INVESTIGATION OF TRANSITION METAL SYSTEMS USING NEW METHODS OF RAMAN SPECTROSCOPY

Dissertation
zur Erlangung des Doktorgrades
des Department Physik
der Universität Hamburg

vorgelegt von
Arne Goos
aus Hamburg

Hamburg
2015

Gutachter der Dissertation:	Prof. Dr. Michael A. Rübhausen Prof. Dr. Robert Blick
Gutachter der Disputation:	Prof. Dr. Michael A. Rübhausen Prof. Dr. Nils Huse
Datum der Disputation:	12.02.2016
Vorsitzender des Prüfungsausschusses:	Prof. Dr. Michael Thorwart
Vorsitzender des Promotionsausschusses:	Prof. Dr. Jan Louis
Dekan der Fakultät für Mathematik, Informatik und Naturwissenschaften:	Prof. Dr. Heinrich Graener

Abstract

In this thesis the results of Raman spectroscopy at transition metal material systems are presented. In particular bio inorganic copper complex model systems were investigated by steady state UV and visible Raman spectroscopy. A systematic study was performed investigating isotope shift in bis(μ-oxo)-dicopper(III) verifying a peroxo-form and granting new insight into the catalytic behaviour. Furthermore, metal to ligand (MTL) and ligand to metal (LTM) charge transfer was studied in guanidine-quinoline copper complexes. A resonance study identifies resonances at 3.4 eV for Cu^I MTL charge transfer and Cu^{II} LTM charge transfer. High temperature superconductor $Bi_2Ca_2CuO_2$ was studied with the novel technique of time resolved pump probe Raman spectroscopy. The study focuses on the superconducting order parameter Δ and its temporal evolution. Two separate components of Δ at different timescales are identified and a model is presented relating these two components to hole-phonon interactions and spin-hole coupling. Time resolved Raman spectroscopy was also used to study the melting and reformation of charge ordered domains in doped $La_{1-x}Ca_xMnO_3$ via observing the decrease in intensity of Jahn-Teller modes. A possible ansatz is discussed to explain the observed antiphasic oscillation of electronic background and Jahn-Teller width and intensity.

Also in this thesis the first results of VUV-Raman spectroscopy at two-leg spin-ladders are presented. A resonance study at the Cu M-edge is presented and screening effects in doped compounds of the correlation energies are found and discussed. Also the technical aspects of the novel VUV-Raman spectrometer at the Free Electron Laser Hamburg (FLASH) are discussed and in detail an alignment procedure of its monochromators is given.

Inhaltsangabe

In dieser Arbeit werden die Ergebnisse der Untersuchungen mit Raman-Spektroskopie an Übergangsmetallsystemen präsentiert. Bioanorganische Kupfer-Komplex-Modellsysteme wurden mit stationärer UV- und sichtbarer Raman-Spektroskopie untersucht. Eine systematische Studie wurde durchgeführt, welche eine Isotopenverschiebung in bis(μ-oxo)-di Kupfer(III) fand. Somit eine peroxo-Form nachweisen konnte, welches neue Erkenntnisse über dessen Rolle in katalytisches Prozesen liefert. Weiterführend wurden Ladungstransfers von Metall zu Ligand (MZT) und Ligand zu Metall (LZM) in Guanidin-Chinolin-Kupfer-Komplexen untersucht. Eine Resonanzstudie identifizierte Resonanzen bei 3.4 eV für den Cu^I MZL Ladungstransfer und den Cu^{II} LZM Ladungstransfer.

Des weiteren wurde der Hochtemperatursupraleiter $Bi_2Ca_2CuO_2$ mit der neuen Messmethode der zeitaufgelösten “pump-probe”-Raman-Spektroskopie untersucht. Die Studie untersucht im Besonderen die zeitaufgelöste Entwicklung des Supraleitungsordnungsparameter Δ. Zwei Komponenten von Δ wurden gefunden, welche sich auf unterschiedlichen Zeitskalen verändern und ein Modell wird eingeführt, welches diese beiden Komponenten mit Loch-Phonon Interaktionen und Loch-Spin Interaktionen erklärt.

Außerdem wurde zeitaufgelöste Raman-Spektroskopie auch verwendet um das Schmelzen und die Reformation des Ladungsgeordneten Zustandes in $La_{1-x}Ca_xMnO_3$ zu untersuchen. Dabei wurde die zeitabhängige Verringerung der Intensität von Jahn-Teller Modi betrachtet. Ein möglicher Mechanismus wird diskutiert um die beobachteten antiphasischen Oszillationen vom elektronischen Hintergrund zur Breite und Höhe der Jahn-Teller Modi zu erklären.

Ebenfalls werden in dieser Arbeit die ersten Ergebnisse von VUV”= Raman-Spektroskopie an zwei-beinigen Spin Leitersystemen präsentiert. Eine Resonanzstudie an der Kupfer M-Kante wird beschrieben und Abschwächungseffekte der Korrelationsenergien in dotierten Proben wurden gefunden und nachfolgend diskutiert. Außerdem werden die technischen Aspekte des neuen VUV-Raman-Spektrometers am Freien Elektronenlaser Hamburg (FLASH) vorgestellt und es wird eine detaillierte Justieranleitung der Monochromatoren gegeben.

Contents

List of Figures

List of Tables

1. Introduction

Raman spectroscopy is a versatile tool for the research of solids and molecules in fluids. Over the past century since the discovery of the Raman effect, Raman spectroscopy is used in many scientific fields such as biology, chemistry, physics and life sciences. With the rise of new light sources, namely the laser, pulsed laser systems, free electron lasers and synchrotrons new Raman applications find its way into modern science while classical UV/VIS[1] still as useful as always for scientific research. In particular, resonance studies with steady state Raman can shad light on the intrinsic modes within a material which can be related to different electronic, phononic, magentic or even superconducting states. Also temperature dependent studies can clarify phase transitions in a medium.

For time resolved Raman spectroscopy a highly stable pulsed laser source is a necessity. Mode locked or q-switched laser provide such light sources over a wide range of laser power, repition rates, pulse width and wavelength. By using two pulsed laser the novel technique of two colour time resolved pump probe Raman spectroscopy arises. With this Raman application it is possible to study the dynamic properties of any given materialclasses, eg. the temporal evolution of phase transitions like the formation of the superconducting phase. VUV-Raman spectroscopy or resonant inelastic soft x-ray scattering (RIXS) is the newest application in science of the Raman effect. With the energies modern free electron lasers provide it is possible to probe element specific eg. directly study the intrinsic behaviour at copper m-edges. Also while UV/VIS Raman scattering is only probing samples at the Γ point due to very small momentum transfers, in the VUV-range a larger portion of the Brillouin zone can be observed.

In this thesis one of the focuses is the study of bioinorganic copper complexes by resonance Raman spectroscopy. These complexes are in the focus of interest because they can mimic the catalytic behaviour of proteins. This is particular interesting for industrial applications like the catalysis of phenoles to quinoles. Furthermore, combined with other techniques like X-ray absorption spectroscopy (XAS) also the entatic nature (see chapter 3) can be investigated.

Furthermore, the superconducting order parameter Δ is investigated in the high temperature superconductor $Bi_2Ca_2CuO_2$. The focus of interest is the up to this date

---

[1] UV/VIS stands for Ultraviolet- and visible Light

still not completely clear nature of the mechanism of behind the superconducting state in high T_Cs. With time resolved Raman the formation of the superconducting state could be observed and two different contributions to Δ could be identified (see chapter 5). Furthermore, also multiferroic materials like doped manganites exhibit strong correlations between charge and magnetic orders which interplay is also in the focus of todays science. Time resolved Raman provides a tool to study the melting and formation of the charge ordered stated striped phase in 50 % doped $La_{1-x}Ca_xMnO_3$. By heating with the pump beam the sample above the transition temperature the decay into the striped ordering can be observed on its timescale and interplay and couplings between charge and lattice degrees of freedom can be found. With VUV-Raman the strongly correlated spinladder compounds $Sr_{14-x}Ca_xCu_{24}O_{41}$ (SCCO) and $La_6Ca_8Cu_24O_{41}$ (LCCO) at the copper M-edge have been studied. These systems inherit a quasi two dimensional substructure and hence can be understood in a two dimensional Hubbard model. While SCCO is intrinsically doped LCCO is undoped with the same structure. In particular, VUV-Raman provides insight into screening effect of the Coulomb one sight repulsion energies U depending on the sample and the orientation of the sample. It also allows to directly observe the hopping energies t and in a Fleury and Loudon model the superexchange energy J.

While steady state Raman is a well known technique, which has been applied for decades, Time resolved Raman and VUV-Raman are very new and unique experimental setups. This thesis provides in detail a description of these setups and also discusses technical details, as well as a newly developed alignment procedure of the VUV-Raman instrument.

2. Theory

In this chapter the fundamental principles of the used experimental techniques are presented and discussed. An overview of the Raman-effect and also an introduction into time-resolved and VUV Raman is given.

2.1. The Raman effect

The Raman effect is an inelastic light scattering process, where an incident photon looses or gains energy after interacting with a medium. It was discovered and first published by Chandrasekhara Venkata Raman and Kariamanickam Srinivasa Krishnan in 1928 [1] by the investigation of molecules with sunlight. Independently from Raman and Krishnan the Raman effect was observed in solids by Grigory Landsberg and Leonid Mandelstam in 1928 [2]. In 1923 the Raman effect has been predicted theoretically by Adolf Smekal [3].
C.V. Raman received the Nobel price for his work with inelastic scattered light in 1930. Over the years many applications of the Raman effect arose and with advances in technology, especial the invention of the laser in the 1960s and the construction of specific Raman spectrometers, which yield a significant increase in resolution and efficiency. Today the Raman effect is used not only to characterise materials in solid state physics, but also to investigate biological compounds such as RNA or complex protein molecules [4].

The inelastic light scattering process can be divided in two different kinds of scattering. The so called Stokes scattering, where the scattered photon looses energy compared to the incident photon energy, and the Anti-Stokes scattering, where the scattered photon gains energy. For Anti-Stokes scattering the material needs to be in an excited state and thus Anti-Stokes scattering is strongly suppressed compared to Stokes scattering at room temperature and almost vanishes at low temperatures. Due to the fact that the wave number $k \sim \omega$ is very small for visible and UV light, compared to common Brillouin zones it can be assumed that all Raman scattering occurs at the Γ-Point ($k = 0$). However, this assumption is not completely valid

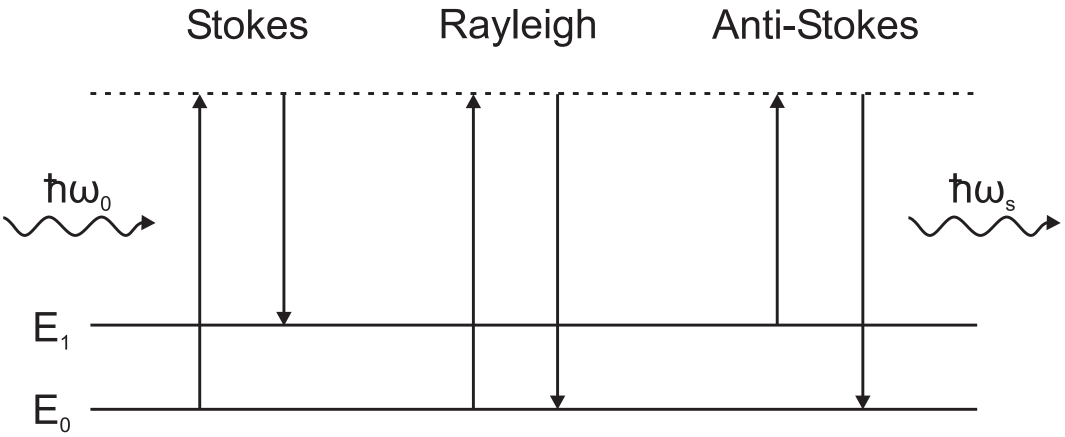

Figure 2.1.: Rayleigh, Stokes and Anti-Stokes process

anymore for higher energy ranges like the VUV. This topic is further discussed in section 2.3.

Inelastic light scattering always comes with elastic light scattering. The elastic scattered light, the so called Rayleigh scattering, has no energy change and is usually the dominant process. The ratio of elastic to inealstic scattered light is in the order of 10^6 when infrared, visible or ultraviolet light is used as incident photon energy. Due to the fact that the intensity of the Raman effect in dipole approximation is proportional to the fourth order of magnitude of the frequency of the incident photon (see section 2.1.1), this ratio becomes much smaller for higher excitation energies in the VUV range. Figure 2.1 shows schematically the three discussed processes related to the Raman effect.

2.1.1. The Raman effect in quantum theory

The classical explanation of the Raman effect considers an electromagnetic wave coupling to an electric dipole in the material. This process is well understood by a classical approach [5, 6], but not sufficient to provide a complete picture about all the other excitations that can occur, for example magnetic or indirect excitations. To describe these phenomena it is necessary to evaluate the underlying Hamiltonian of these excitations and apply perturbation theory. Using Coulomb gauge the Hamiltonian is given by

$$H = \frac{1}{2m}\left(\mathbf{p} - \frac{e}{c}\mathbf{A}\right)^2 \tag{2.1}$$

$$H = \frac{\mathbf{p}^2}{2m} - \frac{e}{mc}\mathbf{A}\cdot\mathbf{p} + \frac{e^2}{2mc^2}\mathbf{A}^2. \tag{2.2}$$

with the momentum $\mathbf{p}$ and the vector potential $\mathbf{A}$,

$$\mathbf{A}(\mathbf{r},t) = \sum_{\mathbf{r},\lambda} \sqrt{\frac{2\pi\hbar c}{kV}} \left(a_{\mathbf{k},\lambda} e_{\mathbf{k},\lambda} e^{i(\mathbf{k}\ \mathbf{r} - \omega_k t)} + a^{\dagger}_{\mathbf{k},\lambda} e^{*}_{\mathbf{k},\lambda} e^{-i(\mathbf{k}\ \mathbf{r} - \omega_k t)} \right), \tag{2.3}$$

where $a^{\dagger}_{\mathbf{k},\lambda}$ ($a_{\mathbf{k},\lambda}$) creates (destroys) a photon with the wave vector $\mathbf{k}$. λ represents the polarisation, $e_{\mathbf{k},\lambda}$ are polarisation operators and V is a volume that denotes periodic conditions and therefore sets specific values for $\mathbf{k}$ and $\omega_k = kc$ [7]. The first term of equation 2.2 can easily be identified as H_0, the second and third term contribute to the electron photon interaction. The second term is linear in $\mathbf{A}$ and therefore is a single photon interaction which does not contribute to the Raman process in first order, and the third term is quadratic in $\mathbf{A}$ denoting a two photon process. The matrix element $M_{\mathbf{A}^2}$ can be calculated by using the charge density operator ρ in k space and using Fermis golden rule the differential cross section becomes normalised to the photon flux [7]:

$$\frac{d\sigma}{d\Omega_{\mathbf{k}'}} = r_0^2 \frac{\omega_s}{\omega_i} |e_{\mathbf{k},\lambda} e^{*}_{\mathbf{k},\lambda}|^2 |\langle n| \rho_{\mathbf{k}\text{-}\mathbf{k}'} |0\rangle|^2 \tag{2.4}$$

where ω_i and ω_s is the frequency of the incident and scattered photon, r_0 is the classic electron radius and $e_{\mathbf{k},\lambda}$ is the polarisation operator. Note, that transitions, that do not change the polarisation of the light, are highly favored . If the binding energy of the electron is very small compared to the incident photon energy, this leads to the so called Thomson scattering [5]. For Raman scattering the incident photon energy is much smaller than typical binding energies, resulting in a contribution of this term to the Raman response.

The second order matrix element resulting from the $\mathbf{p} \cdot \mathbf{A}$ term of equation 2.2 is linear in the vector potential and also a differential cross section can be obtained [7]. For a transition from the ground state $|0\rangle$ via an intermediate state $|m\rangle$ to a final state $|f\rangle$ it becomes: $\hat{R}$ is a position operator and the term $i\eta$ in the denominator is related to the adiabatic nature of the perturbation.

$$\frac{d\sigma}{d\Omega_{\mathbf{k}'}} = \frac{e^3 \omega_i \omega_s^3}{c^4} \left| \sum_m \left(\frac{\langle n| \hat{R} \cdot e^{*}_{\mathbf{k}\ ',\lambda'} |m\rangle \langle m| \hat{R} \cdot e_{\mathbf{k},\lambda} |0\rangle}{\epsilon_0 + \hbar\omega_i - \epsilon_m + i\eta} + \frac{\langle n| \hat{R} \cdot e_{\mathbf{k},\lambda} |m\rangle \langle m| \hat{R} \cdot e^{*}_{\mathbf{k}',\lambda'} |0\rangle}{\epsilon_0 - \hbar\omega_s - \epsilon_m + i\eta} \right) \right|^2 . \tag{2.5}$$

The denominator of equation 2.5 leads to resonance effects, when $\hbar\omega_s \approx \epsilon_n - \epsilon_m$. This kind of scattering is called **Raman scattering**. Depending on the energy difference of incident and scattered photons this leads to Stokes ($\hbar\omega_i - \hbar\omega_s > 0$), Anti-Stokes ($\hbar\omega_i - \hbar\omega_s < 0$), or Rayleigh scattering($\hbar\omega_i - \hbar\omega_s = 0$) as shown in figure 2.1. It is

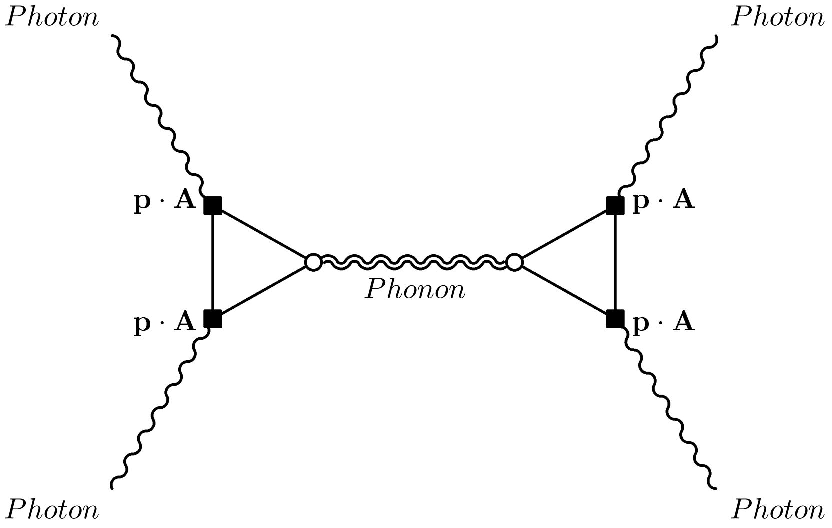

Figure 2.2.: Full Feynman diagram of the Raman scattering process. Due to the $\mathbf{p} \cdot \mathbf{A}$ terms resonances can occur.

obvious, that the intensity of the Raman scattering cross section times the scattering volume is proportional to the fourth power of the frequency of the photons, which are used in a Raman experiment. Therefore it is useful to choose UV or even VUV light to increase signal intensity or shorten integration times.

2.1.2. Many-body response theory

To further investigate the influence of correlation effects in a medium with respect to Raman scattering one has to apply modern response theory formalism. This complex field of modern many-body quantum physics will be briefly explained in this chapter. For further reading please see [8, 9, 10, 11].

In many-body theory excitations are described by different propagators, such as the (free) electron propagator or the phonon propagator. Propagators describe the probability amplitude for a particle to move from one place to another in a given time or to travel with a certain energy and momentum. In non relativistic quantum mechanics propagators are Green's functions [8]. An example for a classical propagator and an introduction into Green's functions is given in appendix A. Figure 2.2 shows the entire Raman scattering process in a Feynman diagram.

The differential scattering cross section for Raman spectroscopy is given by [10, 11]

$$\frac{d^2\sigma}{d\omega_s d\Omega_k} = -\frac{2\pi}{\hbar}\alpha(\hbar\omega_i)2(n(\omega_i)+1)\Im[R(\omega)]. \tag{2.6}$$

where $n(\omega_i)$ is the occupation function, which includes the Bose-Einstein statistical factor representing the bosonic nature of photons, $\hbar\omega_i)$ is denoting the scattering geometry and $R(\omega)$ is the response function of the system [11]. Finding the response function for Raman scattering is strongly dependent on the examined system. In general for Raman the response function can be expressed as

$$R(\omega) = -i \sum_{\mathbf{k},\mathbf{k'},\omega'} \gamma_{\mathbf{k}} G(\mathbf{k'}, \omega') G(\mathbf{k}, \omega + \omega') \Gamma(\mathbf{k}, \mathbf{k'}, \omega, \omega') \tag{2.7}$$

where $G(\mathbf{k'}, \omega')$ a Green's function representing the full single particle propagator, i.e. the propagator plus all interactions with itself γ is vertex, which can be rewritten as a tensor in terms of an effective mass m^* and Γ_k is a vertex correction i.e. the bare vertex with all possible interactions [8, 10, 9].

2.1.3. Electronic Raman scattering

Electronic Raman scattering can be understood as the creation of an electron-hole polarisation bubble. Hereby an electron is excited to an intermediate state, leaving a hole in the band of its origin. In case of resonant Raman scattering the intermediate state corresponds to a real state in an unoccupied band. Starting from equation 2.7 one at first has to calculate the bare electron/hole propagator $G_0(\mathbf{k}, \omega)$ which is given by [10, 8]

$$G_0(\mathbf{k}, \omega) = \frac{1}{\omega - \epsilon_{\mathbf{k}} \pm i\delta_{\mathbf{k}}}. \tag{2.8}$$

The sign in the denominator is dependent on the position of the particle in the k-space. $'+'$ for $k > k_{fermi}$ denotes an electron and $'-'$ for $k < k_{fermi}$ denotes a missing particle, i.e. a hole. With no interactions present in the system, the vertex correction simplifies to $\Gamma = \gamma_{\mathbf{k'}} \delta_{\mathbf{k},\mathbf{k'}}$, which leads to the response of the bare polarisation bubble [9]:

$$R(\omega) = -i \sum_{\mathbf{k},\mathbf{k'},\omega'} \gamma_{\mathbf{k}} G_0(\mathbf{k'} + \tfrac{\mathbf{q}}{2}, \omega') G_0(\mathbf{k} - \tfrac{\mathbf{q}}{2}, \omega + \omega') \gamma_{\mathbf{k'}} \delta_{\mathbf{k},\mathbf{k'}}. \tag{2.9}$$

This non interacting case leads to the simplest electronic response in Raman scattering:

$$R(\omega) = -i \sum_{\mathbf{k},\omega'} \gamma_{\mathbf{k}}^2 \frac{1}{\omega' - \epsilon_{\mathbf{k}-\frac{\mathbf{q}}{2}} + i\delta} \frac{1}{\omega + \omega' - \epsilon_{\mathbf{k}+\frac{\mathbf{q}}{2}} - i\delta}. \tag{2.10}$$

If a weak interacting electron gas is considered, self energy contributions i.e. interaction of the electrons with each other contributions have to be evaluated and calculated into the electron/hole propagator $G(\mathbf{k}, \omega)$ which leads to a Raman Intensity of

$$I(\omega) \propto \Im \left[\frac{2\omega_p}{\omega^2 - \omega_p^2 + 2i\frac{\omega_p}{\tau}} \right], \tag{2.11}$$

where ω_p is the frequency of a free plasmon and τ is its lifetime. A detailed calculation of equations 2.11 and further theoretical background can be found in reference [10]. In the superconducting state the bare propagator cannot be applied anymore because of strong electron-hole interactions forming an electron hole-pair. The propagator takes the form of [8]:

$$G = \frac{u^2}{\omega - \sqrt{\epsilon^2 + \Delta^2} + i\delta} + \frac{v^2}{\omega - \sqrt{\epsilon^2 + \Delta^2} - i\delta}. \tag{2.12}$$

Here Δ is the superconducting order parameter, u and v are solutions of the BCS theory [8, 12]. It is clear that the electronic response is strongly dependent on the nature of the superconducting order parameter, which makes Raman spectroscopy an ideal tool to study superconductors [13, 14].

2.1.4. Phononic Raman scattering

Raman scattering at phonons can be treated as a two part process. First the light creates an electron-hole polarisation bubble which then interacts with the lattice. Figure 2.2 shows this process in terms of a Feynman diagram. In terms of the interaction Hamiltonian H_{int} one has to consider additional contributions of the bare phonons themselves and from the electron-phonon interactions in addition to the electronic response:

$$H = H_{electron} + H_{phonon} + H^{int}_{electron-phonon}. \tag{2.13}$$

The additional components in equation 2.13 lead to additional terms in the self energy of the particle-hole propagator and also to an extended vertex correction Γ. The bare phonon propagator is given by [8]

$$D^0(\mathbf{Q}, \omega) = \frac{\Omega_\mathbf{Q}}{\omega^2 - \Omega_\mathbf{Q}^2 + i\delta\Omega_\mathbf{Q}}. \tag{2.14}$$

Applying the diagrammatic methods described in section 2.1.2 it can be evaluated, that the response function can be written as

$$R(\omega) = R_{electron}(\omega) + R_{electron-phonon}(\omega). \tag{2.15}$$

This shows that always the full electronic response is part of the phononic scattering process. The simplest case is a discrete excitation of a phonon without interaction with an electronic background. In this case it can be shown that $R_{electron-phonon}(\omega)$ is directly proportional to the bare phonon propagator [8, 10]:

$$R_{electron-phonon}(\omega) \sim 4\pi^2 T_p^2 \frac{\Omega}{\omega^2 - \Omega^2 + i\delta\Omega}. \tag{2.16}$$

Here, T_p is the phononic Raman matrix element, which is dependent on the electron phonon coupling constant $g_{\mathbf{k},\mathbf{q}}$ as well as the bare electronic vertex $\gamma_{\mathbf{k}}$. Equation 2.16 leads to a Lorentzian lineshape of the phonon centered at the frequency Ω with the width Γ in the Raman spectrum [6]:

$$I(\omega) \propto I_0 \frac{\omega\Gamma}{(\omega^2 - \Omega^2)^2 + \omega^2\Gamma^2}. \tag{2.17}$$

In case of coupling of the phonon with a continuum of electronic states, e.g. within one band, the phononic response yields a typical Fano lineshape [15].

$$I(\omega) \propto I_0 \frac{(q + (\frac{\omega-\Omega}{\Gamma}))^2}{1 + (\frac{\omega-\Omega}{\Gamma})^2}. \tag{2.18}$$

Here, q is the “Fano parameter”, which is responsible for the asymmetry of the resulting lineshape. It contains information of the electronic and phononic Raman matrix elements T_e and T_p as well as the electron-phonon coupling constant $g_{\mathbf{k},\mathbf{q}}$ and the imaginary part of the electron-hole polarisation bubble ρ:

$$q \approx \frac{T_p}{T_e} \frac{1}{g_{\mathbf{k},\mathbf{q}}\rho}. \tag{2.19}$$

When the electron-phonon coupling constant is very small, i.e. $g_{\mathbf{k},\mathbf{q}} \to 0$, q gets very large and the Fano-profile exhibits a Lorentzian lineshape. Figure 2.3 shows the Lorentz- and Fano lineshape.

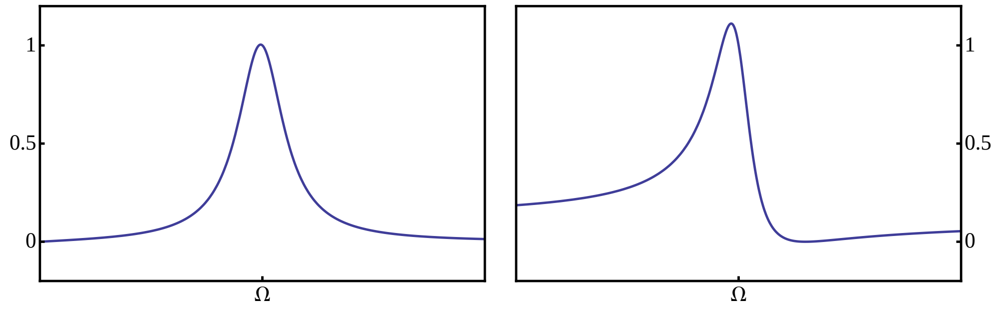

(a) Lorentzian lineshape **(b)** Fano lineshape

Figure 2.3.: (a) Lorentzian lineshape. (b) Fano lineshape. Both lineshapes are normalised to 1, in the Fano Profile q was set to -3. Spectra were calculated using equations 2.17 (a) and 2.18 (b).

2.1.5. Magnetic Raman scattering

To understand magnetic excitations in ferromagnetic and anti-ferromagnetic compounds, the interaction Hamiltonian responsible for magnetic scattering has to be found. A first approach considers only nearest neighbour spin interactions in a half filled Hubbard model. The resulting Hamiltonian is [16]

$$H_0 = J \sum_{\mathbf{i},\mathbf{j}} \mathbf{S_i S_j}, \tag{2.20}$$

where J is the superexchange constant (see also section 3.2.3) and $\mathbf{S_i S_j}$ denotes nearest neighbour spin states. The effective interaction Hamiltonian from this approach has been calculated by Fleury and Loudon in 1968 for magnetic Raman scattering [16]:

$$H_{int} = J \sum_{\mathbf{i},\mathbf{j}} P(\omega_i, \omega_s, \delta) \mathbf{S_i S_j}. \tag{2.21}$$

Here, $P(\omega_i, \omega_s, \delta)$ denotes the applied scattering geometry.
A simple picture to understand magnetic Raman scattering is to envision the number of broken bonds that a spin flip excitation would produce in a two dimensional lattice. Every broken bond contributes $J/2$, so that a simple spin flip would be seen at $6 \cdot J/2 = 3J$ in the Raman spectrum because 6 bonds have to be broken for the full process to complete.

2.2. Time-resolved spontaneous Raman spectroscopy

In many condensed matter systems certain effects like the formation of domains or the transition to normal into the superconducting state are on a short timescale which can not be observed by “normal” Raman spectroscopy. Time resolved Raman spectroscopy is a tool to observe effects that occur on short timescales i. e. in the pico- and femtosecond range. The basic principal is to excite a sample out of its equilibrium state by a “pump” energy, and then observe the non-equilibrium state by a delayed probe beam. It is important to note that with this technique Fermis golden rule can no longer be applied to calculate the response function in a straight forward fashion. However, the Raman response can still be considered being spontaneous. Therefore time-resolved Raman spectroscopy can be used to study the interesting physics of first and second order phase transitions in solids.[17]
To introduce a phase transition different pumping methods can be applied. The simplest case is to use a pulsed laser beam to heat up the sample above a transition temperature and then observe the decay, i.e. the time dependent phase transition

into the ground sate. For the superconducting state a modified heating theory exists that relates the superconducting gap Δ to the new quasi equilibrium temperature T^* or the chemical potential μ^* [18, 19, 20]. This leads to a temperature dependent response of a given operator

$$< a^\dagger_{\mathbf{k}} a_{\mathbf{k}} >= \left(e^{\frac{\epsilon_{\mathbf{k}}(T^*)}{k_B T^*}} - 1 \right)^{-1} . \tag{2.22}$$

Another approach is to only consider the parts of the Hamiltonian related to the phase transition and then directly solve the Heisenberg equation of motion:

$$\frac{d}{dt}\mathcal{O} = \frac{\hbar}{i}[H, \mathcal{O}] + \frac{\partial \mathcal{O}}{\partial t}. \tag{2.23}$$

Here $\mathcal{O}$ is an arbitrary operator and H is the Hamiltonian describing the system. This method has been performed to describe the time resolved thermal melting and recombination of the superconducting state of superconductors [17].

Another possibility to pump, i.e. excite a system is to use a pump energy that is in direct resonance to a transition within the observed medium. If the energy of the pump beam is in resonance to for example a charge transfer process, the electronic structure is directly pumped in an excited non-equilibrium state. This approach can e.g. be used to study the dynamics of domain melting and formation in doped manganites by observing the strength of Jahn-Teller modes.

Figure 2.4 shows schematically a time resolved pump probe experiment. The advantage of time resolved Raman spectroscopy is that phase transitions can be observed with a high sensitivity to the symmetries of the underlying order parameters. Therefore it is an excellent tool to learn more about electron-phonon coupling, the temporal evolution of superconducting gaps or even magnetic excitations.

2.3. VUV-Raman Spectroscopy

With the rise of new light sources in the VUV range (vacuum ultraviolet $\sim 10 - 200\ nm$) and the high brilliance of modern free electron lasers working in the VUV range such as the Free Electron Laser Hamburg for the first time Raman experiments in this range became possible.

There are a lot of advantages by using this energy range. As shown in section 2.1.1 the intensity of the Raman scattered light is proportional to the fourth of its frequency, Raman scattering is a much more intense process in the VUV range than in the visible. This allows to either shorten data acquisition i.e. integration times or even to observe small excitations, which could not be resolved in the UV or visible range.

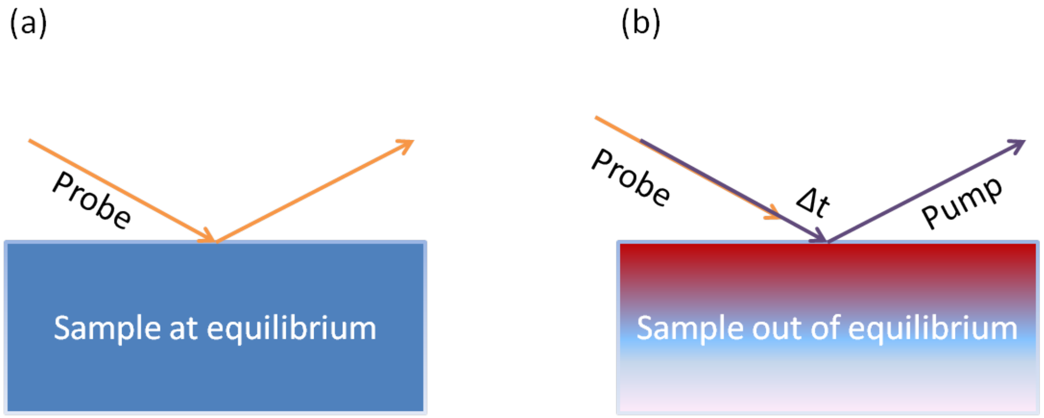

Figure 2.4.: (a) Steady state Raman scattering. The probe beam hits the sample which is in equilibrium. The Raman scattered light (Rayleight, Stokes and anti Stokes) is instantaneous in time. (b) Pump-probe experiment. The pump beam hits the sample and brings it out of the equilibrium state. With a temporal delay the probe beam hits the sample.

Another advantage of VUV-Raman spectroscopy is, that more of the Brillouin zone can be observed. While even in backscattering the momentum transfer of the incident light is small compared to typical sizes of the Brillouin zone in the UV and visible range, so that all Raman scattering occurs at the Γ-Point, with higher incident photon energy more of the Brillouin zone can be observed around the Γ-Point. Assuming a typical lattice constant a of 5 Å and an incident photon energy of 120 eV (copper M_1-edge) and backscattering geometry the ratio between the size of the Brillouin zone and the momentum transfer is

$$\frac{\Delta k}{k_{brillouin}} = \frac{2Ea}{hc} \cong 0.1. \tag{2.24}$$

This gives rise to the possibility to detect even acoustic phonons in Raman scattering in materials with usual lattice constants.
Furthermore, the VUV range closes the gap between resonant inelastic light scattering (RIXS), which performs inelastic light scattering at the core shells (K- and L-edge), and the UV/visible range. With VUV inelastic light scattering it is possible to directly go into resonance with the M-edges and therefore specifically probe orbitals with a high resolution. For example the copper 3s and 3p orbitals belong to the VUV energy range, enabling an orbital selective study of the related physics of copper oxygen driven superconductors or transition metal oxides possible. In table 2.1 the l- and m-edges of several elements are displayed. The red numbers are in the VUV range.

Atomic Number	Element	L_1	L_2	L_3	M_1	M_2	M_3
		$2s_{1/2}$	$2p_{1/2}$	$2p_{3/2}$	$3s_{1/2}$	$3p_{1/2}$	$3p_{3/2}$
6	C						
7	N	19					
8	O	24					
9	F	31					
10	Ne	48	22				
11	Na	63	30				
12	Mg	89	49				
13	Al	118	73				
14	Si	149	100	99			
15	P	187	131	130			
16	S	229	165	164	16		
17	Cl	270	200	199	16		
18	Ar	326	251	249	29	16	
19	K	379	297	294	35	20	
20	Ca	438	350	347	44	25	
21	Sc	498	404	400	51	28	
22	Ti	561	461	455	58	33	
23	V	627	521	513	64	37	
24	Cr	698	585	576	75	42	
25	Mn	769	651	639	82	47	
26	Fe	848	721	707	92	53	
27	Co	927	781	769	101	59	
28	Ni	1010	871	854	111	67	
29	Cu	1099	953	933	122	77	75
30	Zn	1196	1045	1022	140	91	89

Table 2.1.: List of the L and M edge energies by element in eV. The red numbers represent energies in the VUV range.

3. Condensed-Matter Physics

In this chapter an overview about the investigated strongly correlated material system, i.e. bio-inorganic molecules, manganites and cuprate high temperature superconductors and their inherent physics is given.

3.1. Molecules with copper centers

Metal sites play an important role in biology [21] e.g. the binding of oxygen in hemoglobin. Estimations yield that almost one third of all proteins and enzymes require metal ions for their functions. Copper in particular fulfills an important role in the nervous system in higher eukaryotes [22]. Furthermore it is a key factor in oxidation-reduction reactions [23]. Protein with bound metal ions can be classified by their function:

- structure: configuration of the protein structure
- storage: uptake, binding and release of metal ions
- electron-transfer: uptake, release and storage of electrons
- dioxygen binding: metal-O_2 coordination
- catalytic: substrate binding, activation and turnover.

One of the best understood copper oxigenases is tyrosinase, an enzyme that is found in all living organisms. An important role of tyrosinase is the catalysis of the oxidation of phenol. This catalytic process is not fully understood and in the focus of research. However, the efficient oxygen transfer that tyrosinase inherits might be of high potential for industrial catalytic oxidation reactions.

The catalytic process of tyrosinase relies on an active center consisting of two Cu^I connected by Oxygen atoms. This active site can switch between two molecules with the same number of electronic valences but different in structure and electronic configuration. Figure 3.1 schematically shows two different states of the active site of tyrosinase. It is unknown if an oxo- or peroxo-core is responsible for the oxygen transfer during catalysis. To understand the oxygen-transfer process and its possible

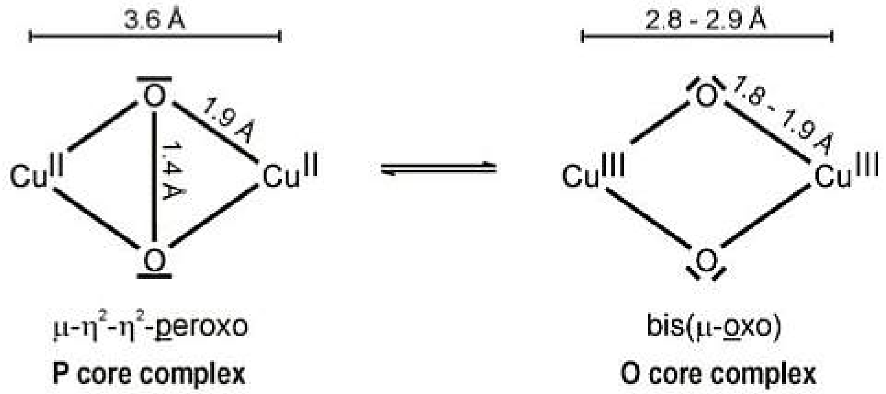

Figure 3.1.: Oxo and peroxo structure of the isomeric states of $\mu - \eta^2 - \eta^2$-peroxo/bis(μ-oxo) dicopper systems [23, 24].

applications in industry, i.e. aromatic oxidation reactions, various model complexes with identical active sites but different ligands have been created. The creation of an oxo- or peroxo-core complex is dictated by nitrogen donors [25]. A possible scheme for the catalysis of phenols is depicted in figure 3.2. Because this process is very complex in its nature, it is important to identify, proof or falsify the intermediate steps in this cycle. The main focus in this thesis is to investigate the reaction show in the upper right part of figure 3.2. In this step two ligand Cu^I complexes are synthesised to a peroxo copper complex. To verify that a peroxo-core forms and not an oxo-core, one can investigate the phononic modes associated with these two configurations (see Chapter 5).

In a more general manner a group of atoms or molecules which is bonded to a protein which can adopt its geometric and or its electronic configuration for function are in an “entatic-state” [27]. This entatic behaviour applies to model complexes with copper centers. Depending on the oxidisation state of the copper, the core energetically prefers square-planar coordination for Cu(II) or tetrahedal for Cu(I). During electron transfer, the copper center changes its oxydation, which also slightly changes the geometry. Therefore, the bonding angle and the length from ligand to copper is different for Cu(I) and Cu(II) states. The exact mechanism behind the functionality of entatic state is not fully understood and therefore in the focus of interest.

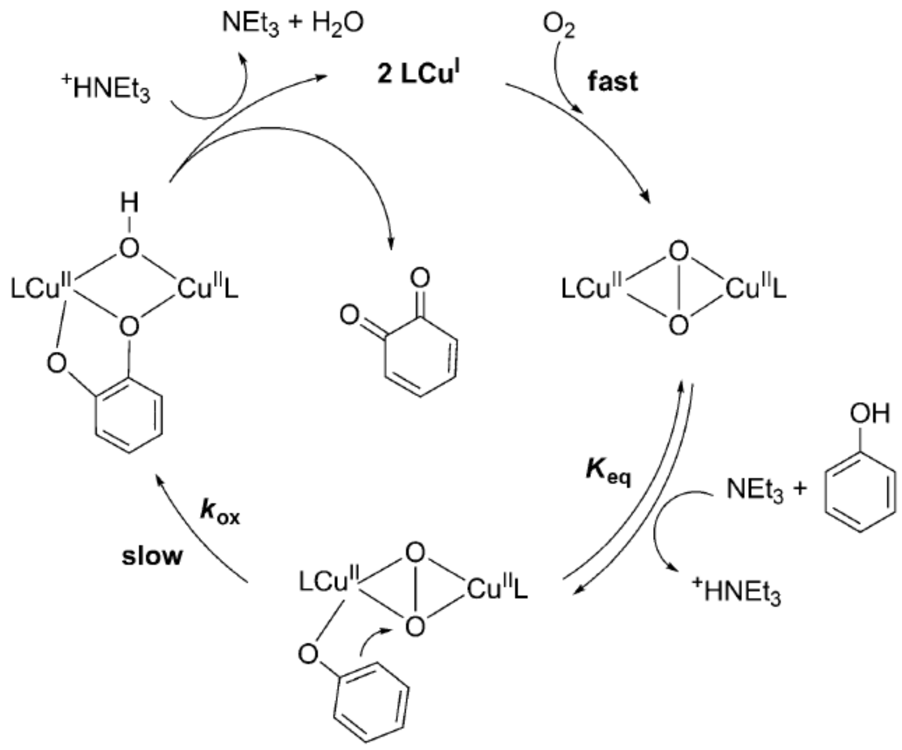

Figure 3.2.: Proposed catalytic mechanism of phenol oxidation [26].

3.2. Manganites

Transition metal oxides such as manganites, belong to a group of materials which is referred to as “strongly-correlated systems”. While many materials can be described with the free electron model [28], where the electrons are treated as simple particles moving through the material and are not interacting with each other, in “strongly correlated systems” electron-electron interaction has to be considered in the Hamiltonian of the system to fully describe the characteristics of this material class. This leads to new physical effects, which can be found in “strongly-correlated systems” with the colossal magnetoresistance [29, 30, 31] as the most prominent example in manganites. This subsection briefly gives an overview of the geometric and electronic structure of manganites and the resulting basic effects and principles.

3.2.1. Structure

Manganites crystallise in the so called pervoskite structure named after the Russian mineralogist L. A. Perovski. The general formula of a pervoskite is ABX_3, where A and B are cations and X is an anion. In case of manganese this formula sim-

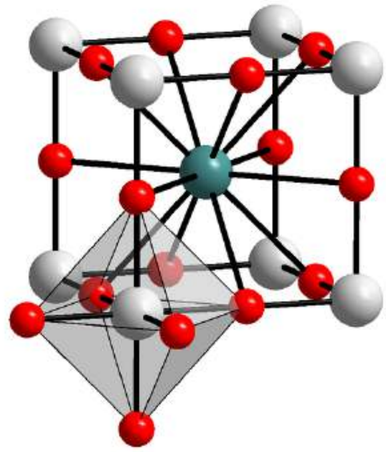

Figure 3.3.: Pervoskite structure. The green and white atoms are cations, the red atoms are anions. In case of manganites the green atom belongs either to the rare earth elements or the alkaline earth metals, white are the manganese ions and red are the oxygen ions creating an oxygen octahedron around an manganese ion.

plifies to $R^{3+}Mn^{3+}O_3^{2-}$ with R being an element of the rare earth group R={La, Nb, Sm,...}. Another possibility to form the pervoskite structure is the elemental formula $A^{2+}Mn^{4+}O_3^{2-}$, with A={Ca, Sr, Ba,...} being a member of the alkaline earth metals. Mixtures of both forms are the so called doped manganites with the structural formula $R_{1-x}A_xMnO_3$. In this structure the manganese occurs in different oxidation states (Mn^{3+}, Mn^{4+}) which leads depending on the value of x to a orthorombic or romboedric distortion of the pervoskite structure. The basic pervoskite structure is displayed in figure 3.3. In the middle of the structure the atom of the rare earth group or of the alkaline earth metal is located. It is surrounded by eight Mn atoms which are placed in corners of a cube around the center atom. The oxygen atoms are located on the edges. Six oxygen atoms and one manganese atom form a MnO_6 oxygen-octahedron with the manganese in the middle. The $Mn^{3+}(Mn^{4+})$ ion has four (three) electrons in 3d valence orbitals. These valence states are degenerated in a free manganese ion but due to the existence of the oxygen octahedron their coulomb potential splits the 3d state in a t_{2g} and a e_g energy level. This effect is known as a crystal field splitting [32]. The t_{2g} energy state consists of the d_{xy}, d_{xz} and d_{yz} orbitals, which are pointing between the oxygen atoms and the e_g state of the $d_{x^2-y^2}$ and $d_{3z^2-r^2}$ orbitals, which are pointing directly towards the oxygen atoms. In the case of Mn^{4+} only the t_{2g} energy levels are occupied and degenerated. However, in the case of Mn^{3+} one electron is present in the e_g state.

By displacing itself with respect to the surrounding, an ion can create an additional non cubic potential which further splits the t_{2g} and e_g states. Such an effect is known as the Jahn-Teller distortion or the Jahn-Teller effect. The Jahn-Teller effect lowers the energy of the $d_{3z^2-r^2}$ orbital and increases the energy of the $d_{x^2-y^2}$ orbital by an energy of δ_{JT}. Also the potential energy of the d_{xy} orbital is increased and the potential energy of the d_{xz} and d_{yz} orbitals is decreased. This splitting is only energetically favored with exactly one electron in the e_g energy level and therefore only occurs to Mn^{3+} ions. Figure 3.4 displays the removal of the degeneracy of the 3d state of manganese by crystal field splitting and the Jahn-Teller effect.

Furthermore, long ranged charge and orbital ordering are present in manganites, i.e., between the manganese ions. In this thesis specifically the properties observed in $La_{1-x}Ca_xMnO_3$ will be reviewed. Figure 3.5 shows the phase diagram of LCMO. LCMO behaves depending on doping and temperature as a paramagnetic insulator, paramagnetic metal, ferromagnetic insulator, ferromagnetic metal or antiferromagnetic insulator. In case of very low (x<0.075) and very high (x>0.85) doping and at low temperatures a canted-antiferromagnetic order has been observed. Also the formation of periodic Mn^{3+} and Mn^{4+} structures is observed and referred to as charge ordering. A charge order state occurs at a commensurate doping. In the x=0.5 case this charge ordering is of extreme long range and results in the occurrence of a strip like pattern with alternating Mn^{3+} and Mn^{4+} fringes [37]. Orbital ordering is referred to as long range periodic ordering of the orientation of the e_g orbitals. These orientations form due to coulomb repulsion of the charge clouds, however, the effect

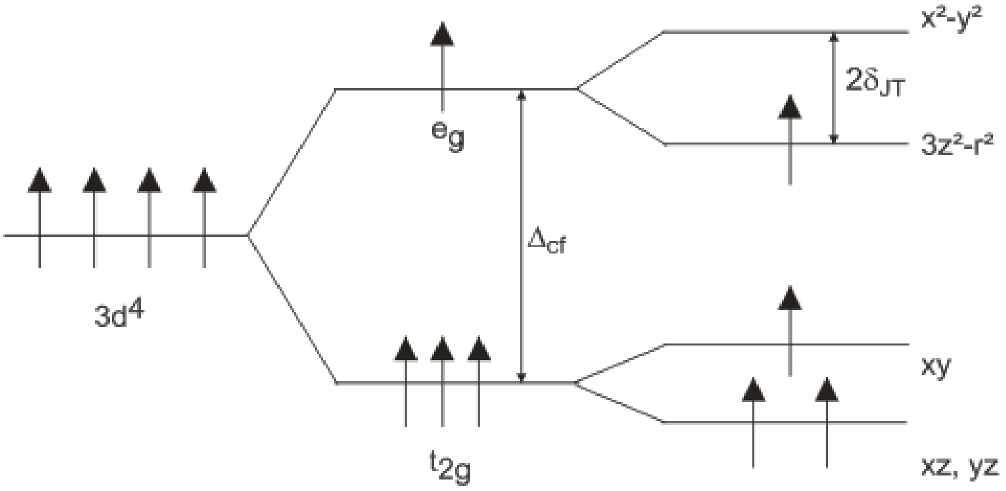

Figure 3.4.: Crystal field splitting and Jahn Teller effect displayed in Mn^{3+} surrounded by an oxygen octahedron [33]. Typical values for Δ_{cf} are 2.5 eV for Mn^{4+} and 1.8 eV for Mn^{3+} [34, 35] and for δ_{JT} the values vary between 0.5 eV and 1.5 eV [35, 36].

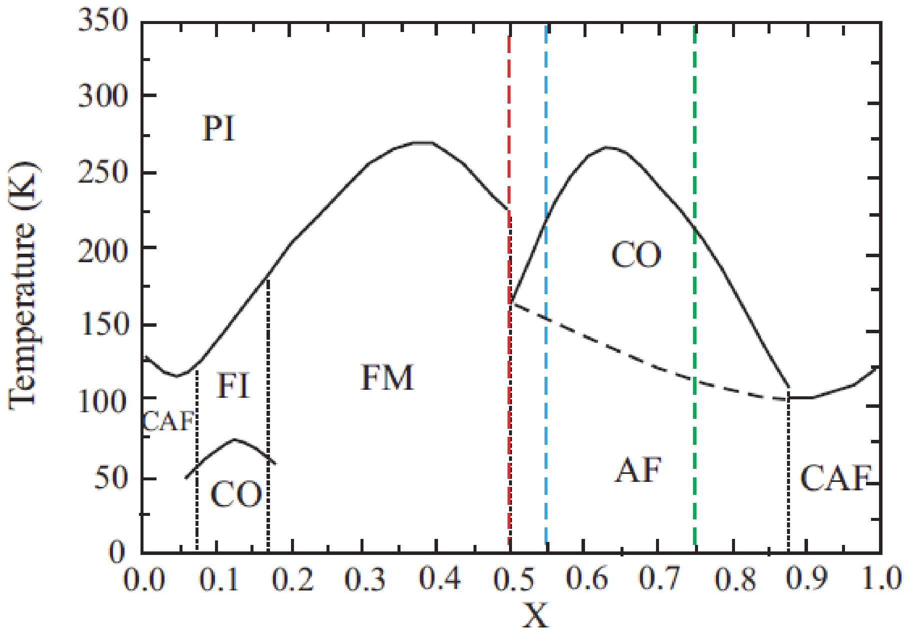

Figure 3.5.: Phase diagram of $La_{1-x}Ca_xMnO_3$. CAF denotes canted antiferromagnetic, PI paramagnetic insulator, FI ferromagnetic insulator, FM ferromagnetic metal, AF antiferromagnetic order and CO charge order. The red, blue and green lines denote the doping further discussed later in this thesis (see chapter 5). [29]

is stabilised by the Jahn-Teller effect [38]. Charge and orbital ordering have a huge connection to the magnetic orderings observed in LCMO and vice versa. Due to the missing overlap between the orbitals nearest neighbour manganese ions, interactions which form charge, orbital or magnetic ordering have to take place via an oxygen ion as a bridge. The two different exchange mechanisms that are supposed to be the driving force behind the magnetic orderings in doped manganites are the double exchange and the super exchange. Basic charge, orbital and magnetic ordering is displayed in figure 3.6.

3.2.2. Double Exchange

The double exchange formalism describes the effective charge and spin transport in mixed valence manganites via an oxygen atom. It requires a ferromagnetic ordering due to Hund's rule coupling and was first described by C. Zener in 1951 [40]. The initial state is a Mn^{3+} ($3d^4$) next to an O^{2-} ($2p^6$) next to a Mn^{4+} ($3d^3$). The spins are ferromagnetically ordered. In an intermediate state one electron from the oxygen moves to the Mn^{4+} thus leaving an $O^{1-}(2p^5)$ behind. This intermediate state can simply decay to the original state leaving the situation unchanged or an electron from the previously unchanged Mn^{3+} can move to the oxygen atom. If

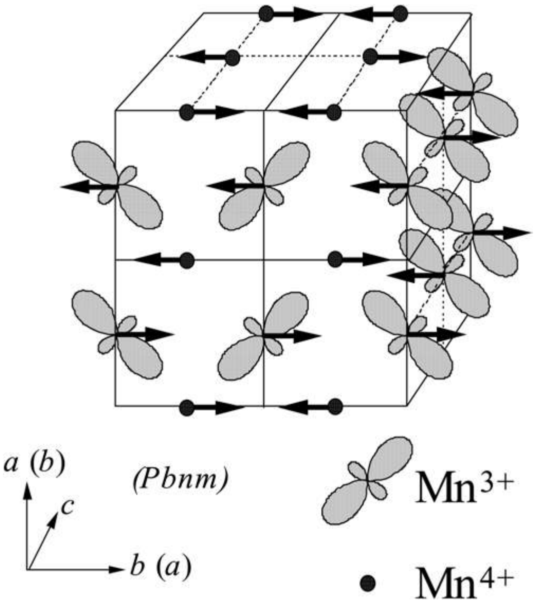

Figure 3.6.: Charge, orbital and magnetic ordering in half doped maganites. Spins are denoted as arrows, the orientations of the occupied e_g orbitals of Mn^{3+} are displayed in gray and Mn^{4+} is displayed as black dots [39].

this is the case an effective charge transfer within the lattice has occurred via an oxygen bridge from one manganese ion to another. The processes are considered to happen simultaneously, and therefore the electrons transported via double exchange are delocalised. This leads to a ferromagnetic metallic behaviour with the double exchange as the driving force. Figure 3.7 schematically shows the double exchange process.

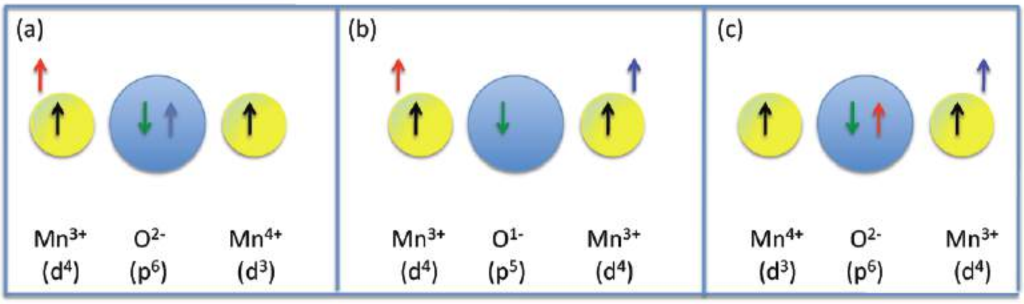

Figure 3.7.: The double exchange process. (a) denotes the initial state, (b) the intermediate state and (c) the final state. [41]

3.2.3. Super Exchange

Contrary to the double exchange described in the previous section the super exchange explains the spin exchange in an antiferromagnetic lattice with no overall redistribution of charge. The principle was first described by H.A. Kramers in 1934 and results from higher order perturbation theory [42]. Starting from a two dimensional quadratic lattice with half filled valence band and therefore with a spin of 1/2, such a system can be evaluated by the Hubbard Model which gives the groundstate energy by the Hamiltonian [43, 44, 45]:

$$H = H_0 + H_1 = -t \sum_{\mathbf{r},\mathbf{r'},\sigma} \left(c^{\dagger}_{\sigma}(\mathbf{r}) c_{\sigma}(\mathbf{r'}) + h.c. \right) + U \sum_{\mathbf{r}} n_{\uparrow}(\mathbf{r}) n_{\downarrow}(\mathbf{r}). \tag{3.1}$$

Here, t represents the energy that is required to move one electron from one place in the lattice to the nearest neighbour, $c^{\dagger}_{\sigma}(\mathbf{r})$ ($c_{\sigma}(\mathbf{r'})$) are creation (anihilation) operators of an electron at the site $\mathbf{r}$ ($\mathbf{r'}$), U is the energy that is required to create an double occupied state and $n_{\uparrow}(\mathbf{r})$ ($n_{\downarrow}(\mathbf{r})$) are the number operators for spin up (spin down). In the strong coupling limit with $U \gg t$ the H_0 can be treated as a small perturbation to H_1 a basic pertubation theory can be applied. This leads to the Heisenberg model of antiferromagnetism [9].

$$H_J = H_0^2 = J \sum_{\mathbf{r},\mathbf{r'}} \mathbf{S}(\mathbf{r}) \mathbf{S}(\mathbf{r'}) \tag{3.2}$$

Here $J = \frac{4t^2}{U}$ is the superexchange energy which is proportional to t squared, i.e. for a spin exchange the energy has to be delivered twice, with 4 being the number of nearest neighbours in a quadratic lattice.

The superexchange process is portrayed in figure 3.8. In the initial state $|a\rangle$ an electron hops to its nearest neighbour forming an intermediate state $|a'\rangle$. Due to the strong Coulomb on-site repulsion the intermediate state decays either to the original state or to a final state $|a''\rangle$. If this is the case two spins have effectively flipped requiring the energy J while no redistribution of charge has occurred. In manganites this means that two next nearest manganese ions of the same valence become antiferromagnetically coupled through the oxygen atom in between.

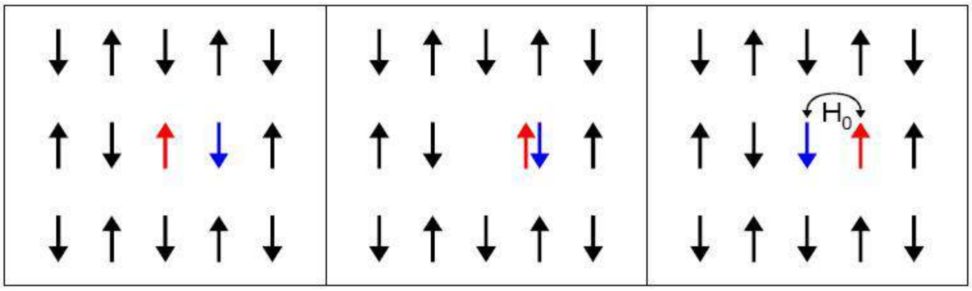

A) |a> B) |a`> C) |a``>

Figure 3.8.: Super exchange process. A) denotes the initial state, B) the intermediate state and C) the final state. [10]

3.3. Cuprates

Another group of strongly correlated materials are the cuprates. With the discovery of high T_c superconductivity by Bednorz and Müller in 1986 [46], cuprates became the focus of interest in solid state physics in the late last century. With the further investigation in subsequent years many new superconducting materials have been discovered. Soon the formation of the superconducting state was related to the copper oxygen planes that are present in most of the high T_Cs but the basic driving mechanisms of high temperature superconductivity are up to date not fully understood. Another interesting feature of cuprates is the formation of Wigner hole crystals in doped high T_Cs. In the following subsection this thesis gives a short introduction of these two phenomena and will focus then on the two different cuprate material systems Bismuth Strontium Calcium Copper Oxide (Biscco-2212) and Strontium Copper Oxide (SCO), the later being a spin ladder compound.

3.3.1. High temperature superconductivity

In 1911 H.K. Onnes discovered the vanishing of the electric resistance of Mercury at the temperature of liquid Helium [47]. This effect could not be explained by the classical theory of electron transport and was called superconductivity. Further studies by Meissner and Ochsenfeld in 1933 showed that superconductors behaved like a perfect diamagnet, which means that an external magnetic field is excluded within the superconductor [48]. It was shown by the brothers London, that the distance an external magnetic field can penetrate a superconductor, the so called London penetration depth λ_l is characteristic for a given superconducting material [28]. However, the superconducting state could be broken by applying a critical field H_c. Later these materials became classified as type I superconductors. Type II superconductors exhibit two different critical magnetic fields H_{c1} and H_{c2} instead. Up to H_{c1} type II superconductors show the same behaviour as type I, above H_{c1} the perfect diamagnetism is not present any more, which means an external magnetic field can penetrate the superconductor and create field tubes within the material, while up to H_{c2} the superconducting state still persists. The phase below H_{c1} is referred to as Meissner-phase, while the phase in between the two critical magnetic fields is know as the Shubnikov-phase [49].

A theoretical explanation for the phenomena of superconductivity at low temperatures is given by the BCS-Theory, named after Barden, Cooper and Schrieffer, in 1957 [12]. The superconductivity was explained by the formation of a new quasi particle the "Cooper pair". Cooper pairs are two electrons with opposite momentum and spin that are coupled through a lattice vibration. They have to be imagened as

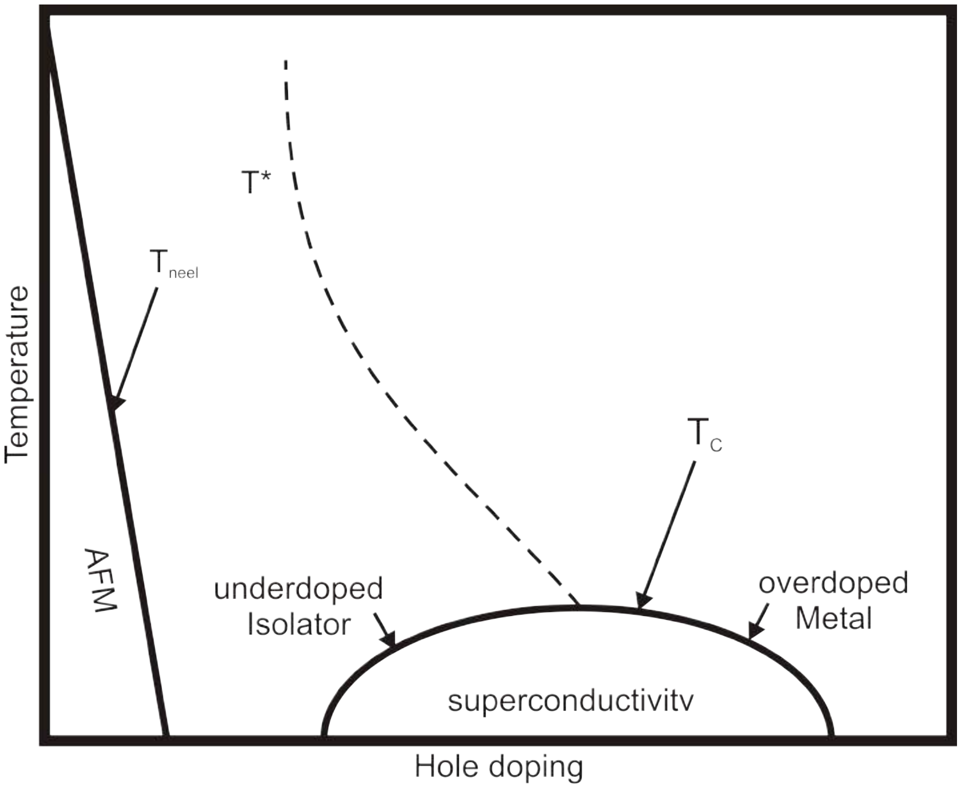

Figure 3.9.: Phase diagram of hole doped cuprate superconductors. T_{neel} is the Néel temperature, T^* is the transition temperature in the pseudogap state and T_c is the critical temperature for forming the superconducting state [33, 10, 50].

an electron polarising the ionic background in the lattice by its electric field, which causes a phonon in the material. Another electron "sees" this phonon (i.e. the moving of the positive ion background) and through coulomb attraction it changes its energy and momentum. Therefore the two electrons become coupled. Cooper pairs are characterised by different attributes. First of all they behave bosonic, which means they can be described with a single wave function, they have a characteristic coherence length ξ, which is basically the size of the Cooper pair and the superconducting order parameter Δ. According to the BCS-Theory, Δ is the energy gap that is created because of the lower energy of the Cooper pair in respect to the Fermi energy. Because of this energy gap with a width of 2Δ, Cooper pairs can not diffract at other electron or ions anymore unless the energy of 2Δ is applied. At room temperature lattice vibrations have a higher energy than the superconducting gap, which leads to the breaking of Cooper pairs, however, at low temperatures the energy of the lattice vibration can not break Cooper pairs anymore and this leads to the superconducting state and therefore to resistance free charge transport [28].

In high temperature superconductors the BCS-Theory is not able to explain the superconducting state and until now no overall theory could be found for this phe-

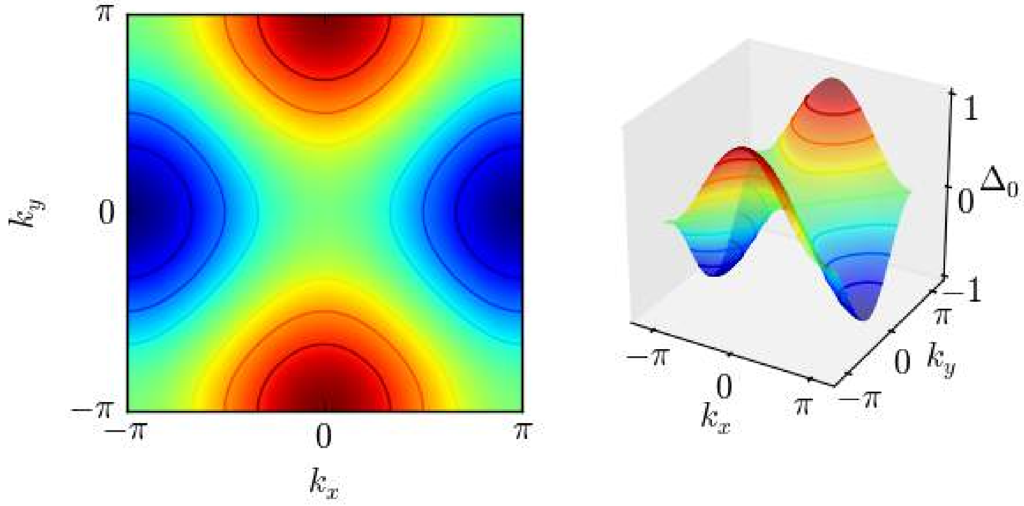

Figure 3.10.: Superconducting order parameter Δ in d-wave symmetry in k-space.

nomenon. An understanding of the different ordering mechanisms is difficult because of the higher chemical complexity of the compounds. It is agreed that all cuprate high T_cs belong to the type II superconductors. Further it is believed that copper oxygen layers (CuO_2) in cuprate high T_c superconductors are the key structures with regards to superconductivity. These quasi two dimensional copper oxygen layers inhibit strong correlation effects with competing mechanisms that are not fully understood and are in the focus of ongoing research. It is believed that instead of electrons, which form Cooper pairs in classical superconductors, in hole doped cuprate high T_cs the holes are responsible for the superconductivity. Investigation of hole doping in cuprate superconductors leads to the phase diagram shown in figure 3.9. At low hole dopings a three dimensional antiferromagnetic (AFM) insulating state forms below the Néel temperature. With increased hole doping the Néel temperature decreases, the cuprate behaves like an underdoped insulator. With increasing doping the superconducting state forms at an optimal doping with the highest T_c of 0.16 holes per copper oxide plane unit cell. With further increase of the hole doping T_c becomes smaller and the system is called an overdoped metal. Another feature of cuprates is the formation of a pseudogap. The pseudogap is an energy gap observed at the Fermi surface occurring below T^* and above T_c. The origin of the pseudogap is still under debate and further reading on this topic can be found in [50].

For a long time the symmetries of the order parameter Δ in high T_c cuprates led to heavy debates in the community [51]. Experiments showed different results regarding this topic [52, 53]. It is agreed that the order parameter Δ is highly anisotope in the z-direction due to the formation of the superconducting state in the CuO_2 layers. Further it was concluded that the two dimensional symmetry of the order

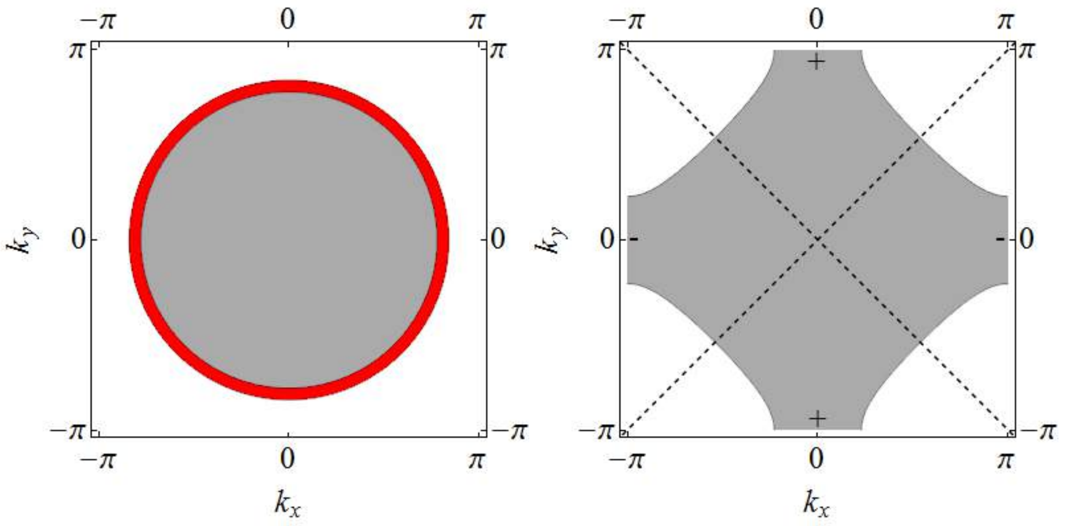

(a) **(b)**

Figure 3.11.: (a) Fermi space in conventional superconductor, the red circle denotes the energy gap 2 Δ. (b) Fermi space of a hole doped cuprate superconductor as measured by ARPES [55]. The signs denote whether the d-wave like superconducting order parameter $\Delta_{d_{x^2-y^2}}$is positive or negative between the dashed lines. The graphics are adapted from [33, 54].

parameter is either s-wave like, which means that it is isotope in the k-space (see figure 3.11 (a)) like in conventional three dimensional superconductors, or that the dominate symmetry is d-wave like, more precisely it exhibits the $d_{x^2-y^2}$ symmetry. Figure 3.10 displays the order parameter $\Delta_{d_{x^2-y^2}} = \frac{\Delta_0}{2}(\cos k_x - \cos k_y)$ in k-space. A d-wave like order parameter changes its sign depending on the position in k-space. This leads to a rise of a new coupling apart from traditional phonon coupling as the driving force of the superconducting state. It also states that phonons within the Fermi surface, that would bridge one of dashed lines in 3.11 (b) would lead not to an attractive coupling interaction and therefore can not be the driving coupling mechanism for the forming of the superconducting state, due to the symmetry of the order parameter $\Delta_{d_{x^2-y^2}}$. Over the last years the mixing of the two proposed order parameters led to a $d_{x^2-y^2} + \alpha s$ order parameter for orthorhombic systems [54]. This ansatz would resolve the confusion of the different measured order parameter symmetries mentioned earlier in this section.

Also still under heavy debate in hole doped high temperature cuprate superconductors is the mechanism that leads to pairing of the holes to Cooper pairs. The discussion leads from B_{1g} phonons, which exhibit the same symmetry as the d-wave order parameter to the pairing through antiferromagnetic spin density wave fluctuations, the so called paramagnon [56, 57], which could lead to the forming of hole

Cooper pairs in d-wave symmetry. Also the role of inhomogenities is discussed regarding the pairing mechanism. However, a concluding experiment that resolves the underlying question of pairing in high T_c cuprate superconductors is still missing.

3.3.2. Wigner crystallisation

A competing mechanism to superconductivity observed in some superconducting materials is the Wigner crystallisation [58]. In 1934 Wigner investigated interactions of electrons in metals [59]. In case of a low density of charge carriers, the kinetic energy is small compared to the potential energy of the lattice. The average distance between electrons (or holes) is long which means a long range repulsive coulomb interaction is occurring. As a result the charge carriers crystallise equidistant in the so called Wigner lattice. In three dimensions this would be a body centered cubic (bcc) lattice, in two dimensions a triangular lattice and in one dimension an equidistant chain. At $T = 0$ only one parameter is needed to characterise the state of the free electron gas, the Wigner-Seitz radius $r_s = a/a_0$, where a is the average inter-particle spacing and a_0 is the Bohr radius. Theoretical calculations regarding the formation of a Wigner lattice in the free electron gas state, that for r_s in the range of 100 to 150 [60] a Wigner lattice in three dimensions forms, while in two dimensions this happens for $r_s > 37.5$ [61].

3.3.3. $Bi_2Sr_2CaCu_2O_{8+\delta}$

$Bi_2Sr_2CaCu_2O_{8+\delta}$ (Bi-2212) is a bilayer cuprate crystal, which means that two CuO_2 planes are present. It belongs to the pervoskite structures with orthorombic distortion. The symmetry group is P/mmm. The inter layer atoms act as charge donators for the copper oxide layers. A more general structure formula is $Bi_2Sr_2Ca_{n-1}Cu_nO_{2n+4+\delta}$, with $n = 1, 2, 3\ldots$ denoting the number of CuO_2 layers. It is known that the highest T_c for layered cuprates exists for n=3. The superconductivity occurs only in ab-planes, but not in c direction. The lattice constant of the CuO_2 planes is $a = b = 5.414$ Å. However, often a 45° tilted unit cell with the lattice parameters $a' = b' = 3.18$ Å is used. Figure 3.12 shows the structure of Bi-2212.
Bi-2212 has been studied by resonance Raman spectroscopy [10, 62, 63]. The good knowledge of its behaviour made Bi-2212 a perfect candidate for time resolved pump and probe Raman spectroscopy described later in this thesis.

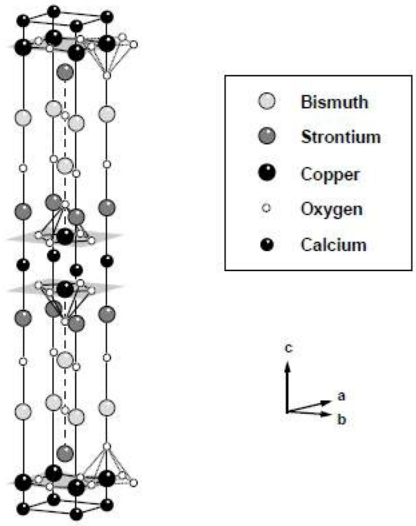

Figure 3.12.: Structure of $Bi_2Sr_2CaCu_2O_{8+\delta}$. [33]

3.3.4. Spin-ladder compounds

$(La, Sr)_{14-x}Ca_xCu_{24}O_{41}$ (SCCO) are so called spin-ladder compound (SLCs). Its basic structure is displayed in figure 3.13. In general the structure of SLC can be seen as a quasi one dimensional two legged ladder, which is orientated along the crystallographic c-axis, separated along the a-axis by $(La, Sr)(Ca)$ atoms from a second quasi one dimensional chain structure along the a direction. Its space group is Cccm. The $(La, Sr)(Ca)$ atoms act as charge donatores to the chain and ladder. Spin-ladder compounds in general are interesting because they exhibit properties such as high temperature superconductivity under pressure [64] , a Wigner-hole crystal [65] and a charge density wave which is stabilised by the misfit between the chain and ladder structure [66]. Its quasi one dimensionality makes SLCs a very good model system to study the interplay between the competing ordering mechanisms leading to the effects described above by a Hubbard model.

The undoped compound SCO (x=0) is intrinsically hole doped with six holes which resemble 3.2 holes in the chain and 2.8 holes at the ladder. The system $La_6Ca_8Cu_24O_{41}$ (LCCO) is a similar system with no intrinsic doping. LCCO was used as an undoped control sample in our study.

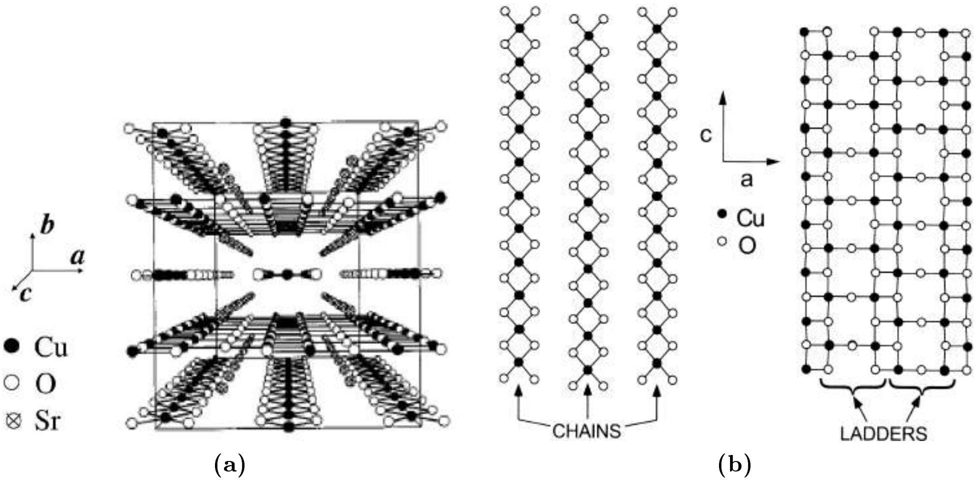

(a) **(b)**

Figure 3.13.: (a) Three dimensional structure of SCO. (b) Separated views of the legged ladder and the chains. The unit cell of SCO consists of ten ladder unit cells and seven chain unit cells [64, 67].

4. Experimental Technique

In this chapter an overview over the time-resolved Raman setup and the VUV-Raman setup at the University of Hamburg and over the VUV-Raman setup at the free electron laser Hamburg is given. For the later also a detailed alignment procedure is discussed.

4.1. Time-resolved Raman spectroscopy

All time resolved Raman data were taken in the laboratory 056 at the Institute of Applied Physics at the Jungiusstraße 11c in Hamburg. The setup for time resolved Raman is located in a clean room laboratory with an average humidity of (40%±2%) and a temperature of ($20\,°C \pm 0.5\,°C$). It was installed as an improvement of the existing steady state Raman experiment in 2007/2008. Details of the setup process and first test with temporal resolution can be found in literature [68, 69, 33]. In the following section a brief overview of the different components of the time resolved Raman setup is given and the data corrections applied to the experimental results are explained.

4.1.1. The setup

For a pump-probe time-resolved Raman setup three components are essential. First two pulsed light sources are required to generate the pump and the probe beam. As a pulsed laser source a Ti:Sapphire laser is used which was pumped by a diode laser. The light of the Ti:Sapphire is then doubled and tripled by a second harmonic / third harmonic generation unit.

As pump laser a *Millenia pro Xs* (Spectra Physics) [70] diode laser with a wavelength of 532 nm with an output power from 2 to 10 Watt is used to pump the Ti:Sapphire laser *Tsunami ps 10W Pump* (Spectra Physics).

The “Tsunami” laser provides a tunable spectral range between 700 nm and 1000 nm. Through mode locking technique it creates ultra short laser pulses with two options for the pulse length, one in the 1 ps range and the other in the 15 ps range. [71, 72]. The output power varies between 1 and 2 Watt. However, the output power and also the pulse width varies depending on the chosen wavelength. In appendix B an overview of the achieved output powers and pulse width is given. The repetition rate of the "Tsunami" laser is 80 MHz. For precise temporal resolution the exact shape of the laser pulses have to be considered and they are given by [72]:

$$I(t) = sech^2\left(\frac{1,76 \cdot t}{\tau_p}\right). \tag{4.1}$$

Here, τ_p denotes the full width half maximum (FWHM) pulse width which in the used time resolved Raman setup was measured by a *Puls check* auto correlator (APE). The measured FWHM pulse width τ_{ac} has to be corrected because the auto correlator assumes a rectangular pulse and not the hyperbolic secant pulse form the "Tsunami" laser. Therefore the rectengular assumed shape by the auto correlator and the real shape have to be convoluted which yields a simple correction factor for the real FWHM of τ_p [72]:

$$\tau_p = 0.648 \cdot \tau_{ac}. \tag{4.2}$$

Furthermore, the power of one pulse can be determined. This is neccesary because only the continuous wave power P_{cw} can be measured in the experiment. The real power in a pulse P_{pulse} is given by

$$P_{pulse} = \frac{P_{cw}}{\tau_p \nu} = \frac{P_{cw}}{0.648 \cdot \tau_{ac} \nu}, \tag{4.3}$$

where ν is the repetition rate. Assuming P_{cw} is 1 Watt and τ_{ac} to 1.5 ps, which are typical values for the laser system, this leads to a pulse power of 12.16 kW, corresponding to a pulse energy of $\sim$ 20 nJ. Table 4.1 summarises the working parameters of the used "Tsunami" laser system. To perform a two colour pump-probe experiment with a single light source the generation of higher harmonic frequencies of the fundamental frequency ω was needed. In this experiment a flexible harmonic generator (FHG), type *GWU-23-PS* (GWU Lasertechnik) is used to achieve frequency doubling and tripling [73]. A detailed description and a manual on how to align this instrument can be found in reference [69].

Spectral range	700 nm - 1000 nm
Average power	$>$ 1,5 W at 800 nm
Pulse width	$>$ 1 ps - 15 ps
Puls energy	20 nJ
Repititionrate	80 MHz

Table 4.1.: Working parameters of the *Tsunami ps 10W Pump.*

The above described laser system provides three for the experiment simultaneously usable wavelengths, the fundamental frequency ω, as well as the higher harmonic

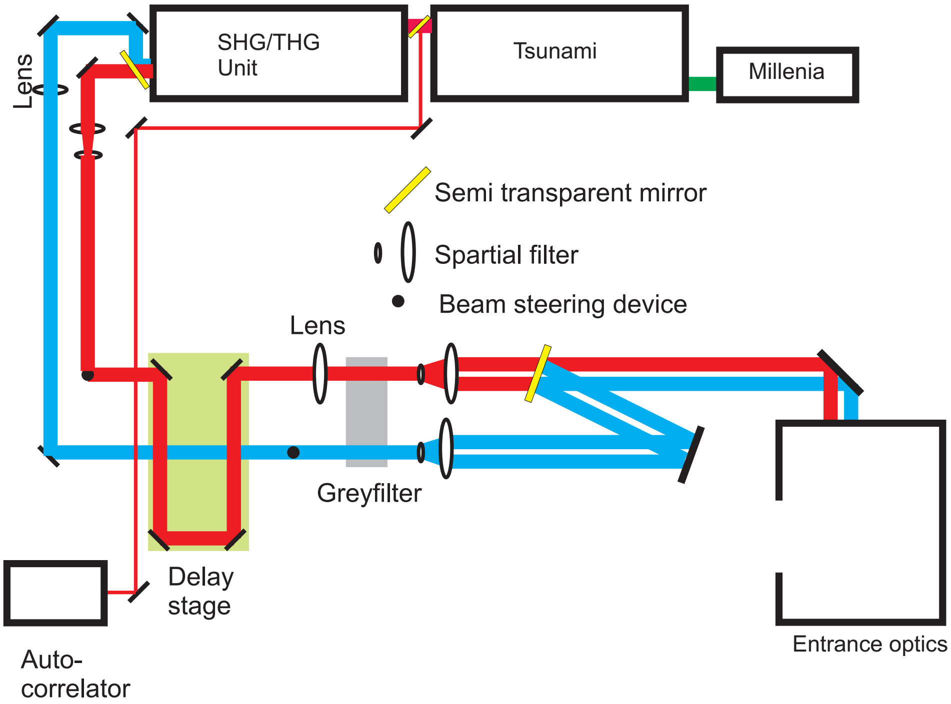

Figure 4.1.: Experimental setup for time-resolved Raman spectroscopy. The red and the blue lines denote the different colours used for time resolved two colour pump probe Raman spectroscopy.

frequencies 2ω (second harmonic generation SHG)and 3ω (third harmonic generation THG). These three wavelengths are spitted into different beam paths by semitransparent mirrors. For the experiments described in this thesis only the ω and 2ω wavelength were used, while the 3ω light was blocked. Figure 4.1 shows the experimental beam path up to the entrance. The ω beam is first scaled down and collimated by a pair of lenses with the focal lengths of 75 mm and 35 mm. This is necessary because the shape provided by the laser system of the beam is neither collimated nor small enough for the optics used in the setup. Over a beam steering device, which rotates the polarisation plane of the laser light, the beam goes through a delay line which consists of two fixed mirrors and two movable mirrors on an optical rail. The delay line is used to achieve the temporal overlap or shift between pulsed pump and probe beam. One centimeter shift in the position of the second an third mirror (see figure 4.1) corresponds to a temporal shift of ± 66 ps between the pulses. For low temporal shifts a micrometer screw is used. After the delay line the ω beam was brought on the optical axis of the spectrometers entrance optics. Via a lens with the focal length of 300 mm it was coupled in a spatial filter, which consists of a “fast” lens with the focal length of 10 mm, a 10 micron pin hole and a “slow” lens with the focal length of 150 mm. The spatial filter provides a round image of the pinhole and widens the beam, which is necessary to acquire the smallest focus

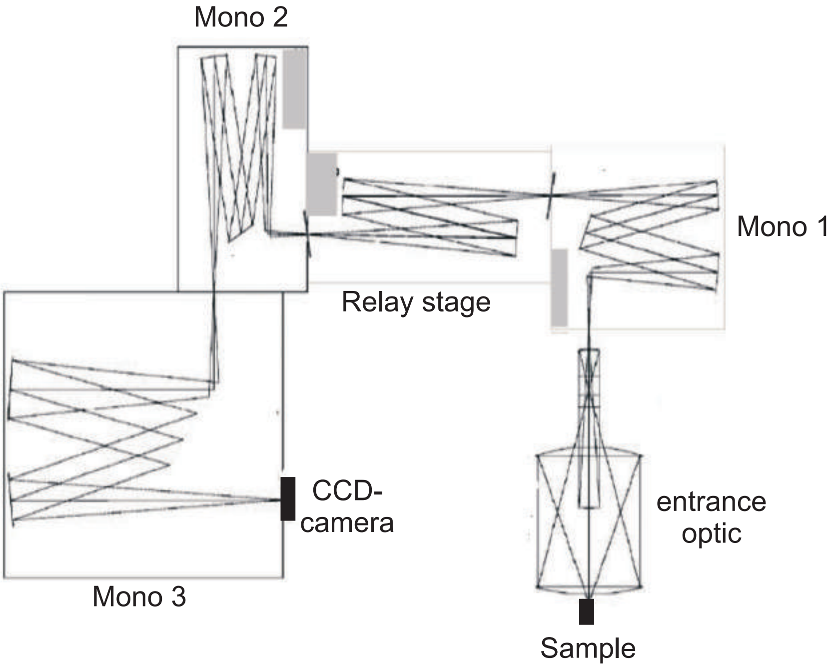

Figure 4.2.: The UT-3 Spectrometer. Mono 1 to 3 denote the first, second and third monochromator [74].

possible at the sample. Behind this filter the beam passes a semi transparent mirror and is guided by two mirrors into the entrance optic. The 2ω beam passes a lens with a focal length of 1000 mm behind the laser system. This lens further collimates the beam which is necessary for the same reasons as for the ω beam. Lead by a mirror the beam passes under the delay stage and is then brought to the optical axis of the spectrometer by a beam steering device, which contrary to the ω beam path does not change the polarisation plane of the light. The 2ω beam gets broadened and shaped by a spatial filter which consists of the same components as the one in the ω beam path. Over a mirror and a semi transparent mirror the 2ω beam is joined with the ω beam and then guided by two mirrors into the entrance optics. The entrance optics focuses the light down to the sample. Typical spot sizes that can be achieved are in the range of 15 to 30 μm, depending on the used wavelength. Larger wavelengths result in a smaller spot size, which is important to note because if the 2ω beam is used as a pump beam the larger ω probe spot also generates Raman scattered light from not pumped sample regions. This has to be taken into account by subsequent data analysis.

Furthermore, a part of the ω beam is taken by a glass reflex between the “Tsunami” laser and the flexible harmonic generator and led by mirrors to the auto correlator to observe the FWHM of the pulses.

Data acquisition is done by the Ultimative Triple 3 (UT-3) Spectrometer. It con-

sists of three monocromators and a relay stage for stray light rejection and has a spectral range from the deep UV (200 nm) to the infrared (800 nm). The first two monochromators are identical and together with the relay stage they act as a pre-monochromator for the third monochromator, which focuses the light at a liquid nitrogen cooled CCD camera. This fully reflective setup allows a great reduction image formation error, like aberrations, astigmatism and coma [75]. The scattered light of the sample is collected by four on axis parabolic mirrors and coupled into the first monochromator through a slit. Over two off-axis parabolic mirrors and a grating a first spectral resolution is acquired in monochromator 1. Through the relay stage and the second monochromator, the light enters the spectrometer which uses a spherical and a toroidal mirror to produce a clear image on the CCD chip. Data acquisition is done by a PC connected to the spectrometer. Figure 4.2 schematically shows the UT-3 spectrometer. Further description can be found in reference [74].
For temperature dependent studies the sample is mounted in a liquid helium cooled cryostat *KONTI cryostat type Spectro 6111* (Cryovac), which allows to rotate the sample by 360 degree.

4.1.2. Data correction

To compare different sets of data several corrections have to be applied to the acquired data. Different laser power and integration times have to be normalised and a correction for the work function of the UT-3 spectrometer, the so called white-light correction [76], has to be applied. Also the electronic background of the CCD camera has to be removed from the spectra. The general formula for these corrections is given by,

$$I_{corr}(\omega) = \frac{I_{raw}(t_{int}, \omega) - I_{Bg}(t_{int})}{I_{cww}(\omega)} \cdot \frac{P_{norm} t_{norm}}{P_m t_{int}}, \tag{4.4}$$

where $I_{corr}(\omega)$ is the corrected intensity of the acquired spectrum, $I_{raw}(t_{int}, \omega)$ the measured spectrum, $I_{cww}(\omega)$ is the white-light correction spectrum, $I_{Bg}(t_{int})$ the background noise of the CCD camera electronics, t_{int} and P_m are the used integration time and power and t_{norm} and P_{norm} are the values the integration time and power are normalised to. Usually t_{norm} is 1 s and P_{norm} is 1 mW. Also artificial signals, so called spikes, which result from cosmic particles traveling through the detector, have to be removed from the spectra. However, all Raman spectra in this thesis have been acquired with the same integration time and power and equation 4.4 simplifies to:

$$I_{corr}(\omega) = \frac{I_{raw}(t_{int}, \omega) - I_{Bg}(t_{int})}{I_{cww}(\omega)}. \tag{4.5}$$

Furthermore, difference spectra have been created for the time resolved pump probe Raman experiment according to the formula:

$$I_{diff}(\omega) = I_{probe}(\omega) - (I_{pump\&probe}(\omega) - I_{pump}(\omega)). \tag{4.6}$$

Here $I_{diff}(\omega)$ is the difference spectrum, $I_{probe}(\omega)$ is the specrum of only the probe beam, $I_{pump}(\omega)$ is the spectrum of only the pump beam and $I_{pump\&probe}(\omega)$ is the spectrum of both beams on the sample. These difference spectra have been normalised by the integrated spectral intensity of just the probe beam by

$$I^{norm}_{diff}(\omega) = \frac{I_{diff}(\omega)}{\int_{\omega} I_{probe}(\omega) d\omega}. \tag{4.7}$$

4.2. VUV-Raman spectroscopy

In this section an overview is given on the setup and the alignment of the VUV-Raman experiment located at the Free-Electron Laser in Hamburg (FLASH) at Deutsches Elektronen Synchrotron (DESY).

4.2.1. The light source FLASH

As light source for the VUV-Raman experiment the FLASH is used. The installation of a VUV free-electron laser at DESY was first proposed in 1996 [77] as an upgrade of the existing TESLA test facility, which is an experimental superconducting linear accelerator constructed at DESY devoted to study and develop parts and components for next generation linear accelerators and X-ray free electron lasers [78]. FLASH is a tunable free electron laser that works with the self amplified spontaneous emission (SASE) principle [79]. FLASH covers an energy range from 4.5 nm to 47 nm with pulse durations from 10 fs to 100 fs. The tuning can be achieved according to the formula,

$$\lambda_{ph} = \frac{\lambda_u}{2\gamma^2}\left(1 + \frac{K^2}{2}\right), \tag{4.8}$$

where λ_{ph} is the wavelength of the emitted photons, λ_u is the periodicity of the undulator, $\gamma = \frac{E}{m_e c^2}$ is the relativistic factor, and $K = \frac{eB_u\lambda_u}{2\pi m_e c}$ is the undulator parameter, with B_u being the peak magnetic field. The tuning is simply achieved by varying the kinetic energy E of the accelerated electrons [80].

The accelerator consists of six cryomodules which bring the electrons to an energy of 1 GeV. After the acceleration stage the electron bunch gets collimated and compressed and the VUV light is generated in an undulator. Figure 4.3 schematically shows the accelerator and undulator stage of FLASH [81]. The light produced in

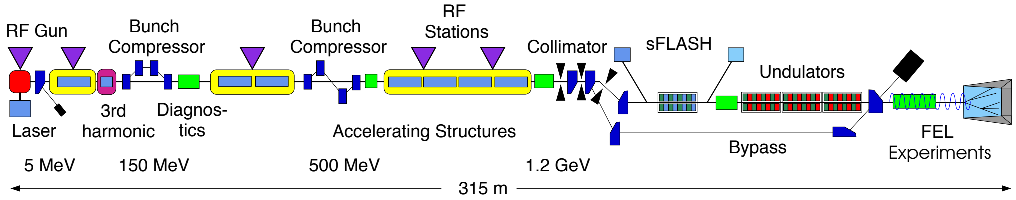

Figure 4.3.: Schematic drawing of the accelerator of FLASH. Figure adapted from reference [81].

the undulator is coupled into one of the five for experiments usable beamlines (PG1, PG2, BL1, BL2, BL3)[1] with a plane mirror (M0). As the VUV-Raman experiment is located at the PG1 beamline and therefore only a description of this beamline will be given in the subsequent section.

4.2.2. The PG 1 Beamline

To direct the beam into the monochromator beamline at FLASH after the M0 mirror the beam goes over a toroidal mirror M1 into the mirror-grating unit [82], which consists of a plane mirror M2 and a plane grating monochromator with two different gratings which can be switched. One of the gratings has 200 lines/mm for the energy range of 20 eV - 200 eV and the other 1000 lines/mm for the energy range of 100 eV - 600 eV with a resolving power $E/\Delta E$ higher than 10^5 [83]. M1 collimates the beam in vertical direction and focuses it in horizontal direction to a point in front of the exit slit. Behind the mirror grating unit, a cylindrical mirror (M3) focuses the beam into the exit slit in vertical direction. The difference in the vertical and horizontal focal points of this mirror system is necessary to reduce the radiation density on the slit blades. After the exit slit a plane mirror M6 steers the beam in a KB pair consisting of two elliptical mirrors, the vertically focusing M7 and the horizontal focusing M8, which focus the beam onto the sample. The calculated spot size at the sample position is 6 μm in horizontal direction and 20 μm in vertical direction [84]. However, in the experiment a spot size of 10 μm in horizontal and $\gg 1$ mm in vertical direction has been achieved. Figure 4.4 shows the ray tracing results for the spot size at sample position. The sample is mounted in a goniometer, which allows 360° rotation of the sample and movement in x, y, and z direction. The incident beam hits the sample with an angle of 10° in regular operation mode. A load lock unit is attached to the experimental chamber, which allows the in vacuum exchange of the sample. A liquid helium cryostat is attached to the sample holder to enable low temperature measurements. In first experiments a temperature of less

---

[1] PG stands fore plane grating, BL for beamline

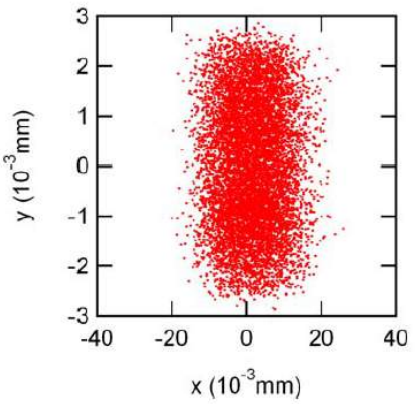

Figure 4.4.: Ray tracing results for the VUV spot size at sample position [84].

than 50 Kelvin at the sample position has been achieved. The UHV in the chamber is generated by an ion getter pump which can achieve pressures up to the 10^{-10} mbar range. A technical drawing of the experimental chamber can be found in appendix C. Furthermore, the sample chamber is equipped with a two-theta stage, which consists of two plane mirrors, which are described in reference [85]. By using this mode of operation different momentum transfers of the incident beam to the sample can be studied. In normal operation mode the angle between the VUV beam hitting the sample and the optical axis of the spectrometer Θ is 100°. That corresponds to a momentum transfer $\Delta\mathbf{k} = 1.53\,\mathbf{k}$. By using the two-theta stage, the scattering angle Θ can be varied between 5° and 175° which correlates to a momentum transfer of $\Delta\,\mathbf{k} = 1.998\,\mathbf{k}$ (quasi back scattering) and $\Delta\,\mathbf{k} = 0.087\,\mathbf{k}$ (quasi forward scattering) respectively. The KB pair as well as the experimental chamber were built by the *BESTEC GmbH* as part of the VUV-Raman spectrometer project at FLASH.

4.2.3. The VUV-Raman spectrometer

The VUV-Raman spectrometer, which was also built by the *BESTEC GmbH* consists of a double monochromator stage, a slit mechanism and a CCD camera. For stray light rejection baffels are mounted between the first monochromator and the slit mechanism which is located in the focus of the first monochromator. Figure 4.5 shows the beampath of the scattered light through the spectrometer.

The solid angle is $1.5 \cdot 10^{-4}\ mrad^2/4\pi$ to obtain a significant amount of scattered photons [85]. The light is collected by the parabolic M1 mirror which has a focal length of 550 mm with the focal point at the sample. The technical details of the mirrors used in the spectrometer can be found in table 4.2. The light is collimated by M1 and directed to the grating. In each monochromator up to four gratings

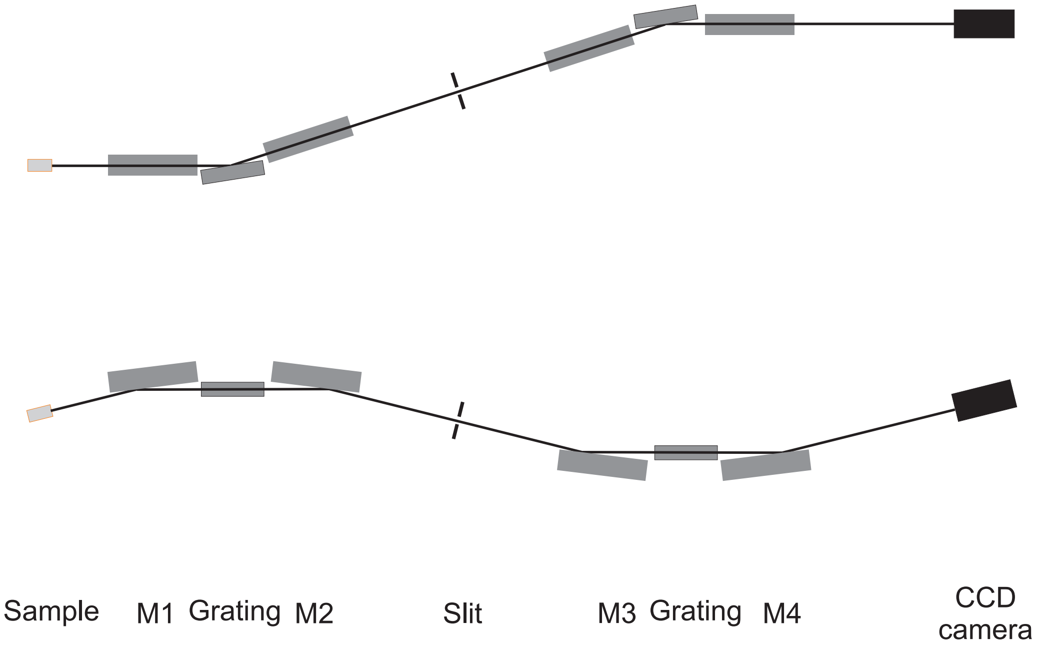

Figure 4.5.: Sketch of the optical scheme of the VUV-Raman spectrometer. Top is a side view, bottom is a top view.

can be mounted which can be switched during normal operations. An overview of the gratings can be found in table 4.3. The parabolic mirror M2 refocuses the dispersed light onto an intermediate slit which acts as an entrance slit for the second monochromator stage. The slit opens symmetrically to the optical axis and allows two modes of operation, a high resolution mode with slit opening in the order of 5 μm, which corresponds to an energy resolution of 20 meV or an huge bandpass mode with an opening of the slit of several mm, which allows to scan an energy range of several eV. In the high resolution mode the slit is also used to block elastic scattered light. The first parabolic mirror M3 of the second monochromator stage collimates the light and deflects it to the second grating. Behind the grating the last parabolic mirror M4 focuses the beam to a Peltier cooled backthinned CCD-camera with a chip size of 2048 x 2048 pixel. The VUV Light is converted by microoptics to visible light.

The included angle D for both monochromator stages is 162°, the angle of incident Θ for all mirrors is 7° and the instrument is working in first order. However, the first stage is working in inside (positive diffraction orders) and the second stage in outside (negative diffraction orders) order. To calculate the diffraction orders the grating equation

$$\frac{m\lambda}{g} = \sin\alpha + \sin\beta \tag{4.9}$$

Name	Length · Width (mm^2)	Focus (mm)
M1	390 · 20	550
M2	375 · 45	1200
M3	375 · 45	1200
M4	390 · 20	1200

Table 4.2.: Overview of the mirrors for the VUV Raman spectrometer [85].

Name	Spectral Range (eV)	Coating	Groove Density (lines/mm)	Blaze angle (°)
G1-1	5-20	Rhodium	80	1.5
G1-2	18-72	Graphite	288	2
G1-3	36-144	Graphite	576	2
G2-1	5-20	Rhodium	170	3
G2-2	18-72	Graphite	612	4
G2-3	36-144	Graphite	1224	4
G2-4	70-210	Rhodium	2380	4

Table 4.3.: Overview of the gratings for the VUV-Raman spectrometer. G1-X belong to the first monochromator stage, G2-X to the second [85].

with α as incident angle, β as diffraction angle, g as the groove density of the grating, m as the diffraction order and λ as the wavelength of the FEL beam has to be solved [86]. By using the the geometry of the Czerny-Turner geometry of the monochromator stages the incident angle can be calculated to

$$\alpha = \arcsin\left(\frac{m\lambda g}{2\cos\frac{D}{2}}\right) + \frac{D}{2}. \tag{4.10}$$

To calculate the resolution limit of the instrument several contributions have to be taken into account. The resolution limit of the monochromator stages is given by

$$\Delta\lambda_{s_1} = \frac{s_1 \cos\alpha}{gmr_1}, \tag{4.11}$$

and

$$\Delta\lambda_{s_2} = \frac{s_2 \cos\beta}{gmr_2}, \tag{4.12}$$

where s_1 is the size of the entrance slit, which is for the first stage the size of the focus of the FEL beam on the sample and for the second stage the size of the intermediate slit, s_2 the size of the exit slit which is for the first stage the size of the intermediate slit and for the second stage the pixel size of the CCD-camera, the distance of the source point of the stage to the first mirror r_1, and the distance r_2 from the second mirror of the stage to the exit slit, which is for the first stage the distance from M2 to the intermediate slit and for the second stage the distance from M4 to the CCD-camera. Furthermore, the resolution is limited by the slope errors of the parabolic mirrors and the gratings. For the gratings this can be calculated by

$$\Delta\lambda_g = \frac{2\sigma_g}{gm}\cos\left(\frac{\alpha+\beta}{2}\right)\cos\left(\frac{\alpha-\beta}{2}\right), \tag{4.13}$$

with σ_g as the slope error of the gratings. For the first mirror of each stage the resolution is given by

$$\Delta\lambda_{m1} = \frac{2\sigma_m\cos\alpha}{gm}\cos\Theta, \tag{4.14}$$

and for the second mirror of each stage by

$$\Delta\lambda_{m2} = \frac{2\sigma_m\cos\beta}{gm}\cos\Theta, \tag{4.15}$$

with σ_m as its slope error. The overall resolution limit is acquired by the sum over equation 4.11 to 4.15, i.e.

$$\Delta\lambda = \sqrt{\sum_i \Delta\lambda_i^2}. \tag{4.16}$$

Figure 4.6 shows the design value resolution for the two monochromator stages in inside outside geometry calculated with typical slope errors and slit sizes and groove densities. Also a breakdown of the different contributions is denoted. The reciprocal linear dispersion of the monochromator stages can be calculated by

$$P = \frac{E\cos\beta}{\lambda gms_2}, \tag{4.17}$$

where λ is the wavelength of the FEL beam and E the energy of the FEL beam. The whole spectrometer is housed in UHV chambers and a vacuum up to 10^{-8} mbar is achieved by ion getter pumps. The incident angle of the gratings, the position of the gratings i.e. which grating is used, the width of the intermediate slit, the distance of the camera after M4 and the y position of the M1 to M3 can be varied by high precision step motors and the yaw of the gratings by wobble sticks under vacuum conditions. For data acquisition and operating the instrument a PC is used.

4.2.4. Alignment procedure of the monochromator stages

In this section the basic optical alignment procedure of the two monochromators of the VUV-Raman spectrometer is described. The alignment had to be performed twice due to a technical malfunction causing a dealignment of the instrument. It has been constantly improved as it took place. As a light source for this procedure a *Laser Unequal Pathlength Interferometer System (LUPI) by SORL* was used. The monochromator optics were either aligned in back reflection geometry to interference

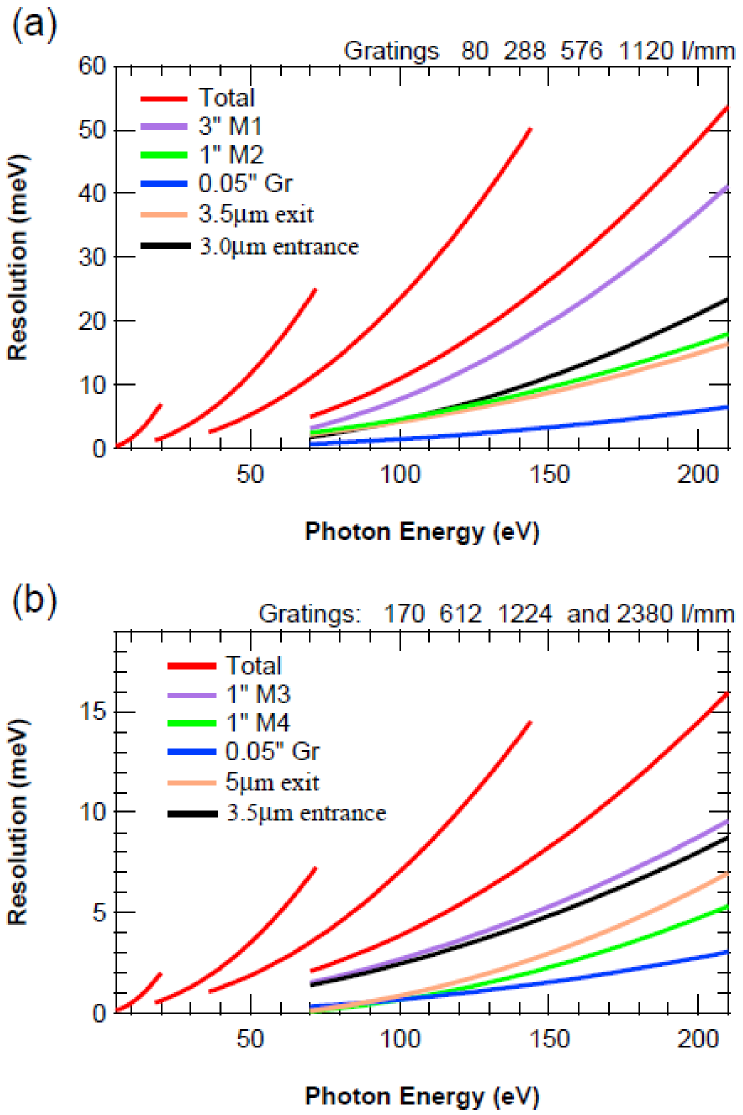

Figure 4.6.: (a) Resolution of the first monochromator stage calculated for four different gratings. Red is the total resolution, violet the contribution of M1 with a slope error of 3 arcseconds, green the contribution of M2 with a slope error of 1 arcsecond, blue the contribution of the grating with a slope error of 0.05 arcseconds, yellow is the contribution of an 3.5 μm intermediate slit and black the contribution of a 3 μm spot size. (b) Resolution of the second monochromator stage calculated for four different gratings. Red is the total resolution, violet the contribution of M3 with a slope error of 1 arcsecond, green the contribution of M4 with a slope error of 1 arcsecond, blue the contribution of the grating with a slope error of 0.05 arcseconds, yellow is the contribution of a 5 μm exit slit i.e. pixel size of the CCD-camera and black the contribution of a 3.5 μm intermediate slit size. This figure is taken from the description of the VUV-Raman spectrometer [85].

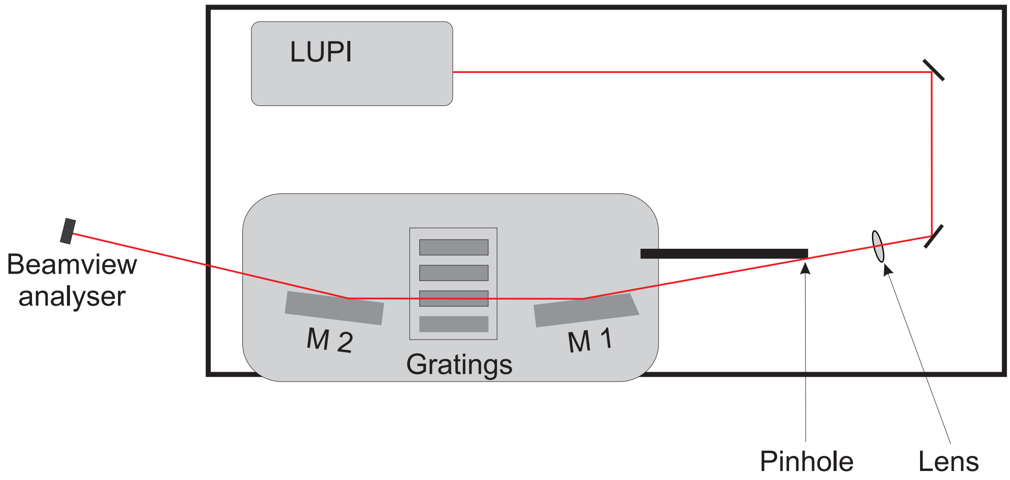

Figure 4.7.: Sketch of the setup used for the allignment of the first monochromator stage.

fringes or by checking the resulting spot formation by a *Lasercam-HR (RoHS) by Coherent* beam view analyser. The basic alignment setup for the first monochromator stage is displayed in figure 4.7, technical drawings of the monochromator stages can be found in appendix C. In general the procedure is very complex due to the many degrees of freedom, the long optical path and the required precision in the micrometer range. Table 4.4 specifies the degrees of freedom for each optical element. The overall procedure took place in a cleanroom laboratory at the Institute of Applied Physics in Hamburg.

Optical element	Degrees of freedom
M1, M2, M3	x, y, z, pitch, roll, yaw
M4	x, z, pitch, roll, yaw
Gratings	x, z, pitch, roll, yaw

Table 4.4.: Degrees of freedom for the optical elements of the VUV-Raman spectrometer.

In the following a step by step description of the procedure is given for the first monochromator stage. The second monochromator stage is aligned in an equal fashion. Differences will be discussed later in this section.

1. Levelling of the optical tables. This is done by using a high precision water level with an accuracy of 0.02 mm per meter. It is important to note, that this precision is in the order of the flatness of the optical tables surface. Therefore it is required to choose at least two different spots on the table where the calibration takes place.

2. Positioning of the baseplate on the optical table with the long edge parallel to the long edge of the table.

3. Levelling of the baseplate. As in step 1, two fixed spots for the levelling procedure are required for the same reason as for the optical table.

4. Set up the alignment beampath according to figure 4.7. For the alignment of the first mirror M1 the following steps have to be taken:

    a) The gratings have to be put in back reflexion stance i.e. they have to be positioned perpendicular to the normal beampath. To verify that the gratings in their holders are exactly in the right position, the gratings have to be calibrated to optimal interference fringes by the LUPI using a reference beampath. This beampath consists of an optical rail, which has to be parallel to the long edge of the baseplate, and a moving iris on it, to ensure that this beampath is parallel to the optical table and perpendicular to the small edge of the baseplate.

    b) The angle of incident to the first mirror has to be 14° in respect to the long baseplate edge. To achieve the right angle of incident the front edge of the mirror M1 is phased 14° (see figure C.4). The LUPI beam has to be put on this edge and by changing pitch and yaw of the M1 mirror this mirror is aligned to optimal interference fringes.

    c) The LUPI beam has to be focused with a 300 mm lens in a 50 μm pinhole, which is located at the position of the sample, i.e. the focus position of the PG 1 beamline. For positioning of the pinhole, a reference arm can be mounted to the baseplate (provided by BESTEC) (see figure C.2).

    d) The M1 mirror has to be aligned by varying the x-, y-, z- and the roll of the mirror, in a way that the center of the beam hits the pole of M1 and that the back reflected beam is again focused in the pinhole. This is the most complicated step in the whole procedure and requires extreme patients and precision, because the back reflex can not be tract easily. In an optimal case it is possible to acquire good parallel interference fringes. However, this has never been achieved in through the pinhole. During this alignment procedure it is helpful to remove the pinhole from time to time to see the interference pattern more clearly and get a better feedback of the current state. It is also important to note, that the height of the beam is correct i.e. that the gratings are hit symmetrically around their pitch rotational axis. If this is not the case or a good alignment can only be achieved in with a mirror position which is close to the alignment limits,

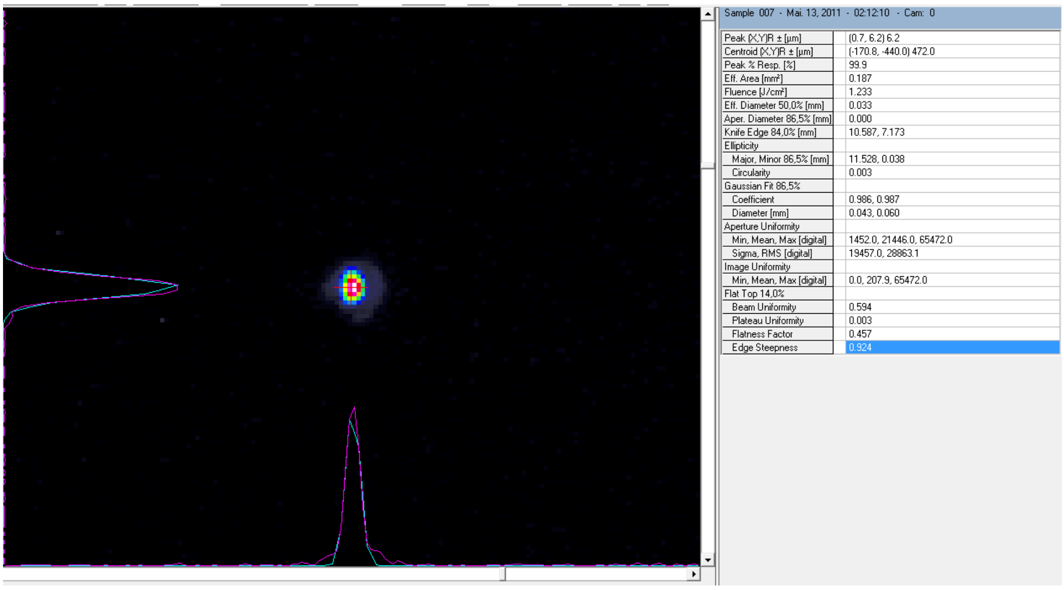

Sample 007 - Mai. 13, 2011 - 02:12:10 - Cam: 0

Peak (X,Y)R ± [µm]	(0.7, 6.2) 6.2
Centroid (X,Y)R ± [µm]	(-170.8, -440.0) 472.0
Peak % Resp. [%]	99.9
Eff. Area [mm²]	0.187
Fluence [J/cm²]	1.233
Eff. Diameter 50,0% [mm]	0.033
Aper. Diameter 86,5% [mm]	0.000
Knife Edge 84,0% [mm]	10.587, 7.173
Ellipticity	
Major, Minor 86,5% [mm]	11.528, 0.038
Circularity	0.003
Gaussian Fit 86,5%	
Coefficient	0.986, 0.987
Diameter [mm]	0.043, 0.060
Aperture Uniformity	
Min, Mean, Max [digital]	1452.0, 21446.0, 65472.0
Sigma, RMS [digital]	19457.0, 28863.1
Image Uniformity	
Min, Mean, Max [digital]	0.0, 207.9, 65472.0
Flat Top 14,0%	
Beam Uniformity	0.594
Plateau Uniformity	0.003
Flatness Factor	0.457
Edge Steepness	0.924

Figure 4.8.: Spot formation of the LUPI beam over the blank at the focal point of the M2 mirror. Screenshot taken from the Beamview analyser software version 4.2.2. The spot size (effective diameter 50%) is 33 μm.

the pitch and the yaw have to be readjusted and therefore steps 4b to step 4d have to be performed again.

5. After M1 is sufficiently adjusted, the gratings have to be put back in normal position. It is important, that the gratings are recalibrated because the movement of the gratings from back reflection to normal position usually destroys their alignment. This readjustment is achieved by building a reference beampath from the LUPI which hits the gratings vertically from the top. To assure perpendicular irradiation, a reference mirror is adjusted with a water level and placed above the gratings so that the beampath can be calibrated to interference fringes. To insure that the gratings are exact at the required height, a reference laser is coupled through the pitch rotational axis of the gratings. The height is correct if this round laser beam is exactly cut in half.

6. Now, the gratings are put in zeroth order, which means to 9°. They should be completely illuminated by the LUPI beam so that the optical surface of the M2 mirror also is full illuminated.

7. The beam view analyser camera has to be installed in the focal point of the M2 mirror in a fashion, that a scanning through the focal point is possible to analyse the shape of the focus. For this a support structure was planned and attached to the baseplate. It has to be considered that optical axis at this part of the spectrometer is tilted by 17.4° vertically and 14° horizontally in respect to the plane of the baseplate. The focal point of M2 is ~ 889 mm behind and

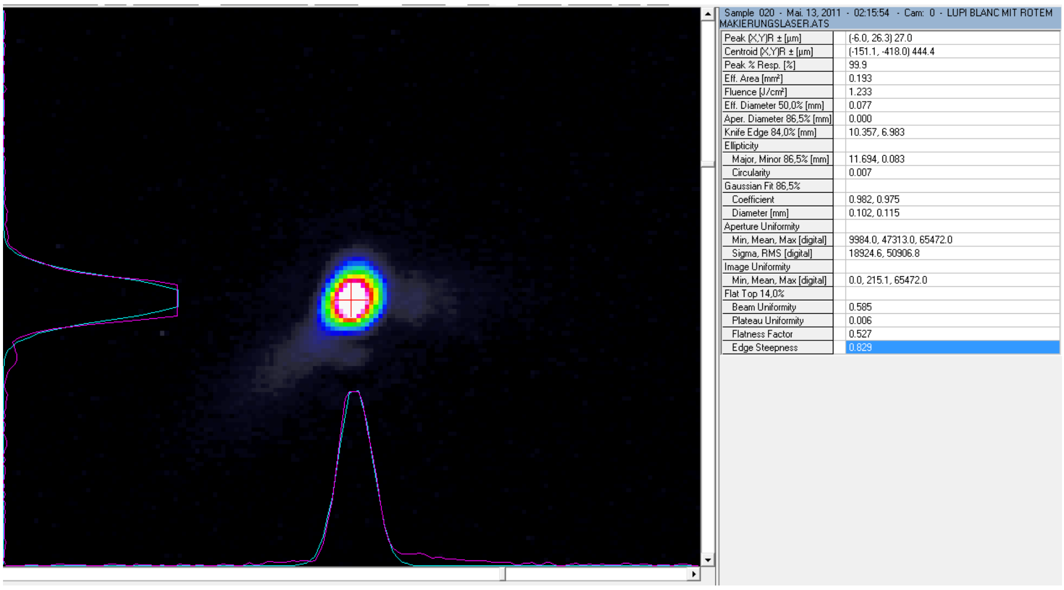

Sample 020 - Mai. 13, 2011 - 02:15:54 - Cam: 0 - LUPI BLANC MIT ROTEM MAKIERUNGSLASER.ATS

Peak (X,Y)R ± [µm]	(-6.0, 26.3) 27.0
Centroid (X,Y)R ± [µm]	(-151.1, -418.0) 444.4
Peak % Resp. [%]	99.9
Eff. Area [mm²]	0.193
Fluence [J/cm²]	1.233
Eff. Diameter 50,0% [mm]	0.077
Aper. Diameter 86,5% [mm]	0.000
Knife Edge 84,0% [mm]	10.357, 6.983
Ellipticity	
Major, Minor 86,5% [mm]	11.694, 0.083
Circularity	0.007
Gaussian Fit 86,5%	
Coefficient	0.982, 0.975
Diameter [mm]	0.102, 0.115
Aperture Uniformity	
Min, Mean, Max [digital]	9984.0, 47313.0, 65472.0
Sigma, RMS [digital]	18924.6, 50906.8
Image Uniformity	
Min, Mean, Max [digital]	0.0, 215.1, 65472.0
Flat Top 14,0%	
Beam Uniformity	0.585
Plateau Uniformity	0.006
Flatness Factor	0.527
Edge Steepness	0.829

Figure 4.9.: Spot formation of the focal point marking laser at the of the M2 mirror. Screenshot taken from the Beamview analyser software version 4.2.2. The spot size (effective diameter 50%) is 77 μm.

$\sim 696\ mm$ above the baseplate (see figure C.2).

8. Now, M2 has to be aligned by adjusting x, y, z position, as well as pitch, roll and yaw while looking at the image provided by the beam view analyser. It is very important that the spot is round, in front of and behind the focal point. At the position of the focal point of M2 the slit mechanism is supposed to be. A small derivation of the position could cause the beam hitting the vacuum tubes and therefore not entering the second monochromator anymore because of the long beampath between the M2 and M3 mirror (2.4 m). However, the alignment of M2 is much easier compared to the one of M1 due to the fact, that a real time image of the spot formation can be observed. It is also important to note, that due to the different focal lengths of M1 and M2 mirrors, a magnification of 2.18 in the spot size should be observed. During the alignment a spot size of 33 μm was achieved after M2, which is the same size as the focus before M1. This is because of the bad reflectivity of the mirrors and the gratings in the visible [85]. A picture of the spot achieved after M2 can be found in figure 4.8.

9. A last adjustment of the gratings has to be done to verify, that on all gratings the spot after the M2 mirror is at exactly the same position and of the same shape. This can be achieved with a precision of roughly one camera pixel, i.e. $\sim 5\ \mu m$. For the first and second baseplate the spot sizes and positions can be found in appendix D.

10. The last step of the alignment is to mark the optical path and the focal points

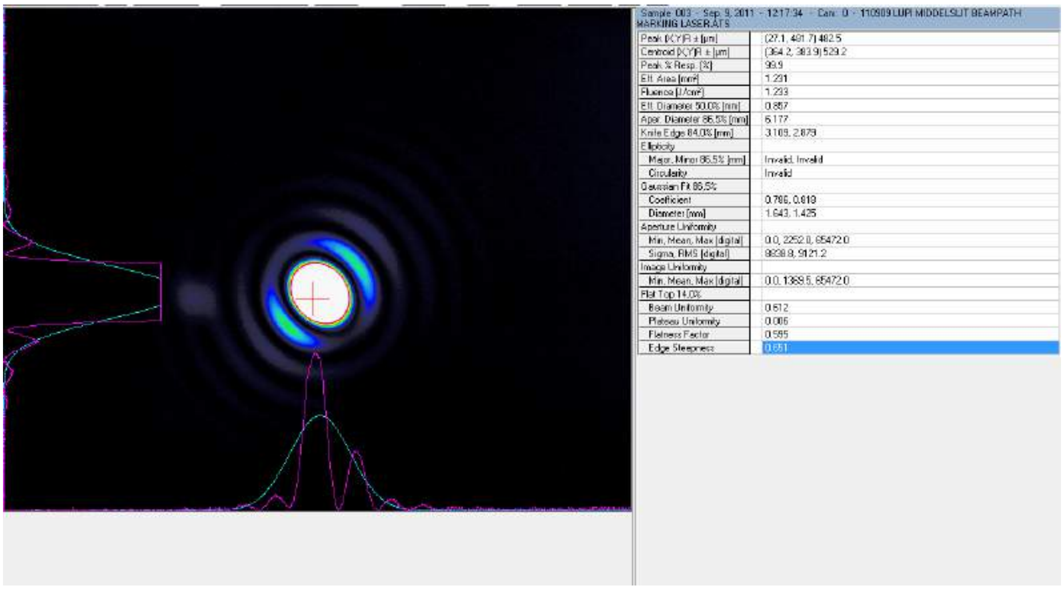

Sample 003 - Sep. 9, 2011 - 12:17:34 - Cam: 0 - 110909 LUPI MIDDELSLIT BEAMPATH MARKING LASER.ATS

Peak [X,Y]R ± [µm]	(27.1, 491.7) 482.5
Centroid [X,Y]R ± [µm]	(364.2, 383.9) 529.2
Peak % Resp. [%]	99.9
Eff. Area [mm²]	1.231
Fluence [J/cm²]	1.233
Eff. Diameter 50.0% [mm]	0.857
Aper. Diameter 86.5% [mm]	6.177
Knife Edge 84.0% [mm]	3.109, 2.879
Ellipticity	
Major, Minor 86.5% [mm]	Invalid, Invalid
Circularity	Invalid
Gaussian Fit 86.5%	
Coefficient	0.786, 0.819
Diameter [mm]	1.643, 1.425
Aperture Uniformity	
Min, Mean, Max [digital]	0.0, 2252.0, 65472.0
Sigma, RMS [digital]	9838.9, 9121.2
Image Uniformity	
Min, Mean, Max [digital]	0.0, 1369.5, 65472.0
Flat Top 14.0%	
Beam Uniformity	0.612
Plateau Uniformity	0.006
Flatness Factor	0.595
Edge Steepness	0.651

Figure 4.10.: Spot formation of the beampath marking laser at the focal point of the M2 mirror. Screenshot taken from the Beamview analyser software version 4.2.2. The spot size (effective diameter 50%) is 857 μm.

of the M1 and M2 mirror for transport and later alignment at FLASH. For marking the focal points of M1 and M2, two separate lasers with specific optics have been attached to the baseplate. The optics are necessary to provide a sufficient small size of the marking spot, which is in the range of the LUPI spot size. However, these marking lasers are not on the optical axis of the instrument. Therefore, two additional lasers have been installed to mark the optical axis of the instrument. Due to space constraints it was not possible to attach additional optics to this lasers to decrease the beam size. An exemplary picture of the size of the marking laser focus and of the optical axis denoting laser can be found in figures D.6 and 4.10. Additional photos of the setup can be found in appendix D.

For the alignment of the second monochromator stage the main difference was, that it took place by aligning M4 before M3. The alignment setup displayed in figure 4.7 has to be rearranged in a way, that the pinhole is in the focal point of the M4 mirror. Also a 500 mm focal length lens has to be used to illuminate M4 completely. Step 5 has to be skipped because there was no sufficient way to mount a reference mirror due to the top down design of the grating holder in this stage. For step 8 it is also important to note that no spot magnification is expected. A picture of the spot formation after the alignment and additional photos can be found in appendix D. Also on the second baseplate only marking lasers for M3 have been attached.

5. Results

In this chapter an overview of the experimental results is given. At first a proof of the existance of a peroxo-core responisible for electron transfer is given by the investigation of isotope Raman shift. Secondly, the results of steady state Raman spectroscopy at Cu^I and Cu^{II} complexes are discussed. A resonance study is presented which indicates that both complexes resonate at 3.4 eV and at 4.45 eV. These resonances can be related to vibrational modes which are connected to structures of both oxidation states in a charge transfer process.

Thirdly an analysis of the time-resolved Raman results of multiferroic compound $La_{1-x}Ca_xMnO_3$ (LCMO) is given. The focus of interest is the temporal evolution of melting and recombination of the charge ordered state of the 50 % doped sample by observing a pump introduced suppression of a Jahn-Teller mode. These results are compared to two different doped samples (55 % and 76%) and a possible mechanism of the melting is presented.

In the subsequent section the results of the time-resolved Raman study on the high temperature superconducting compound $Bi_2Sr_2CaCu_2O_8$ (Bi-2212) is presented. The focus of this study is the observation of the light introduced melting and recombination of the superconducting state, by observing the temporal evolution of the pair breaking peak. The results are compared to theory and related to two different mechanisms indicating the nature of the superconducting order parameter Δ.

Finally the results of the VUV-Raman experiment performed at the FLASH light source in Hamburg are given. At first the results of calibration of the energy axis using the elastic scattered response of Silicone is shown and the principle of the calibration is discussed. Afterwords the first results on the intrinsically hole doped cuprate compound $Sr_{14-x}Ca_xCu_{24}O_{41}$ (SCCO) are presented. The goal of this study is to understand the hole pairing mechanism. For comparison the undoped sample $La_6Ca_8Cu_{24}O_{41}$ (LCCO) is discussed. A theory for the scattering Hamiltonian is presented and a possible Raman matrix element is discussed.

5.1. Bio inorganic copper complexes

To investigate which electronic configuration of the bio inorganic model system is responsible for electron transfer in the phenol hydroxylation process a Raman study at 412 nm incident photon energy has been performed. For this study the samples were created directly before the measurement, and cooled with liquid nitrogen to avoid degradation that occurs at room temperature within seconds. Figure 5.1 shows the degeneration of the sample $[Cu_2O_2(HC(3-tBuPz)_2(Py))_2](SbF_6)_2$ solved in dichloromethane. It is obvious that after 30 seconds of measurement at room temperature, a clear signal could be obtained. Subsequent measurements show a gradual degradation in signal strength and after 150 seconds under room temperature atmosphere almost no signal could be obtained anymore.

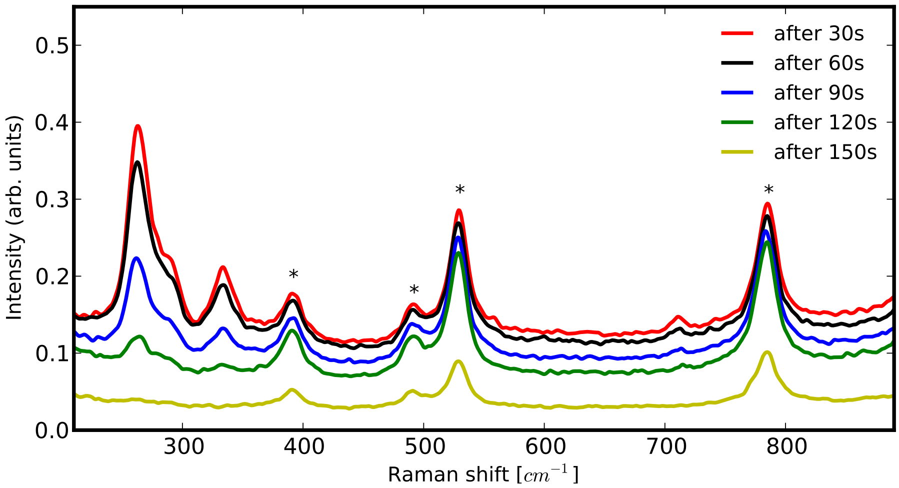

Figure 5.1.: Sample degradation of $[Cu_2O_2(HC(3-tBuPz)_2(Py))_2](SbF_6)_2$ in dichloromethane. Asterixes mark solvent peaks. The sample initially was synthesised at -78 °C. Due to heating of the sample caused by room temperature environment the system degrades gradually. The sample shown was synthesised with O_{18}.

Despite the decrease in signal the initial measurement is strong enough to compare Isotope shifts of oxygen. Figure 5.2 shows the initial measurement of the same compound synthesised with O_{16} and O_{18} respectively. The peak at 750 cm^{-1} in the O_{16} spectra can be related via time-dependent density functional theory to a characteristic O-O stretch [87]. Upon O_{18} substitution, this mode shifts 39 cm^{-1} to lower energies (see insert). This is a clear evidence for the formation of a peroxo state in this compound and therefore proofs the proposed scheme of phenol hydroxylation.

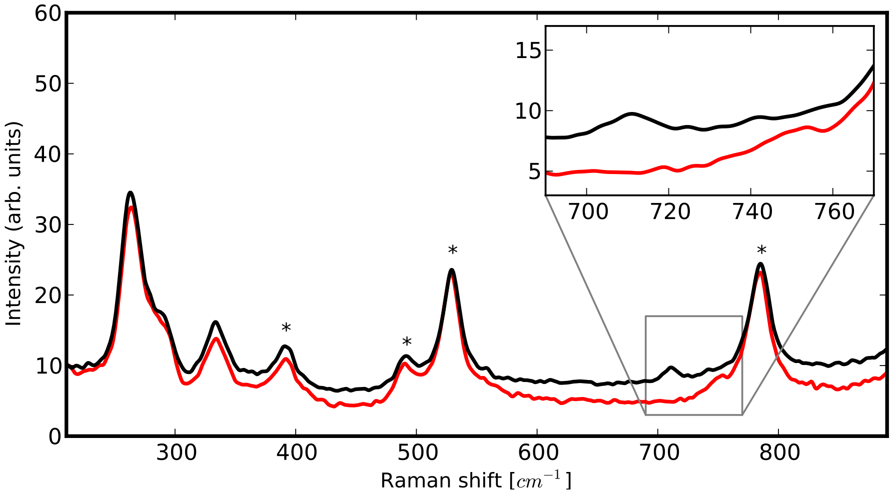

Figure 5.2.: Comparison of $[Cu_2O_2(HC(3-tBuPz)_2(Py))_2](SbF_6)_2$ synthesised with O_{16} (red) and O_{18} (black). An isotope shift of the mode at 750 cm^{-1} by about 39 wavenumbers to lower energies could be observed. The insert shows the relevant peak enlarged. The sample was solved in dichloromethane.

Furthermore, a resonance study with a series of bis(chelate) Cu^I and Cu^{II} complexes has been performed .to contribute to the investigation of their structure and resonance profiles have been obtained. Figure 5.3 show exemplarily the obtained Raman spectra of $[Cu(TMGqu)_2]CF_3SO_3$ (1) (a) which has a Cu^I oxidation state at 2,97 eV incident photon energy and $[Cu(TMGqu)_2](CF_3SO_3)_2$ (2) (b) which has a Cu^{II} oxidation state at 4,46 eV incident photon energy. (c) and (d) depict the Raman cross section of the observed Raman peaks depending on incident photon energy. The oxidation states of the samples were determined by X-ray absorption spectroscopy (see **Paper II** for details). In both complexes two different resonances were found at 3.4 eV and 4.45 eV for most of the peaks in both Cu^I and Cu^{II} oxidated cores. A density functional theory (DFT) analysis reveals that the 788 cm^{-1} (purple triangle) mode found in (1) and (2) is a vibrational $Cu-N_{gua}$ stretching and chelate angle torsion mode. Furthermore, the resonance at 3.4 eV couples to MLT charge transfer form Cu^I to Cu^{II} and a LTM charge transfer from Cu^{II} to Cu^I [88]. Thus, the 788 cm^{-1} mode connects the Cu^I and Cu^{II} oxidation state. This proves that the entatic transition state is directly optically accessible and therefore the reaction coordinate can directly be observed by Raman spectroscopy.

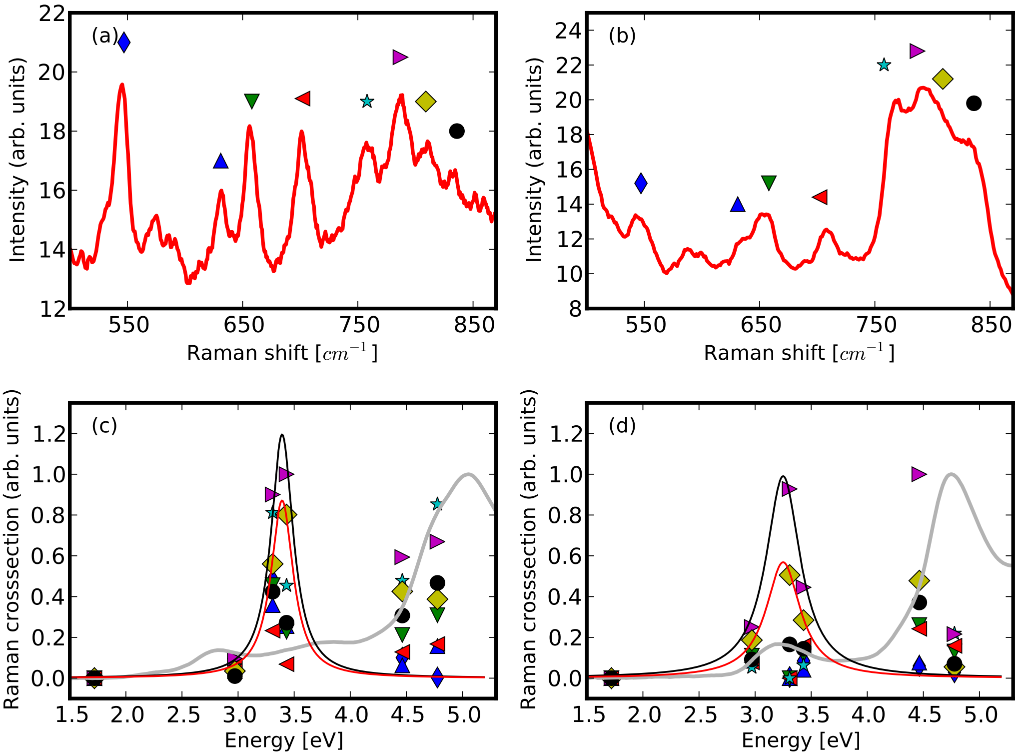

Figure 5.3.: (a) Raman spectrum of $[Cu(TMGqu)_2]CF_3SO_3$ (1) at an excitation energy of 2.97 eV. (b) Raman spectrum of $[Cu(TMGqu)_2](CF_3SO_3)_2$ (2) at an excitation energy of 4.46 eV. (c) Dependence of the Raman intensity on incident photon intensity of (1). (d) Dependence of the Raman Intensity on incident photon intensity of (2). The markers were used to indicate Raman peaks and their resonance behaviour, the gray line denotes the absorption spectrum, and the coloured lines are a guides to the eye. As solvent MeCN was used and the incident photon energies were 1.72 eV, 2.97 eV, 3.31 eV, 3.43 eV, 4.46 eV and 4.78 eV.

Paper I

Catalytic Phenol Hydroxylation with Dioxygen: Extension of the Tyrosinase Mechanism beyond the Protein Matrix

Alexander Hoffmann, Cooper Citek, Stephan Binder,
Arne Goos, Michael Rübhausen, Oliver Troeppner,
Ivana Ivanović-Burmazović, Erik C. Wasinger, T.
Daniel P. Stack, and Sonja Herres-Pawlis

Angewandte Chemie ***125****, 5508–5512 (2013)*

Angewandte Communications

Tyrosinase Model

DOI: 10.1002/anie.201301249

Catalytic Phenol Hydroxylation with Dioxygen: Extension of the Tyrosinase Mechanism beyond the Protein Matrix**

Alexander Hoffmann, Cooper Citek, Stephan Binder, Arne Goos, Michael Rübhausen, Oliver Troeppner, Ivana Ivanović-Burmazović, Erik C. Wasinger, T. Daniel P. Stack, and Sonja Herres-Pawlis**

A pinnacle of bio-inorganic chemistry is the ability to leverage insights gleaned from metalloenzymes toward the design of small analogues capable of effecting catalytic reactivity outside the context of the natural system.[1,2] Structural mimicry of active sites is an attempt to insert a synthetic catalyst into an enzymatic mechanism. Such a mechanism evolves by selection pressures for efficiency and traverses an energetic path, with barriers and wells neither too high nor too deep in energy—a critical factor of catalytic turnover.[3] An advantage of metalloenzymes over small metal complexes is the site-isolation of the metal center in the protein matrix and the attendant ability to attenuate destructive decay processes—reaction sinks. This protection provides access to thermal regimes that allow barriers and wells to be traversed. Synthetic complexes too must avoid any deleterious reactions, often necessitating the deliberate incorporation of protective superstructures.[4,5] Such limitations make reproducing enzymatic catalytic reactivity in a synthetic complex with native substrates a significant challenge, as evidenced by the dearth of good examples, despite decades of effort.

The intellectual investment of translating a catalytic mechanism from an active site to a synthetic system is justified by a comparison of Nature's dexterity with dioxygen to perform catalytic monooxygenase-type chemistry[6–9] and the dependence of synthetic chemists on exotic reagents for oxygen-atom insertion reactions. Tyrosinase is a ubiquitous dinuclear copper enzyme that catalyzes the hydroxylation of phenols to catechols and the subsequent oxidation of catechols to quinones by activating dioxygen in the form of a side-on-bonded peroxide dicopper(II) species, crystallographically[10] and spectroscopically identified.[11,12] The seemingly simple, regiospecific transformation mediated by tyrosinase is not reproduced easily by synthetic methods, though its importance has been acknowledged by recent efforts to move beyond stoichiometric oxidants,[13] as these sometimes multistep syntheses are often low to moderate yielding and frequently unselective.[14–17] Limited examples of stoichiometric phenolate hydroxylation exist with synthetic, tyrosinase-like side-on peroxide complexes[18–22] formed by oxygenation of copper(I) complexes. Only two complexes achieve significant catalytic phenol hydroxylation using dioxygen: a dinucleating, polydentate imine complex reported by Réglier et al.,[23] and a mononucleating analogue reported by Tuczek et al.[24] both capable of roughly 16 turnovers in the presence of triethylamine. Neither study could identify an operative oxygenated copper species, presumably precluding a more detailed mechanistic analysis of the key substrate hydroxylation step. The possibility of a synthetic side-on peroxide as a catalytic oxidant is suggested by the work of Casella et al. with a dinucleating copper benzimidazole complex, achieving 1.2 turnovers with readily oxidized phenols.[21,25]

---

[*] Dr. A. Hoffmann, Prof. Dr. S. Herres-Pawlis
Department of Chemistry
Ludwig-Maximilians-Universität München
81377 Munich (Germany)
and
Fakultät Chemie, Technische Universität Dortmund
44227 Dortmund (Germany)
E-mail: sonja.herres-pawlis@cup.uni-muenchen.de

C. Citek, Prof. Dr. T. D. P. Stack
Department of Chemistry, Stanford University
Stanford, CA 94305 (USA)
E-mail: stack@stanford.edu

Dr. S. Binder, A. Goos, Prof. Dr. M. Rübhausen
Institute for Applied Physics
and Center for Free Electron Laser Science
University of Hamburg (Germany)

O. Troeppner, Prof. Dr. I. Ivanović-Burmazović
Department of Chemistry and Pharmacy
University of Erlangen-Nuremberg (Germany)

Prof. Dr. E. C. Wasinger
Department of Chemistry and Biochemistry
California State University, Chico, CA 95929 (USA)

[**] A.H., S.B., A.G., M.R., and S.H.-P. thank the Deutsche Forschungsgemeinschaft (FOR 1405) for financial support. S.H.-P. gratefully acknowledges the Fonds der Chemischen Industrie for a Liebig fellowship, the Bundesministerium für Bildung und Forschung initiative MoSGrid (01IG09006) for computational support, and Prof. Dr. K. Jurkschat for valuable advice. I.I.-B. and O.T. gratefully acknowledge support through the "Solar Technologies Go Hybrid" initiative of the State of Bavaria. Financial support was provided by the U.S. National Institutes of Health (NIH; GM50730) for T.D.P.S. and the William R. and Sara Hart Kimball Stanford Graduate Fellowship for C.C. E.C.W. thanks the CSU Chico College of Natural Sciences for financial support and release time to support this work. Portions of this research were carried out at the Stanford Synchrotron Radiation Laboratory, a national user facility operated by Stanford University on behalf of the U.S. Department of Energy, Office of Basic Energy Sciences.

Supporting information for this article (including materials and methods, synthetic procedures, Raman measurements, XAS spectroscopy details, TD-DFT details, and optimized coordinates of **1**) is available on the WWW under http://dx.doi.org/10.1002/anie.201301249.

Here we report a synthetic catalyst capable of hydroxylating a wide variety of phenols using dioxygen that proceeds through a room-temperature (RT)-stable analogue of oxygenated tyrosinase—a side-on peroxide complex, which possesses ligation and spectroscopic attributes similar to those of the enzymatic active site. Efficient stoichiometric oxidation of phenolates to catecholates at −78 °C is shown, as well as catalytic oxidation of phenols to quinones at room temperature with triethylamine, through a reaction pathway consistent with the generally accepted enzymatic mechanism.[11] Conditions are described in which catalytic turnover is halted and restored at a proposed catecholate–product adduct. This investigation demonstrates that simple structural mimicry suffices to not only transfer the inherent enzymatic catalytic reactivity into a synthetic complex, but that bioinspiration is a viable stategy of pursuing selective transformations of substrates beyond scope of the enzyme.[26]

Oxygenation of [Cu^I{bis(3-*tert*-butyl-pyrazolyl)pyridylmethane}]SbF$_6$ in dichloromethane at −78 °C results in near-quantitative formation (vide infra) of [Cu_2O_2(HC(3-*t*BuPz)$_2$(Py))$_2$](SbF$_6$)$_2$ (**1**), a side-on peroxide dicopper(II) complex (Figure 1 A), as evidenced by the characteristic O–O stretch in its resonance Raman spectrum at 750 cm^{-1}, which shifts by 39 cm^{-1} upon $^{18}O_2$ substitution (Figure 1 C).[27,28] The expected mass signature and isotope pattern observed in the cryo-ESI-TOF mass spectrum also shifts appropriately upon oxygenation with $^{18}O_2$ (Figure S3 in the Supporting Information). The ligand-to-metal-charge-transfer (LMCT) features at 350 nm (20 mM^{-1}cm^{-1}) and 550 nm (1 mM^{-1}cm^{-1}) have a 20:1 intensity ratio,[22,27] similar to those of oxy-tyrosinase and oxy-hemocyanin,[29] and the feature near 412 nm (0.9 mM^{-1}cm^{-1}) is assigned tentatively to a pyrazole/pyridine $\pi^*\rightarrow d_{xy}$ charge-transfer transition, based on a natural transition orbital analysis of a TD-DFT calculated spectrum (TD-DFT = time-dependent density functional theory; Figure 1 B).[22,30] The DFT-optimized structure of **1** predicts a planar Cu_2O_2 core with a Cu–Cu separation of 3.57 Å, in line with the 3.51 Å distance determined by Cu K-edge extended X-ray absorption fine structure models (Table S2 and Figure S5 in the Supporting Information).[27,28] Taken together, these data fully support the structural homology between tyrosinase and **1**.

The formation of **1** is effectively quantitative (> 95 % yield) in a variety of solvents at −78 °C, as assessed by iodometric titrations of the released peroxide after treatment with trifluoroacetic acid.[22,31] The complex is stable for weeks in CH_2Cl_2 at −78 °C, yet decays within 1 day in tetrahydrofuran or acetone. Compound **1** reacts within 60 min with a wide variety of sodium phenolate salts (5 equiv), both electron-rich and -deficient; the side-on peroxide oxidant is efficiently consumed releasing catechol products after an acidic workup (Table 1 A). Using a 1:1 oxidant/phenolate stoichiometry, impressive catecholate yields (> 90 %) are possible at −78 °C, albeit reaction times of nearly 1 week are required. Expectedly, the mass of the *p*-methoxy-1,2-catechol product is shifted by 2 a.u. if **1** is formed with $^{18}O_2$, indicating dioxygen as the oxygen atom source.[32]

From kinetic data, the hydroxylation of phenolate to catecholate by **1** is best understood as a second-order process: first order in [**1**] and first order in [phenolate], with a pre-equilibrium binding event and a rate-limiting oxidation step, presumably C−O bond formation. An intramolecular competitive kinetic isotope effect of 1.2(2) measured at −78 °C with 2-D-4-*tert*-butylphenolate excludes rate-limiting C−H bond cleavage. The observed rate constants k_{obs} saturate with respect to added phenolate (Figure 2), consistent with an initial phenolate-binding equilibrium K_{eq}, followed by an intramolecular rate-determining oxidation step k_{ox} from a substrate–complex adduct (Table S1 in the Supporting Information),[18,32,33] as electron-deficient phenolates clearly react more slowly. A plot of ln(k_{ox}) versus σ_p^+ for a variety of phenolates gives a Hammett parameter $\rho = -0.99$ (Figure 2), consistent with the trend reported for tyrosinase ($\rho = -1.8$ to -2.2)[34,35] and in line with an electrophilic aromatic substitution mechanism.

At room temperature in CH_2Cl_2, **1** is formed quantitatively but decays irreversibly with a half-life of 30 min. However, this rare stability allows for catalytic hydroxylation of phenols to quinone products at room temperature. Only two other synthetic side-on peroxide species have greater thermal stability, but exogenous substrate reactivity has not been reported.[36,37] With 25 equiv of *p*-methoxyphenol and 50 equiv of triethylamine under 1 atm of O_2,[23,24,38] 10 equiv of quinone is formed in 1 h or 15 equiv in 24 h (Table 1 B), as assessed by the characteristic optical feature of quinone at 400 nm (Figure S1 in the Supporting Information). Slower catalytic reaction rates are observed with more electron-deficient phenols. At these higher temperatures, the oxidation of the catechol to quinone and its subsequent release is proposed to

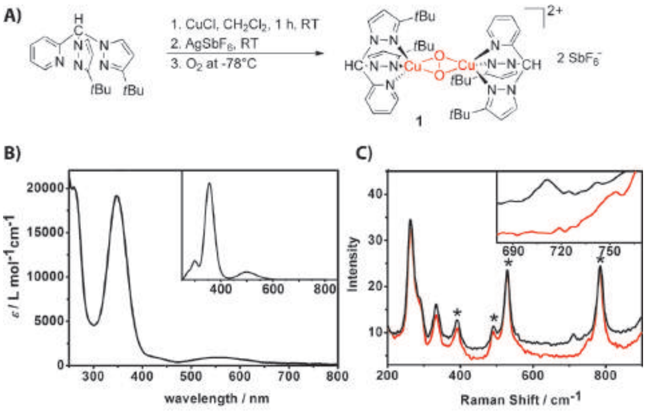

Figure 1. A) Preparation of the side-on peroxide species **1**. B) Absorption spectra of **1**; inset: TD-DFT-predicted optical spectrum of **1**. C) Resonance Raman spectra of 1 in acetone with excitation at 412 nm (red: $^{16}O_2$, black: $^{18}O_2$, asterisks (*): solvent peaks); inset: isotopic shift of the feature at 750 cm^{-1}.

Table 1: A) Reaction of phenolic substrates and **1** under N_2 atmosphere at −78 °C.[a] B) Catalytic oxidation of phenols to quinones.[b]

A)	R	X^-	Equiv[c]	Time	% catechol[d]
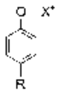	OMe	Na^+	5	5 min	>95
	Me	Na^+	5	5 min	>95
	Cl	Na^+	5	5 min	>95
	H	Na^+	5	5 min	>95
	F	Na^+	5	5 min	>95
	COOMe	Na^+	5	60 min	>95
	CN	Na^+	5	60 min	>95
	NO_2	Na^+	5	60 min	>90
	estrone	Na^+	5	5 min	>90
	8-hydroxyquinoline	Na^+	5	5 min	>90
	N-acetyltyrosine ethyl ester	Na^+	5	5 min	>90
	OMe	$HNEt_3^+$	5	10 min	>95
	Me	$HNEt_3^+$	5	10 min	>95
	OMe	Na^+	1	7 days	>90
	OMe	$HNEt_3^+$	1	10 days	>90
	estrone	Na^+	1	8 days	>90
	8-hydroxyquinoline	Na^+	1	8 days	>90
	N-acetyltyrosine ethyl ester	Na^+	1	5 days	>90

[a] All reactions performed in CH_2Cl_2 at 1 mM [Cu] and quenched with acid at -78°C after the given reaction time. [c] Equiv relative to 1. [d] Yields based on the concentrations of 1. No quinone or biphenol products were observed.

B) Substrate	Time	Turnovers[e]
p-methoxyphenol	1 h	10
N-acetyltyrosine ethyl ester	16 h	15
estrone	6 h	4
8-hydroxyquinoline	16 h	8

[b] All reactions performed in CH_2Cl_2 at 25°C under 1 atm of O_2 with 25 equiv of substrate, 50 equiv NEt_3 and [Cu] = 1.0 mM. [e] Turnover numbers based on the concentration of **1**.

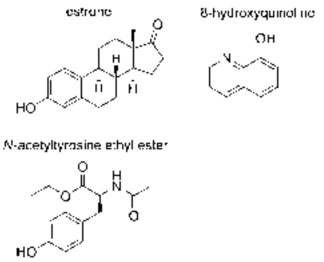

drive the reduction of the Cu^{II} centers back to a Cu^I state, permitting re-oxygenation to **1** (Scheme 1).

Three conditions appear to be necessary for catalytic turnover and support operation through a tyrosinase mechanism: ambient reaction temperatures (25 °C), proton management, and excess dioxygen. Under catalytic reaction conditions at −78 °C, rapid formation of a green species is observed, tentatively assigned as a Cu^{II} catecholate complex (Scheme 1), as one equiv of p-methoxy-1,2-catechol is formed as the sole product upon an acidic quench at this temperature. If warmed to 25 °C, this green species yields a quinone rather than a catecholate product, suggesting catecholate-binding inhibition at low temperatures (Scheme 1). Phenol deprotonation and binding to a copper center is essential in the catalytic oxidation process, as exclusion of triethylamine results in the return of unreacted phenol at −78 °C even after a reaction time of hours. After phenol deprotonation, the resultant triethylammonium cation presumably provides the necessary proton for the protonation of hydroxide to water as catecholate reduces Cu^{II} to Cu^I.

Beyond the ability to catalytically oxidize a tyrosinase substrate, N-acetyltyrosine methyl ester,[39] to its dopaquinone form, the oxidative reactivity of **1** can be extended to more complicated phenols, outside the typical substrate scope of the enzyme (Table 1 B). Estrone, an estrogenic hormone, is regioselectively *ortho*-hydroxylated to 3,4-estrone-*o*-catechol in > 90 % yield at −78 °C in less than 5 min when 5 equiv of its sodium salt are added relative to **1** (Table 1 A). The 3,4-estrone-*o*-quinone is formed under the catalytic conditions at 25 °C with 4 turnovers.[32] While mushroom tyrosinase itself

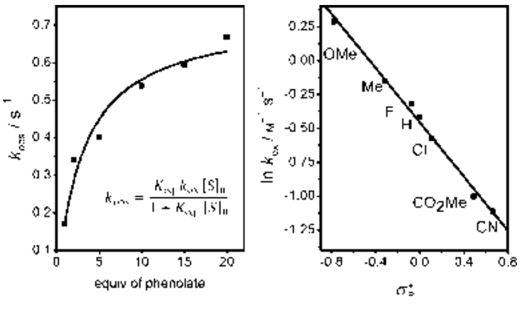

Figure 2. Reactivity of **1** at −78 °C in CH_2Cl_2. Left: Substrate-binding kinetics of the stoichiometric hydroxylation reaction with 4-fluorophenolate. Right: Hammett plot for the stoichiometric hydroxylation reaction with 1–20 equiv of various p-substituted phenolates.

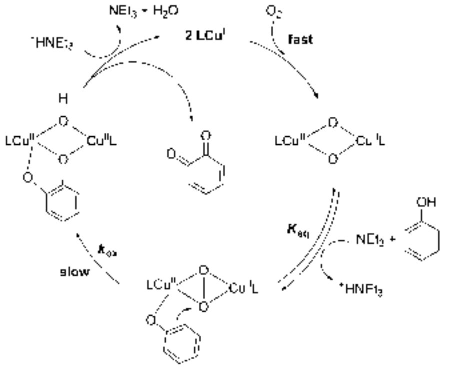

Scheme 1. Proposed catalytic mechanism of phenol oxidation by **1** in the presence of triethylamine.

can oxidize estrone,[40] 8-hydroxyquinoline is not a viable substrate,[32] possibly due to the steric demands of the fused ring structure positioned *ortho* to the phenol oxygen (Table 1 B).[26] Compound **1** oxidizes 8-hydroxyquinoline both stoichiometrically to the catechol (7,8-dihydroxyquinoline) at −78 °C, and catalytically to its quinone at 25 °C (quinoline-7,8-dione; 8 turnovers; Table 1 B), extending the substrate scope beyond that possible in the enzymatic system.[2] The substrate flexibility of **1** may thus make it a potentially useful reagent for the efficient stoichiometric conversion of a wide variety of phenolates to catechol or a catalyst for the multi-turnover oxidation of phenols by dioxygen to quinones, which are readily reduced back to catechols.[17]

Oxygen-insertion reactions that use dioxygen directly are extremely limited, despite the indisputable advantages to using Earth's ready supply of dioxygen. The difficulty lies in directing the oxidative power of dioxygen and in assuring that reactions profiles do not have insurmountable barriers or thermodynamically overstabilized intermediates. In this work, the essence of the tyrosinase enzyme mechanism, founded on the oxidizing power of dioxygen, is translated from its protein environment into a small complex through only approximate structural mimicry of the oxygenated active site, yet selective and efficient catalytic *ortho*-hydroxylation reactivity results. This strategy of copying pre-existing reactivity from Nature opens the door not only to challenging organic transformations, but for developing useful synthetic tools with substrate scopes beyond those of biological systems.

Received: February 12, 2013

Keywords: bioinorganic chemistry · copper · dioxygen · homogeneous catalysis · tyrosinase

---

[1] L. Que, Jr., W. B. Tolman, *Nature* **2008**, *455*, 333 – 340.
[2] V. Mahadevan, R. J. M. Gebbink, T. D. P. Stack, *Curr. Opin. Chem. Biol.* **2000**, *4*, 228 – 234.
[3] S. Kozuch, S. Shaik, *Acc. Chem. Res.* **2011**, *44*, 101 – 110.
[4] J. P. Collmann, *Acc. Chem. Res.* **1977**, *10*, 265 – 272.
[5] M. Momenteau, C. A. Reed, *Chem. Rev.* **1994**, *94*, 659 – 698.
[6] S. Itoh, S. Fukuzumi, *Acc. Chem. Res.* **2007**, *40*, 592 – 600.
[7] *Copper-Oxygen Chemistry* (Eds.: K. D. Karlin, S. Itoh, S. Rokita), Wiley, Hoboken, **2011**.
[8] "Metal-Oxo and Metal-Peroxo Species in Catalytic Oxidations": *Structure and Bonding* (Ed.: B. Meunier), Springer, Berlin, **2000**.
[9] L. Q. Hatcher, K. D. Karlin, *Adv. Inorg. Chem.* **2006**, *58*, 131 – 184.
[10] Y. Matoba, T. Kumagai, A. Yamamoto, H. Yoshitsu, M. Sugiyama, *J. Biol. Chem.* **2006**, *281*, 8981 – 8990.
[11] E. I. Solomon, U. M. Sundaram, T. E. Machonkin, *Chem. Rev.* **1996**, *96*, 2563 – 2605.
[12] M. Rolff, J. Schottenheim, H. Decker, F. Tuczek, *Chem. Soc. Rev.* **2011**, *40*, 4077 – 4098.
[13] C. Huang, N. Ghavtadze, B. Chattopadhyay, V. Gevorgyan, *J. Am. Chem. Soc.* **2011**, *133*, 17630 – 17633.
[14] T. V. Hansen, L. Skattebøl, *Tetrahedron Lett.* **2005**, *46*, 3357 – 3358.
[15] B. Gigante, C. Santos, A. M. Silva, M. J. M. Curto, M. S. J. Nascimento, E. Pinto, M. Pedro, F. Cerqueira, M. M. Pinto, M. P. Duarte, A. Laires, J. Rueff, J. Goncalves, M. I. Pegadod, M. L. Valdeirad, *Bioorg. Med. Chem.* **2003**, *11*, 1631 – 1638.
[16] S. Itoh, M. Ogino, S. Haranou, T. Terasaka, T. Ando, M. Komatsu, Y. Ohshiro, S. Fukuzumi, K. Kano, K. Takagi, T. Ikeda, *J. Am. Chem. Soc.* **1995**, *117*, 1485 – 1493.
[17] A. Pezzella, L. Lista, A. Napolitano, M. d'Ischia, *Tetrahedron Lett.* **2005**, *46*, 3541 – 3544.
[18] S. Itoh, H. Kumei, M. Taki, S. Nagatomo, T. Kitagawa, S. Fukuzumi, *J. Am. Chem. Soc.* **2001**, *123*, 6708 – 6709.
[19] L. Santagostini, M. Gullotti, E. Monzani, L. Casella, R. Dillinger, F. Tuczek, *Chem. Eur. J.* **2000**, *6*, 519 – 522.
[20] L. M. Mirica, M. Vance, D. Jackson Rudd, B. Hedman, K. O. Hodgson, E. I. Solomon, T. D. P. Stack, *J. Am. Chem. Soc.* **2002**, *124*, 9332 – 9333.
[21] S. Palavicini, A. Granata, E. Monzani, L. Casella, *J. Am. Chem. Soc.* **2005**, *127*, 18031 – 18036.
[22] C. Citek, C. T. Lyons, E. C. Wasinger, T. D. P. Stack, *Nat. Chem.* **2012**, *4*, 317 – 322.
[23] M. Réglier, C. Jorand, B. Waegell, *J. Chem. Soc. Chem. Commun.* **1990**, 1752 – 1755.
[24] M. Rolff, J. Schottenheim, G. Peters, F. Tuczek, *Angew. Chem.* **2010**, *122*, 6583 – 6587; *Angew. Chem. Int. Ed.* **2010**, *49*, 6438 – 6442.
[25] L. Casella, M. Gullotti, R. Radaelli, P. Di Gennaro, *J. Chem. Soc. Chem. Commun.* **1991**, 1611 – 1612.
[26] M. del Mar Garcia-Molina, F. Muñoz-Muñoz, F. Garcia-Molina, P. A. García-Ruiz, F. Garcia-Canovas, *J. Agric. Food Chem.* **2012**, *60*, 6447 – 6453.
[27] L. M. Mirica, X. Ottenwaelder, T. D. P. Stack, *Chem. Rev.* **2004**, *104*, 1013 – 1045.
[28] E. A. Lewis, W. B. Tolman, *Chem. Rev.* **2004**, *104*, 1047 – 1076.
[29] R. S. Himmelwright, N. C. Eickman, C. D. LuBien, E. I. Solomon, *J. Am. Chem. Soc.* **1980**, *102*, 5378 – 5388.
[30] R. L. Martin, *J. Chem. Phys.* **2003**, *118*, 4775 – 4777.
[31] I. Sanyal, K. D. Karlin, R. W. Strange, N. J. Blackburn, *J. Am. Chem. Soc.* **1993**, *115*, 11259 – 11270.
[32] Materials and methods are described in the Supporting Information.
[33] S. Herres-Pawlis, P. Verma, R. Haase, P. Kang, C. T. Lyons, E. C. Wasinger, U. Flörke, G. Henkel, T. D. P. Stack, *J. Am. Chem. Soc.* **2009**, *131*, 1154 – 1169.
[34] S.-I. Yamazaki, S. Itoh, *J. Am. Chem. Soc.* **2003**, *125*, 13034 – 13035.
[35] J. L. Muñoz-Muñoz, J. Berna, M. del Mar Garcia-Molina, F. Garcia-Molina, P. Antonio García-Ruiz, R. Varon, J. N. Rodriguez-Lopez, F. Garcia-Canovas, *Biochem. Biophys. Res. Commun.* **2012**, *424*, 228 – 233.
[36] Z. Hu, R. D. Williams, D. Tran, T. G. Spiro, S. M. Gorun, *J. Am. Chem. Soc.* **2000**, *122*, 3556 – 3557.
[37] M. Kodera, K. Katayama, Y. Tachi, K. Kano, S. Hirota, S. Fujinami, M. Suzuki, *J. Am. Chem. Soc.* **1999**, *121*, 11006 – 11007.
[38] J. E. Bulkowski, US patent 4545937, **1984**.
[39] V. Kahn, N. Ben-Shalom, *Pigm. Cell Res.* **1998**, *11*, 24 – 33.
[40] W. W. Westerfeld, *Biochem. J.* **1940**, *34*, 51 – 58.

Paper II

Catching an Entatic state-A Pair of Copper Complexes

Alexander Hoffmann, Stephan Binder, Anton Jesser, Roxana Haase, Ulrich Flörke, Manuel Gnida, Marco Salomone Stagni, Wolfram Meyer-Klaucke, Benjamin Lebsanft, Lara Elena Grünig, Simon Schneider, Maryam Hashemi, Arne Goos, Alina Wetzel, Michael Rübhausen, and Sonja Herres-Pawlis

Angewandte Chemie ***126****, 305–310 (2014)*

Angewandte
International Edition Chemie

Electron Transfer

DOI: 10.1002/anie.201306061

Catching an Entatic State—A Pair of Copper Complexes**

*Alexander Hoffmann, Stephan Binder, Anton Jesser, Roxana Haase, Ulrich Flörke, Manuel Gnida, Marco Salomone Stagni, Wolfram Meyer-Klaucke, Benjamin Lebsanft, Lara Elena Grünig, Simon Schneider, Maryam Hashemi, Arne Goos, Alina Wetzel, Michael Rübhausen, and Sonja Herres-Pawlis**

Dedicated to Professor Bernt Krebs on the occasion of his 75th birthday

Abstract: *The structures of two types of guanidine–quinoline copper complexes have been investigated by single-crystal X-ray crystallography, K-edge X-ray absorption spectroscopy (XAS), resonance Raman and UV/Vis spectroscopy, cyclic voltammetry, and density functional theory (DFT). Independent of the oxidation state, the two structures, which are virtually identical for solids and complexes in solution, resemble each other strongly and are connected by a reversible electron transfer at 0.33 V. By resonant excitation of the two entatic copper complexes, the transition state of the electron transfer is accessible through vibrational modes, which are coupled to metal–ligand charge transfer (MLCT) and ligand–metal charge transfer (LMCT) states.*

Copper is one of the most important redox-active metals and plays a central role in many biological processes.[1] Blue copper electron-transfer proteins are nature's workhorses for electron transfer (ET). They use copper as a one-electron relay that shuttles between the cuprous and cupric oxidation states. Their $Cu^{II/I}$ reduction potentials span a large window ($E^{\circ\prime} = 0.18$ to > 1 V versus NHE (normal hydrogen electrode)),[2] which tailors these proteins to interact with a wide variety of ET partners. The inner coordination sphere most directly affects the redox properties of metal ions.[3] Hence, tuning the $Cu^{II/I}$ redox couple is central for electron transfer in nature and also important in synthetic complexes for catalytic applications.[4–6] There are multiple factors governing the redox potential, including the effects of the first coordination sphere such as geometric constraints enforced by the ligand sphere (tetrahedral versus square-planar coordination) and ligand donor atoms (σ- and/or π-donation), as well as second-coordination-sphere effects.[7–11]

Already in 1968, Vallee and Williams coined the term "entatic state" (also called rack-induced state), defined as a "catalytically poised state intrinsic to the active site".[12] This term has been intensively discussed during the last decades.[7,13–15] Rorabacher et al. specified it to be an electronic entatic state rather than a simple geometric constraint physically imposed upon the active site by the protein matrix.[16] Hodgson et al. proved with X-ray absorption spectroscopy (XAS) methods that the concept of a rack-induced state might be not valid as the protein imposes almost no strain on the copper coordination.[17] Theoretically, it was proven that Cu^{II} prefers square-planar and square-pyramidal coordination but that π-donor ligands lead to stabilization of trigonal distorted geometries.[18] Recently, Vila et al. found that the entatic state does not require the ligand to have a preformed metal-binding site. They identified metal binding as a major contributor to the conformational rigidity of copper centers involved in electron transfer which reconciles the seemingly contradictory requirements of a rigid center for electron transfer and an accessible, dynamic site for in vivo copper uptake.[19] In blue copper centers, the entatic state is currently regarded as a "soft entatic state",[20] whereas the whole concept has been condensed into an "energization due to a misfit between ligands and metal ions."[21]

---

[*] Dr. A. Hoffmann, A. Jesser, Prof. Dr. S. Herres-Pawlis
Ludwig-Maximilians-Universität München
Department Chemie
81377 München (Germany)
E-mail: sonja.herres-pawlis@cup.uni-muenchen.de

Dr. S. Binder, B. Lebsanft, L. E. Grünig, S. Schneider, M. Hashemi, A. Goos, A. Wetzel, Prof. Dr. M. Rübhausen
Institut für Angewandte Physik and Center for Free-Electron Laser Science, Universität Hamburg
22607 Hamburg (Germany)

Dr. R. Haase, Dr. U. Flörke, Dr. M. Gnida, Dr. W. Meyer-Klaucke
Universität Paderborn, Department Chemie
Warburger Strasse 100, 33098 Paderborn (Germany)

Dr. M. Salomone Stagni
Libera Università di Bozen-Bolzano
Faculty of Science and Technology
piazza Universitá, 1, 39100 Bozen, Bolzano (Italy)

[**] We thank the Deutsche Forschungsgemeinschaft (DFG FOR 1405), the Fonds der Chemischen Industrie (FCI for S.H.-P.), the Evonik-Stiftung (R.H.), and the Bundesministerium für Bildung und Forschung (BMBF 05K12GU1 for A.W. and MoSGrid initiative 01IG09006) for financial support, the beamline staff at the Deutsches Elektronen-Synchrotron (DESY Photon Science (Germany)) and the Diamond Light Source (UK) for assistance with XAS data collection, P. Höfer at the MPI Mülheim for square-wave voltammetric measurements, and the Paderborn Cluster for Parallel Computing (PC^2 Paderborn) and the Center for Information Services and High Performance Computing of the Technische Universität Dresden for calculation time.

Supporting information for this article (including details on materials and methods, synthetic procedures, Raman measurements, XAS spectroscopy, cyclic voltammetry, square-wave voltammetry, and DFT details on Raman assignment and excited-state calculations) is available on the WWW under http://dx.doi.org/10.1002/anie.201306061.

Here, we report a series of bis(chelate) Cu^{I} and Cu^{II} complexes in which the cationic units have very similar structures even though Cu^{I} and Cu^{II} complexes generally prefer tetrahedral and square-planar environments, respectively. Besides the structural study of single crystals in the solid state, we provide insights into the structure in the liquid phase that we obtained from XAS data of complexes in solution. A resonance Raman study of Cu^{I} and Cu^{II} complexes in solution indicates that both complex types come into resonance at a similar energy around 3.2–3.4 eV. We found a vibrational mode that couples vibronically the optical charge-transfer excitation with the distortion along the reaction coordinate, leading from the Cu^{I} to the Cu^{II} geometry. Therefore, we have optical access to a charge-separated state which mimics the transition state of the inner-sphere ET. In contrast to reported outer-sphere electron-transfer studies on Cu$^{II/I}$ pairs,[22] we focus on the photochemically induced charge transfer.

The reaction of tetramethylguanidinoquinoline (TMGqu)[23] with suitable copper sources yields the series of bis(chelate) Cu^{I} and Cu^{II} complexes **1**–**5**. The most remarkable feature of these complexes is their structural similarity (Figure 1, Table 1, and Figures S1–S5 in the Supporting Information). For a Cu^{I} complex, one would generally expect a structure with tetrahedral configuration as found in [Cu(tmeda)$_2$]$^{+}$ complexes (tmeda = tetramethylethylenediamine),[24] whereas Cu^{II} complexes are square-planar (e.g. [Cu(tmeda)$_2$]$^{2+}$).[25] But in the complexes **1**–**5**, the situation is completely different. The copper centers of all complexes are tetracoordinate through interactions with two chelating guanidine–quinoline ligands. The Cu–N$_{gua}$ distances in the Cu^{I} complexes **1**–**3** are 0.1 Å longer than those in Cu^{II} complexes **4** and **5**. The contraction of the Cu–N$_{qu}$ bonds during the formal oxidation is not very pronounced (0.02 Å).

The coordination geometry can be described by a τ factor indicating a square-planar arrangement for a value of 0 and an ideal tetrahedron for a value of 1.[26] In the Cu^{I} complexes, we observe a τ of roughly 0.6 indicative of a strongly distorted tetrahedron, whereas in the Cu^{II} complexes τ amounts to 0.4. The angle between the chelate planes Cu-N$_{gua}$-N$_{qu}$ gives a measure of the tetrahedral character as well: 90° correspond to an ideal tetrahedron and 0° to square-planar coordination. This angle ranges from 65.1 to 68.3° in the Cu^{I} complexes and from 42.5 to 44.6° in the Cu^{II} complexes. This clearly demonstrates that the difference between the two oxidation states results in a twist of approximately 20° between the chelate planes and a shortening of the Cu–N$_{gua}$ bond by 0.1 Å. The guanidine substituents force the ligands to avoid each

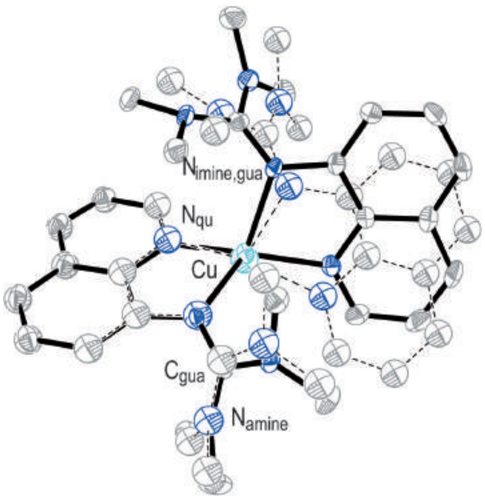

Figure 1. Superimposed molecular structures of [Cu(TMGqu)$_2$]$^{+}$ and [Cu(TMGqu)$_2$]$^{2+}$ (Cu^{I}: darker with solid bonds, Cu^{II}: lighter with dashed bonds).

Table 1: Key geometric parameters of complexes **1**–**5**.

	[Cu(TMGqu)$_2$]CF$_3$SO$_3$ **1**	[Cu(TMGqu)$_2$]PF$_6$ **2**	[Cu(TMGqu)$_2$]ClO$_4$ **3**	[Cu(TMGqu)$_2$](CF$_3$SO$_3$)$_2$ **4**	[Cu(TMGqu)$_2$](PF$_6$)$_2$ **5**
Bond lengths [Å]					
Cu–N$_{imine,gua}$	2.065(2), 2.113(3)	2.068(3), 2.095(3)	2.074(3), 2.080(3)	1.959(2), 1.964(2)	1.964(3), 1.964(3)
Cu–N$_{qu}$	1.978(3), 2.003(2)	1.966(3), 1.999(3)	1.998(3), 2.002(3)	1.976(2), 1.975(2)	1.967(3), 1.980(3)
C$_{gua}$–N$_{imine,gua}$	1.324(4), 1.321(4)	1.316(4), 1.330(4)	1.319(4), 1.312(4)	1.344(3), 1.347(3)	1.358(4), 1.347(4)
C$_{gua}$–N$_{amine,gua}$	1.356(4), 1.359(4)	1.365(5), 1.357(5)	1.362(4), 1.352(4)	1.346(3), 1.343(3)	1.324(4), 1.346(4)
	1.356(4), 1.372(4)	1.363(5), 1.355(5)	1.361(4), 1.359(4)	1.340(3), 1.341(3)	1.344(4), 1.344(4)
Bond angle [°]					
N-Cu-N	82.1(1), 81.7(1)	82.6(1), 82.1(1)	82.2(1), 81.8(1)	83.5(1), 83.7(1)	83.6(1), 83.7(1)
Structure factors					
τ_4[a]	0.60	0.58	0.60	0.40	0.41
ρ[b]	0.97, 0.96	0.96, 0.97	0.96, 0.97	1.00, 0.99	1.02, 1.00
Torsion angles [°]					
$\measuredangle$(C$_{gua}$N$_3$,CuN$_2$)	49.5, 58.6	49.1, 58.5	53.0, 59.2	47.5, 52.1	46.9, 47.2
$\measuredangle$(N$_{amine}$C$_3$,C$_{gua}$N$_3$)	30.0(av), 29.9(av)	30.1(av), 27.7(av)	30.0(av), 29.0(av)	28.3(av), 31.1(av)	30.0(av), 28.5(av)
$\measuredangle$(CuN$_2$,CuN'$_2$)	68.0	65.1	68.3	42.5	44.6

[a] $\tau_4 = \frac{360^\circ-(\alpha+\beta)}{141}$.[26] [b] $\rho = 2a/(b+c)$ with $a = d$(C$_{gua}$=N$_{imine,gua}$), b, and $c = d$(C$_{gua}$–N$_{amine}$).[27]

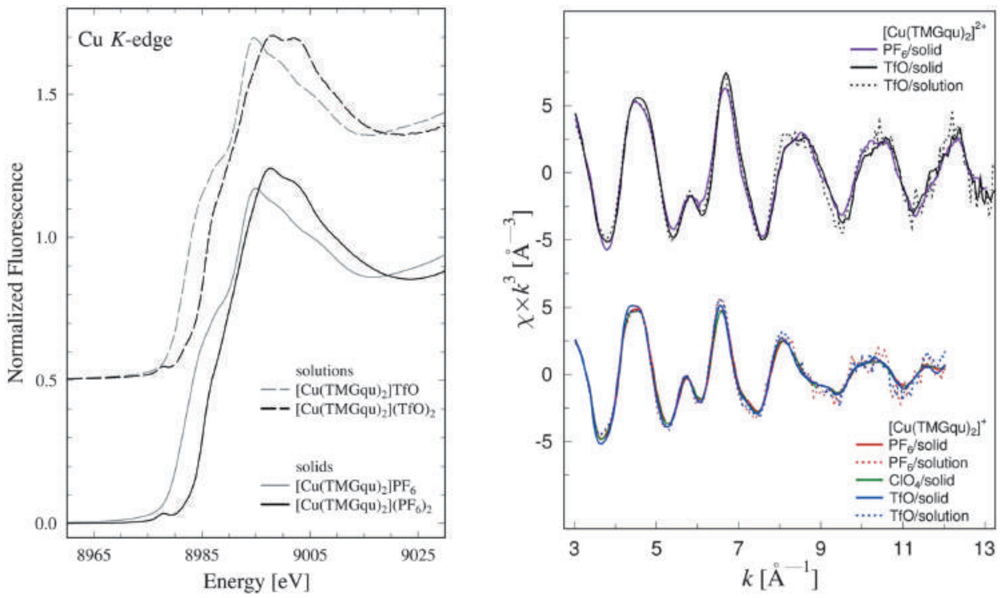

Figure 2. Left: Cu K-edge absorption of solid **2** and **5** (solid curves) as well as solutions of **1** and **4** in MeCN (broken curves). Right: Superimposed experimental k^3-weighted EXAFS spectra of various Cu^{I} and Cu^{II} complexes.

other and sterically restrain the coordination geometry to only small variations, ranging from 68 to 44° between the CuN$_2$ planes and the corresponding range of the τ value from 0.6 to 0.4.

Since the structural change between Cu^{I} and Cu^{II} is so small, we expected a reversible redox behavior. Cyclic voltammetry proves a reversible oxidation wave for **2** at 0.33 V vs. NHE (Figure S20, left) and square-wave voltammetry shows the 0.33 V oxidation to be a one-electron oxidation step (Figure S20, right).

To characterize the oxidation states we performed XAS spectroscopy on solid samples of **1**–**5** (see the Supporting Information for details). The solid curves in Figure 3 compare the Cu-K absorption edges of the complexes [Cu(TMGqu)$_2$]PF$_6$ (**2**) and [Cu(TMGqu)$_2$](PF$_6$)$_2$ (**5**). The edge positions are 8983.3 eV (**2**) and 8986.8 eV (**5**), equal to a chemical shift between the two compounds of $|\Delta E| = 3.5$ eV. The edge positions and the chemical shift identify the oxidation states as Cu^{I} in **1**–**3** and Cu^{II} in **4** and **5** (Figure S6, Table S1).[28] The oxidation state assignment is further supported by the edge shapes. Cu^{I} complexes have a characteristic shoulder or peak in the rising edge (8985 eV and below, assigned as a 1s→4p transition).[28] In contrast, Cu^{II} edges are of rather low intensity in this energy range. The intensity of the "Cu^{I} feature" can be related to the site geometry. The normalized fluorescence for **2** at 8985.6 eV is 0.65 (Figure 2), indicative of tetracoordinate Cu^{I}.[28] The Cu^{II} state in **5**, in turn, manifests itself in a very weak pre-edge peak at 8977.7 eV (Figure 2, left), assignable as a 1s→3d transition.[29] It is apparent that the edge positions, shapes, and features for Cu^{I} and Cu^{II} are the same for solid and solution samples (Figure 2). Analysis of extended X-ray absorption fine structure data (EXAFS) (Table S2, Figure 2, right) demonstrates that, for a given oxidation state, the structural models for solid and solution samples are identical within the precision of the analysis and do not depend on the choice of counterion. Raman data support the conclusion that the structure in solution is independent of the counterion (vide infra and Figure S9). EXAFS analysis of the complexes **2** and **5** confirms the molecular structures as being tetracoordinate with two nitrogen back-scatterers at 2.01 Å and two at 2.03 Å in Cu^{I} as well as two nitrogen back-scatterers at 1.95 Å and two at 2.00 Å in Cu^{II} (Table S2).

Furthermore, we performed Raman measurements on the complexes **1**, **2**, **4**, and **5** in MeCN and CH$_2$Cl$_2$ solution (Figure 3). UV/Vis measurements (see Figures S10–S17) indicated that a resonance can be expected at approximately 3.4 eV and above 4.0 eV for complexes in either oxidation states. The Raman spectra show a multitude of peaks between 400 and 850 cm^{-1}. By exciting at numerous incident photon energies, we derive the excitation dependence of the Raman peak intensities. A vibrational assignment is made possible by theoretical calculations based on extensive benchmarking.[30] Figure 4a details the excellent agreement between experimental Raman spectra taken with a nonresonant incident photon energy of 2.97 eV and calculated Raman spectra. It is noteworthy that for complex **1** 2.97 eV is clearly in off-resonance condition as the sharp resonance is close to 3.4 eV. Figure 4b compares the experimental Raman data for **4** in nearly nonresonant measurement conditions. The Raman resonance energy is shifted by about 0.3 eV (cf. Figure 3c,d),

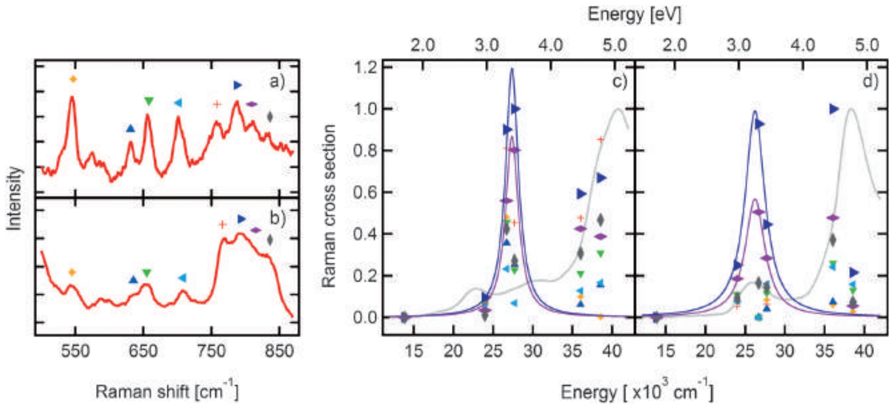

Figure 3. a) Raman spectrum of **1** in MeCN upon excitation at 2.97 eV. b) Raman spectrum of **4** in MeCN upon excitation at 4.46 eV. c) Dependence of the Raman intensity on incident photon energy for **1** in MeCN. d) Dependence of the Raman intensity on incident photon energy for **4** in MeCN. Colored symbols were used to indicate Raman peaks and their resonance behavior. The gray line denotes the absorption spectrum, whereas the colored curves serve as a guide to eye. Incident photon energies: 1.72 eV, 2.97 eV, 3.31 eV, 3.43 eV, 4.46 eV, 4.78 eV.

putting the spectrum into a preresonance explaining the difference between the calculated with the observed spectra.

We find that selected Raman peaks of both complexes turn into resonance at 3.40 and 4.45 eV (Figure 3c,d), namely the peaks at 650, 778, and 811 cm^{-1} for **1** (Cu^{I}) and at 790 and 815 cm^{-1} for **4** (Cu^{II}). Since these vibrations are resonant at similar energies for both complexes, we relate them to vibrations, which connect the crystallographically determined structures of both oxidation states within a charge-transfer process.

Tables S3 and S4 list the geometrical changes during the vibrations for **1** and **4** together with a detailed assignment. For **1**, the vibration at 800 cm^{-1} can be related to the experimental vibration at 788 cm^{-1} (purple triangle), which is a Cu–N$_{gua}$ stretching vibration with concomitant twist of the two chelate planes relative to each other. Precisely these two structural changes are the most important distortions between Cu^{I} and Cu^{II} geometry. For **4**, the peak at 815 cm^{-1} is assigned as a Cu–N$_{gua}$ stretching vibration as well. Analysis of the excited singlet states attained by resonant excitation at 3.4 eV shows that for Cu^{I} the twist angle diminishes by 7° and the Cu–N$_{gua}$ bond contracts by 0.07 Å (Figure 4c, **1^{ex}**). In the reverse sense, the excited state of the Cu^{II} complex (**4^{ex}**) displays an increase in the twist angle of 21° and a Cu–N$_{gua}$ bond elongation of 0.1 Å.

DFT analysis[30] of the optical transition at 3.4 eV of the Cu^{I} complex reveals that this is a metal-to-ligand charge transfer (MLCT, electron density difference map in Figure 4d). The corresponding transition of the copper(II) complex is a LMCT which is complementary to the MLCT of Cu^{I} (Figure 4e). Hence, we have successfully identified the vibronic mode that connects Cu^{I} and Cu^{II}.

Resonance Raman spectroscopy probes the electronic states that are most relevant for the vibrational excitation spectrum. In particular, a vibrational excitation mediating charge transfer will become resonant very close to the energy of the involved electronic charge-transfer transition that connects the involved electronic orbitals.[31,32] This resonance is expected to be much sharper and better defined in energy than UV/Vis absorptions since the resonance Raman signals are only related to one specific contribution of the charge transfer selected by the specific vibration and by doing so this technique effectively probes the reaction coordinate. Thus, the LMCT and MLCT identified by Raman spectroscopy occur in close proximity to each other as they access the inverse reaction coordinate through complementary charge-transfer processes.

In summary, we present five complexes with very similar coordination midway between tetrahedral and square-planar geometry: The oxidation of Cu^{I} to Cu^{II} increases the twist angle formed by the CuN$_2$ planes by only 20°. The two complex types are connected through a reversible electron transfer. X-ray absorption spectroscopy not only verifies the oxidation states of the reported complexes; it is also in excellent agreement with crystallographic data and demonstrates that the structures are independent of the complexes being solid or in solution. Moreover, the structures are independent of the choice of counterions which is supported by Raman spectroscopy. Hence, the coordination geometry is not a result of solid-state effects but inherent to the effects resulting from the balance between electronic and steric effects. Raman spectroscopy in solution allows access to the reaction coordinate of the electron transfer. Both complex types show resonance at an incident photon energy of 3.4 eV. DFT analysis reveals that at resonance a vibrational mode of Cu–N$_{gua}$ stretching and chelate angle torsion couples with an MLCT from Cu^{I} to Cu^{II} and an LMCT from Cu^{II} to Cu^{I}. This proves that the ET transition state is optically accessible and that the concept of ligand restrictions imposed upon copper coordination is very useful for the generation of electron-transfer models.

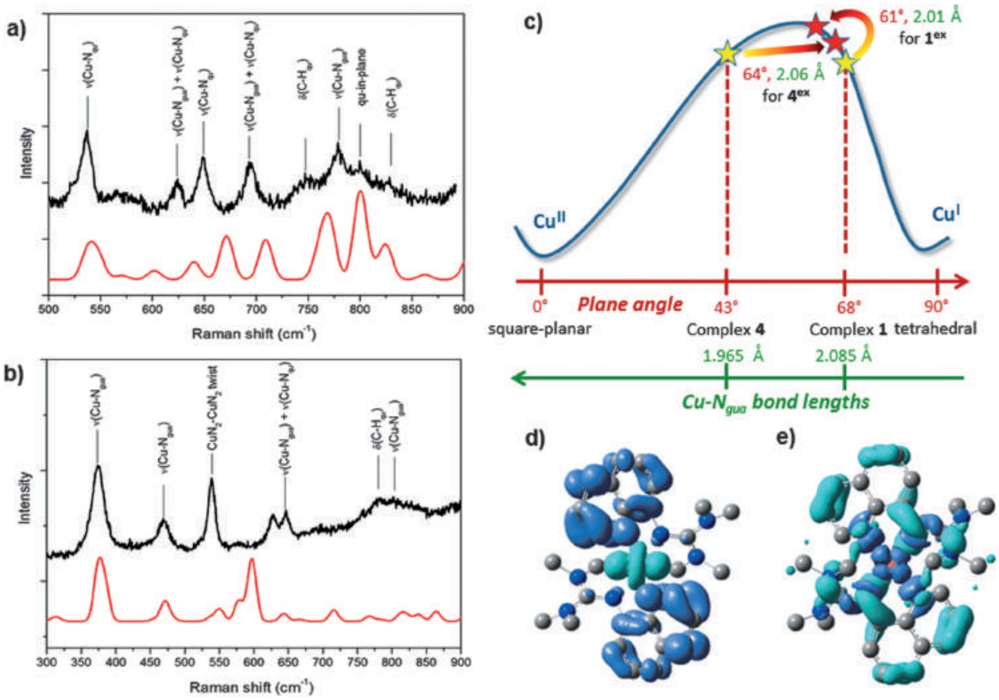

Figure 4. a) Comparison of nonresonant experimental (black) Raman spectrum at 2.97 eV and theoretical (red) Raman spectrum of **1**. b) Comparison of nonresonant experimental (black) Raman spectrum at 2.97 eV and theoretical (red) Raman spectrum of **4**. c) Reaction coordinate between $\mathrm{Cu^I}$ and $\mathrm{Cu^{II}}$ and the optically attained excited states. d) EDDM of the Cu $d_{z^2} \rightarrow \pi^*$ transition (light to dark). e) EDDM of the $\pi \rightarrow$Cu d transition (light to dark)

Received: July 12, 2013
Revised: August 25, 2013

Keywords: bioinorganic chemistry · copper · resonance Raman spectroscopy · X-ray absorption spectrocopy · X-ray diffraction

---

[1] E. I. Solomon, R. G. Hadt, *Coord. Chem. Rev.* **2011**, *255*, 774–789.
[2] S. G. Bratsch, *J. Phys. Chem. Ref. Data* **1989**, *18*, 1–21.
[3] A. B. P. Lever, *Inorg. Chem.* **1990**, *29*, 1271–1285.
[4] D. B. Rorabacher, *Chem. Rev.* **2004**, *104*, 651–697.
[5] P. Comba, M. Kerscher, *Coord. Chem. Rev.* **2009**, *253*, 564–574.
[6] H. B. Gray, B. G. Malmström, R. J. Williams, *J. Biol. Inorg. Chem.* **2000**, *5*, 551–559.
[7] K. M. Lancaster, S. DeBeer George, K. Yokoyama, J. H. Richards, H. B. Gray, *Nat. Chem.* **2009**, *1*, 711–715.
[8] K. M. Lancaster, O. Farver, S. Wherland, E. J. Crane III, J. H. Richards, I. Pecht, H. B. Gray, *J. Am. Chem. Soc.* **2011**, *133*, 4865–4873.
[9] K. M. Lancaster, M.-E. Zaballa, S. Sproules, M. Sundararajan, S. DeBeer, J. H. Richards, A. J. Vila, F. Neese, H. B. Gray, *J. Am. Chem. Soc.* **2012**, *134*, 8241–8253.
[10] J. J. Warren, K. M. Lancaster, J. H. Richards, H. B. Gray, *J. Inorg. Biochem.* **2012**, *115*, 119–126.
[11] B. E. Bursten, *J. Am. Chem. Soc.* **1982**, *104*, 1299–1304.
[12] B. L. Vallee, R. J. P. Williams, *Proc. Natl. Acad. Sci. USA* **1968**, *59*, 498–505.
[13] P. Comba, *Coord. Chem. Rev.* **1999**, *182*, 343–371.
[14] P. Comba, W. Schiek, *Coord. Chem. Rev.* **2003**, *238–239*, 21–29.
[15] P. Comba, V. Müller, R. Remenyi, *J. Inorg. Biochem.* **2004**, *98*, 896–902.
[16] G. Chaka, J. L. Sonnenberg, H. B. Schlegel, M. J. Heeg, G. Jaeger, T. J. Nelson, L. A. Ochrymowycz, D. B. Rorabacher, *J. Am. Chem. Soc.* **2007**, *129*, 5217–5227.
[17] a) P. Frank, M. Benfatto, R. K. Szilagyi, P. D'Angelo, S. Della Longa, K. O. Hodgson, *Inorg. Chem.* **2005**, *44*, 1922–1933; b) P. Frank, M. Benfatto, B. Hedman, K. O. Hodgson, *Inorg. Chem.* **2012**, *51*, 2086–2096.
[18] a) V. S. Bryantsev, M. S. Diallo, W. A. Goddard III, *J. Phys. Chem. A* **2009**, *113*, 9559–9567; b) M. H. M. Olsson, U. Ryde, B. O. Roos, K. Pierloot, *J. Biol. Inorg. Chem.* **1998**, *3*, 109–125; c) U. Ryde, M. H. M. Olsson, B. O. Roos, A. C. Borin, *Theor. Chem. Acc.* **2001**, *105*, 452–462.
[19] M.-E. Zaballa, L. A. Abriata, A. Donaire, A. J. Vila, *Proc. Natl. Acad. Sci. USA* **2012**, *109*, 9254–9259.
[20] E. Solomonet al. in *Electron Transfer Reactions*, (Ed.: S. Isied), ACS, Washington, DC, **1997**, chap. 19, pp. 317–330.
[21] P. Comba, *Coord. Chem. Rev.* **2000**, *200–202*, 217–245.
[22] a) B. Xie, T. Elder, L. J. Wilson, D. M. Stanbury, *Inorg. Chem.* **1999**, *38*, 12–19; b) P. Comba, M. Kerscher, A. Roodt, *Eur. J. Inorg. Chem.* **2004**, 4640–4645.

[23] A. Hoffmann, J. Börner, U. Flörke, S. Herres-Pawlis, *Inorg. Chim. Acta* **2009**, *362*, 1185–1193.
[24] M. Pasquali, C. Floriani, G. Venturi, A. Gaetani-Manfredotti, A. Chiesi-Villa, *J. Am. Chem. Soc.* **1982**, *104*, 4092–4099.
[25] J. T. York, E. C. Brown, W. B. Tolman, *Angew. Chem.* **2005**, *117*, 7923–7926; *Angew. Chem. Int. Ed.* **2005**, *44*, 7745–7748.
[26] L. Yang, D. R. Powell, R. P. Houser, *Dalton Trans.* **2007**, 955–964.
[27] V. Raab, K. Harms, J. Sundermeyer, B. Kovacevic, Z. B. Maksic, *J. Org. Chem.* **2003**, *68*, 8790–8797.
[28] L. Kau, D. J. Spira-Solomon, J. E. Penner-Hahn, K. O. Hodgson, E. I. Solomon, *J. Am. Chem. Soc.* **1987**, *109*, 6433–6442.
[29] J. E. Hahn, R. A. Scott, K. O. Hodgson, S. Doniach, S. R. Desjardins, E. I. Solomon, *Chem. Phys. Lett.* **1982**, *88*, 595–598.
[30] A. Jesser, M. Rohrmüller, W. G. Schmidt, S. Herres-Pawlis, *J. Comp. Chem.* **2013**, DOI: 10.1002/jcc.23449.
[31] S. Herres-Pawlis, S. Binder, A. Eich, R. Haase, B. Schulz, G. Wellenreuther, G. Henkel, M. Rübhausen, W. Meyer-Klaucke, *Chem. Eur. J.* **2009**, *15*, 8678–8682.
[32] R. G. Hadt, X. Xie, S. R. Pauleta, I. Moura, E. I. Solomon, *J. Inorg. Biochem.* **2012**, *115*, 155–162.

5.2. Time-resolved pump-probe Raman spectroscopy

In this section the time-resolved pump-probe Raman measurements on the doped manganite $La_{1-x}Ca_xMnO_3$ for the dopings x = 0.5, 0.45 and 0.24 and on the high T_c superconductor $Bi_2Sr_2CaCu_2O_{8+\delta}$ are presented. The focus of the analysis of the LCMO lies in the study of the melting and recombination process of the charge ordered phase of the commensurate doped sample by observing the temporal evolution of the Jahn-Teller mode. Because strong electron-phonon coupling is present conclusion of the electronic behaviour can be made. A comparison to the results of the non commensurate doped samples is given. The study of Bi-2212 focuses on the temporal evolution of the superconducting gap 2Δ. The closing and opening of the gap can be observed by analysing the redistribution of spectral weight in the transient Raman spectrum. For both measurements the time-resolved pump-probe Raman setup described in section 4.1 has been used.

5.2.1. LCMO

In this section a time-resolved Raman study of three $La_{1-x}Ca_xMnO_3$ samples with different dopings (x = 0.5, 0.55, 0.76) is presented. The focus of the analysis is on the commensurate doped sample and in detail the temporal evolution of the Raman-spectra. Steady state resonate Raman studies have been performed on the samples by Naler *et al.* [89, 41]. From Raman studies on $LaMnO_3$ the resonance of the Jahn-Teller mode is known to be at 1.9 eV, which is close to the used probe energy of 1.72 eV and yields a strong intensity of the studied mode [90]. Furthermore the energy of the pump beam had an energy of 3.44 eV, which is in the energy range of charge transfer transitions from the $3d$ band to the $2p$ band for manganites [91]. The FWHM of the probe beam was 1.1 ps, the pump beam had also FWHM of 1.1 ps. The power of the probe beam was chosen to 16 mW, the pump beam had a power of 14 mW. It is important to note that the spotsize of the probe beam (45 μm in diameter) was 1.5 times lager than the one of the pump beam (30 μm in diameter), which means that always unpumped regions of the sample were probed. The samples used in this study were produced at Rutgers University in New Jersey in the group of S.-W. Cheong. The 50 % and the 55 % doped sample were polycrystalline while the 76 % doped sample was a single crystal. The study was done at 50 K. All three of the samples feature an antiferromagnetic insulator at these temperature (see Figure 3.5).

Figure 5.4 shows transient time-resolved pump probe Raman spectra of the 50 % doped sample at room temperature (red) and at 50 K (blue) at a fixed delay of 33 ps.

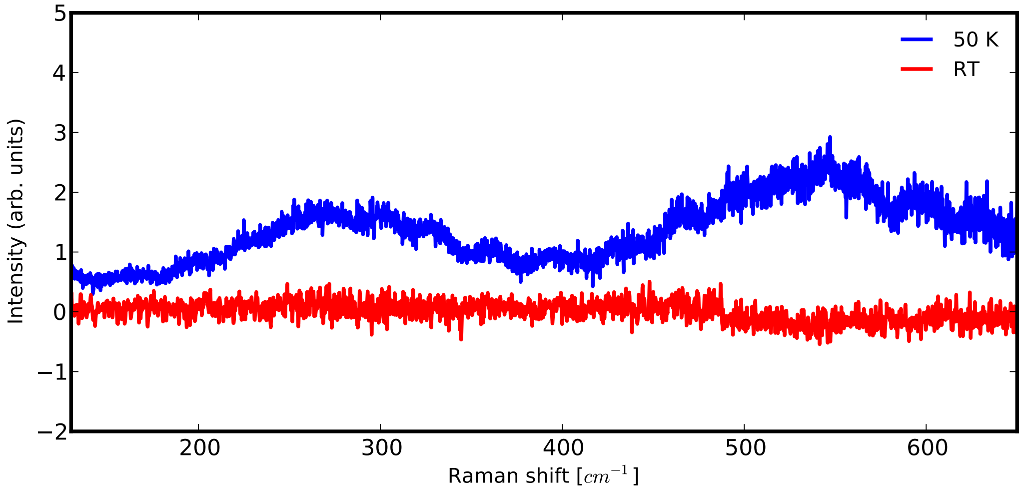

Figure 5.4.: Raman difference spectra at 33 ps delay at room temperature (red) and 50 K (blue).

The transient Raman spectra have been calculated according to equation 4.6. The suppression of two B_{2g} Jahn-Teller at 260 cm^{-1} and 540 cm^{-1} can be observed at 50 K, while no suppression is found at room temperature. A higher spectrum indicates a stronger suppression. At room temperature the sample stays in a paramagnetic state, no temporal evolution can be observed at all. At 50 K the suppression of the Jahn-Teller modes can be explained by two different processes. First the pump beam can induce a charge transfer process from Mn^{3+} to O^{2-} Ions which leads to a reduction of Jahn-Teller active Mn^{3+} Ions. The second process is a local heating of the sample due to the pump beams energy above the charge order temperature. The system enters a non equilibrium state. The further analysis will focus on the temporal evolution of the 540 cm^{-1} mode at 50 K in a temporal range from 0 ps to 500 ps. In figure 5.5 four time-resolved pump-probe Raman spectra of the 50 % doped sample are exemplary shown at different temporal delays. The left panel of figure 5.5 always shows only the probe spectra (red), the pump spectra (blue) and the combined pump and probe spectra (black). On the right panel a transient Raman spectra is shown. The transient spectra clearly displays an imitate decrease of the Jahn-Teller mode at 0 ps. The suppression gets stronger at 66 ps and 264 ps while at 462 ps the supression of the Jahn-Teller mode is almost not existent anymore. However, the transient spectra also indicates not only a change in the phononic Jahn-Teller mode but also a change in the electronic background. The wiggly nature of spectra are due to a artifact produced by the used laser and has been observed in this energy range on several different other samples. Fourie analysis of the spectra indicates that the period of the wiggles is in the range of the pulse width of the fundamental of the used laser system as well.

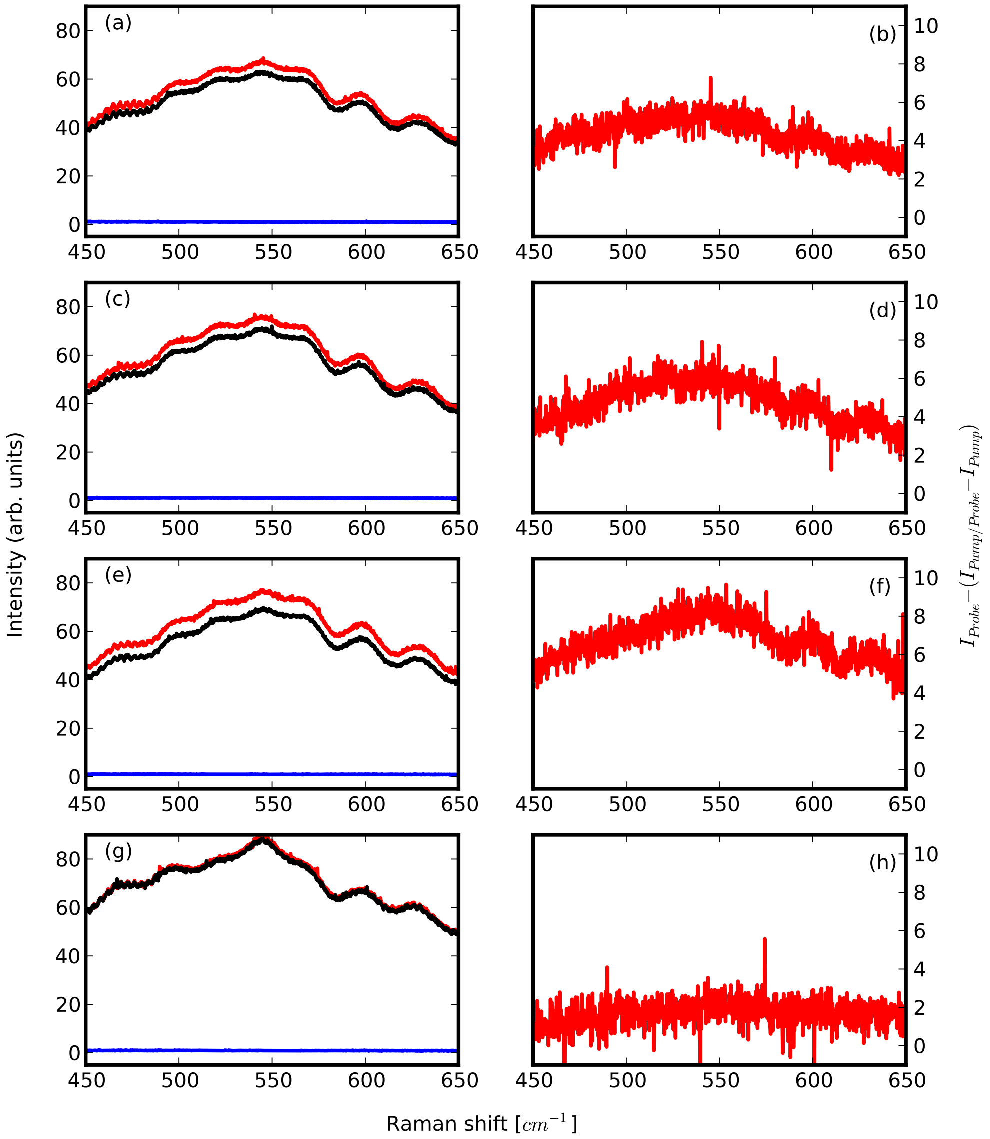

Figure 5.5.: Temporal evolution of the LCMO Raman spectra at different delays. (a) Raman spectra of LCMO 0 ps delay. Red is a probe only spectra, blue a pump only spectra and black is the pump and probe spectra. (b) Transient Raman spectra at 0 ps delay.(c)+(d)at 66ps, (e)+(f) at 264 ps and (g)+(h) at 462 ps delay respectively .

Because of these artifacts a numerical analysis of the data turned out to be difficult and several approaches have been performed to consistently analyse the data. Fig-

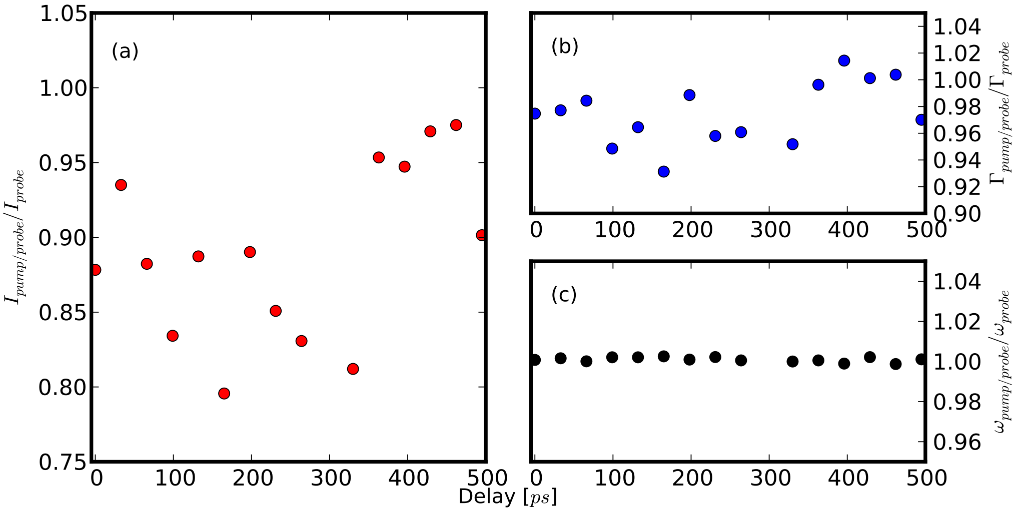

Figure 5.6.: Parameters of the numerical fit of the 50 % doped sample. (a) Intensity of the pump/probe spectra divided by the intensity of the probe spectra, (b) width and (c) position respectively.

ure 5.6 shows the results of an analysis of the pump and the pump/probe spectra minus the probe spectra. The spectra have been modeled with a Lorentzian profile according to equation 2.17. In subfigure (a) the intensity of the pump probe spectra relative to the probe spectra is depicted. A maximal decrease of the mode of up to 20 % at 165 ps was found but however, not a clear trend of the temporal evolution of the intensity of the 540 cm^{-1} can be observed, despite a decrease in the suppression of the Jahn-Teller mode after 330 ps. Panel (b) depicts the temporal evolution of the width of the Jahn-Teller mode. The width changes significantly in a range from -7 % up to +2 %. However, because the system is in a non equilibrium state these width changes can not directly related to a change of the lifetime of the Jahn-Teller excitation. Contrary to the width and the intensity of the mode, the position of the mode is constant as seen in panel (c). This indicates that the force constants are not changing in a significant way and therefore no complete structural phase transition of the sample occurs. However, these first fits did not took into account the changing electronic backgrounds.

However, the changing electronic background suggest a strong interplay between electronic and phononic degrees of freedom. To learn more about the changing of the electronic background another numerical analysis has been performed. Figure 5.7 displays the results of a Lorentzian fit of the non normalised difference spectra. In panel (a) the width of the difference spectra is displayed, the sinusoidal modulation has a period of ≈ 113 ps and is increasing in strength over time. In panel (b) the fluctuation of the electronic background is displayed. It also inherits a sinusoidal behaviour with a slightly faster period of ≈ 93 ps up to 264 ps. Afterwards

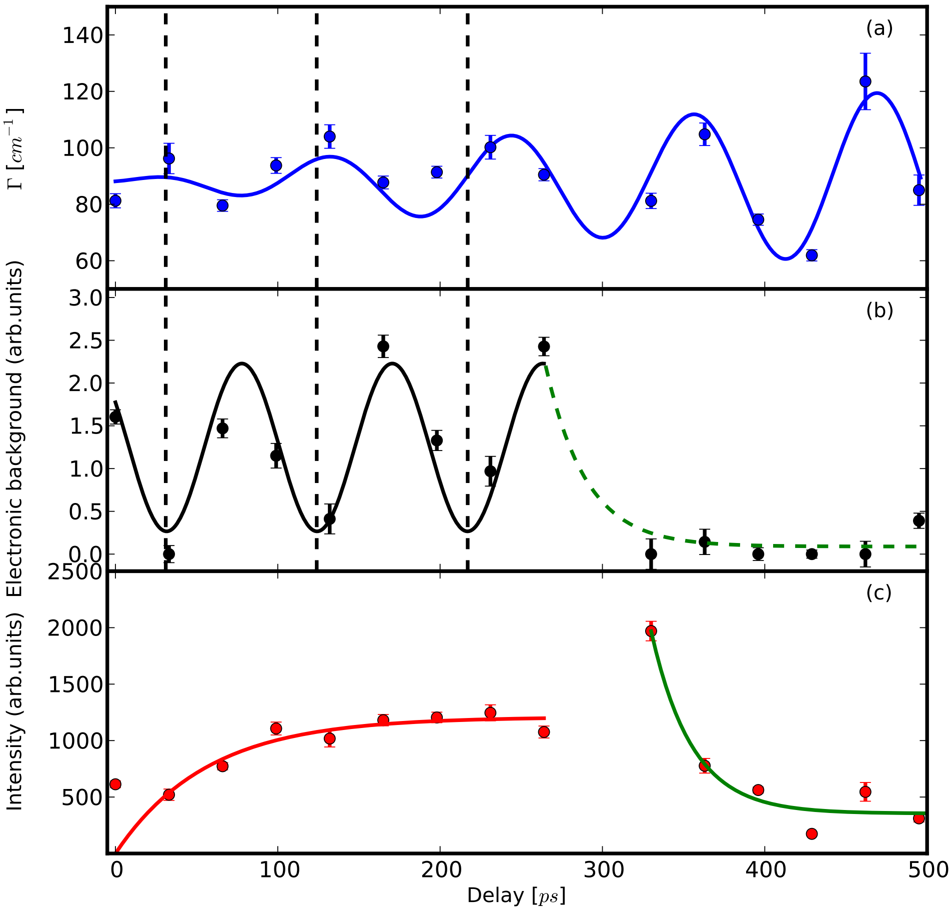

Figure 5.7.: Fitting results of the non normalised transient Jahn-Teller Raman spectra.(a) Width of the mode, (b) electronic background and (c) intensity. The width is oscillating with a period of 113 ps, the electronic background is oscillating with a period of 93 ps nearly out of phase to the width, which is indicated by the dashed black lines. At around 300 ps the electronic background vanishes. This is also the time the suppression of the intensity of the Jahn-Teller mode is beginning to decrease, after a rise up to 264 ps.

the electronic background vanishes, which is indicated by the dashed green line. It is important to note, that the width and the electronic background oscillate nearly out of phase. In panel (c) the intensity of the phonon mode is shown. Up to 264 ps a rise in the suppression of the mode can be observed with a rise time of 56 ps (red line). After 300 ps the intensity of the mode decays fast to almost no suppression which corresponds to vanishing electronic background. The green line represents an exponential fit with a resulting decay time of 25 ps.

To explain the observed behaviour the special structure of the 50 % doped sample has to be considered. The half doped sample shows a very long range charge ordered state with alternating Mn^{3+} and Mn^{4+} ions in a striped structure [37]. The Mn^{4+} ions are ordered antiferromagneticaly perpendicular to the stripe direction, while the Mn^{3+} ions are ferromagneticaly ordered parallel to the striped pattern. The Mn^{3+} stripes are Jahn-Teller distorted leading to the observed Jahn-Teller Raman mode, while the Mn^{4+} are not Jahn-Teller distorted and therefore not Raman active. After the initial pump laser pulse this ordered state gets molten leading to free charges in the system. While the quasi free electrons are moving through the crystal which leads to the formation of a polaron [92, 28]. Polarons in manganites are well known and studied [93, 94, 95]. When an electron leaves a Mn^{3+} ion via double exchange to a Mn^{4+}, a delayed response of the vanishing (Mn^{3+*}) or staring (Mn^{4+*}) Jahn-Teller distortion occurs. Because of this delayed response the charge has the tendency to move back to the energetically favorable state. By the time the charge gets back, the Jahn-Teller distortion has vanished and it is favorable for the electron to move again. This leads to a back and fourth hopping between undistorted and distorted sites which results in an increase of the radius of the polaron. The polaronic lattice distortion can be related to the change in width observed in figure 5.7 (a), the change of the electronic background in (b) describes if the charges are free (high electronic background) or temporally bound to a Mn ion (no electronic background). This also explains the out of phase oscillation of width and electronic background. If the electrons are moving most of the pump energy is localised in the kinetic energy of the electrons, while when the electrons are localised the energy is for the most part in the polaronic lattice distortion. The overall decrease in intensity (c) indicates the decrease of pure Jahn-Teller distorted sites. After 300 ps the energy of the pump beam is dissipated in the system and the electrons have not enough energy anymore to move quasi-free through the crystal and localise in the energetically favorable striped state. This explains the decay of the transient Raman intensity and the vanishing electronic background. However, the slower polaronic lattice distortion takes a longer time to completely relay into the ground state. A possible model of such a behaviour can be found by a predator-prey model [96]. Such a model describes the interplay

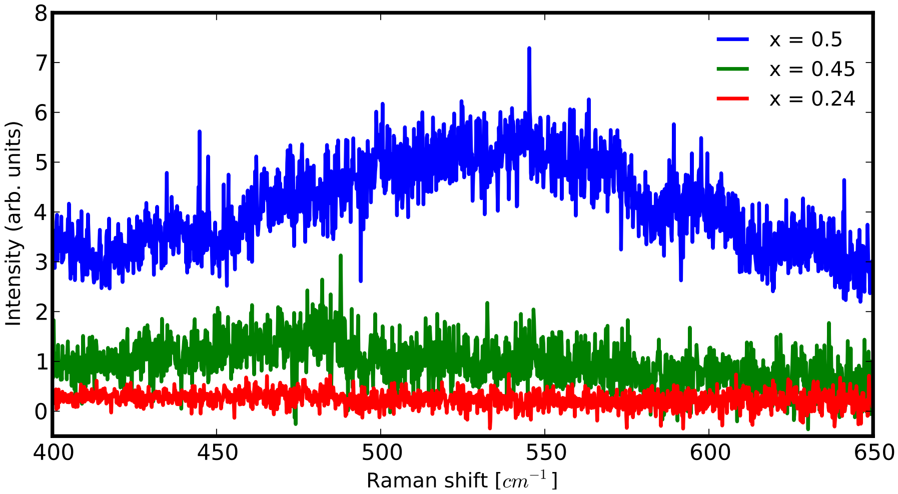

Figure 5.8.: Doping dependence of the transient Raman signal of $La_{1-x}Ca_xMnO_3$ with x = 0.5 (blue), x = 0.45 (green) and x = 0.24 (red) at a delay of 0 ps. While the 50 % doped sample exhibits a strong transient signal, at 55 % the signal is very weak and completely gone at the 76 % doped sample.

between two competing species or effects which strongly interact with each other and has been applied to a wide range of phenomena like biology or economics [97, 98, 99]. Such a model can be described mathematically by a pair of first order differential equation as follows:

$$\begin{aligned} \frac{dN_e(t)}{dt} &= \alpha N_e(t) - \beta N_e(t) N_p(t) \\ \frac{dN_p(t)}{dt} &= -\gamma N_p(t) + \delta N_e(t) N_p(t). \end{aligned} \tag{5.1}$$

Here N_e represents the number of free charges, N_p the number of lattice distortions, α the growth rate of free charges, which is related to the pump laser pulse, β the rate at which free charges are trapped by a lattice distortion, γ the decay rate of the lattice distortions and δ the rate new polarons are created by free charges. A solution to equations 5.1 leads to the phase shifted oscillating behaviour observed in the experiment.

The above given explanation of the melting and recombination process of the 50 % doped sample is backed by the results obtained for the 55 % and 76 % doped samples. Figure 5.8 displays the transient Raman spectra at a delay of 0 ps at 50 K of the three different doping examined in this study. It is clear to see that at the 76 % doped sample no transient Raman signal could be measured. Also up to 231 ps delay no transient Raman signal was observed. Possible explanations for this results are the absence of an effect at all, the effect happens on a timescale faster than the temporal resolution of the experimental setup or because of the very small percentage of Mn^{3+} within the sample, the effect is to weak to be observed. The 55 % doped sample exhibits a decrease in the Jahn-Teller mode, but compared to the 50 % doped sample the effect is roughly six times weaker. This weak signal makes a consistent numerical analysis of the temporal evolution impossible. Qualitatively the process of melting charge ordered domains and the recombination is way faster than in the 50 % doped sample. The whole process is finished after 60 ps. The 55 % doped sample exhibits no long range charge order but has charged ordered domains. However, the imbalance between Mn^{3+} and Mn^{4+} leads to an imbalance between free charges and polarons. It is more likely that a free charge is trapped by an Mn^{4+} ion with a local surrounding of other Mn^{4+} ions and therefore no possibility to enter an energetically favorable state by moving further through the crystal. In terms of the predator-prey model this can be understood that the rate at which free charge is trapped is very high compared to the rate that free charge is created.

In conclusion the time-resolved pump-probe Raman measurements on doped $La_{1-x}Ca_xMnO_3$ show a strong interplay between charge and lattice degrees of freedom for the commensurate doped sample. A decrease in the Jahn-Teller mode has been observed in a temporal range up to 500 ps. Further analysis of the data yielded a rise time of the melting process of 56 ps and after 300 ps a decay into the ground state can be found with a decay time of 25 ps. Furthermore, nearly out of phase oscillation in the width and the electronic background can be found. This is explained by the creation of free charge carriers through the initial pump pulse which creates slower polarons. Due to the striped-charge ordered nature of the 50 % doped sample a back and fourth interplay between polarons and free charge can be explained. A possible ansatz for a theoretical explanation can be found in a predator-prey model. Contrary to the 50 % doped sample the 55 % doped sample exhibits only a very weak transient Raman signal in a shorter time range and the 76 % doped sample none at all.

5.2.2. Bi-2212

Overdoped Bi-2212 has been studied extensively with steady state Raman spectroscopy in the past [63, 62]. *Budelmann et. al* observed in overdoped Bi-2212 the formation of a superconducting gap below the critical temperature T_c. The gap is a redistribution of spectral weight from the lower energy part of the electronic Raman response to the higher energy part. The rise of the so called pair-breaking peak occurs at the energy 2Δ, which is exactly the energy that is required to overcome the coupling of the electrons or in the case of Biscco-2212 the holes, which lead to the formation of Cooper pairs. It has been shown, that in overdoped Bi-2212 the pair-breaking peak consists in fact of three different contributions at 320 cm^{-1}, 440 cm^{-1} and 580 cm^{-1}, which resonate at the different excitation energies 2.5 eV, 3.3 eV and 3.8 eV in B_{1g} geometry which resembles the geometry of the superconducting order parameter Δ [100]. However, the 580 cm^{-1} peak is not related to the redistribution of spectral weight but exhibits the behaviour of a collective mode. Furthermore, the mode at 440 cm^{-1} is resonant at 3.3 eV and the 320 cm^{-1} mode resonates also at 3.3 eV as well as at 2.5 eV. This makes 3.3 eV the preferred pump energy for a pump and probe experiment, that will explicitly pump the superconducting order parameter Δ. Studies by time resolved reflectivity at $YBa_2Cu_3O_{7-\delta}$ thin film hinted at two relevant time scales in high T_c cuprate superconductors. One is a relaxation time of about 5 ps and one of > 10 ns [101]. However, only the fast component vanishes above T_c and thus is directly related to the superconducting state.

Because of this short timescales, the well characterised sample properties, the different contributions to the pair-breaking peak, which hint at more then one mechanism responsible for the formation of the superconducting state, time-resolved Raman spectroscopy is an excellent tool to study the structure of superconducting order parameter Δ directly.

For the study of Bi-2212 a slightly overdoped sample with a $T_c = 82$ K was used, which was created by P. Guptasarma and M.S. Williamsen at the University of Wisconsin, USA. The same sample was used in the study of *Budelmann et. al.* As pump energy 3.44 eV was chosen, to be close to the resonance of the 320 cm^{-1} and 440 cm^{-1} contributions of the pair breaking peak. The FWHM of the pump beam was 0.8 ps and a power of 30 mW was applied to the sample. The probe beam had an energy of 1.72 eV a FWHM of 0.9 ps and a power of 6.3 mW. It is important to note, that the probe beam is not in resonance to the gap features. Furthermore, the spot size of the pump beam was ~ 30 nm, the spot size of the probe beam ~ 45 nm, which results in a pumped unpumped sample ratio of roughly 50 %. The heating of the sample through the pump beam was estimated to $\sim 40 - 65$ K using a heat diffusion model and by comparison to continuous wave laser temperature corrected Raman spectra [102, 17]. The probe beam only heats the sample up about ~ 3 K.

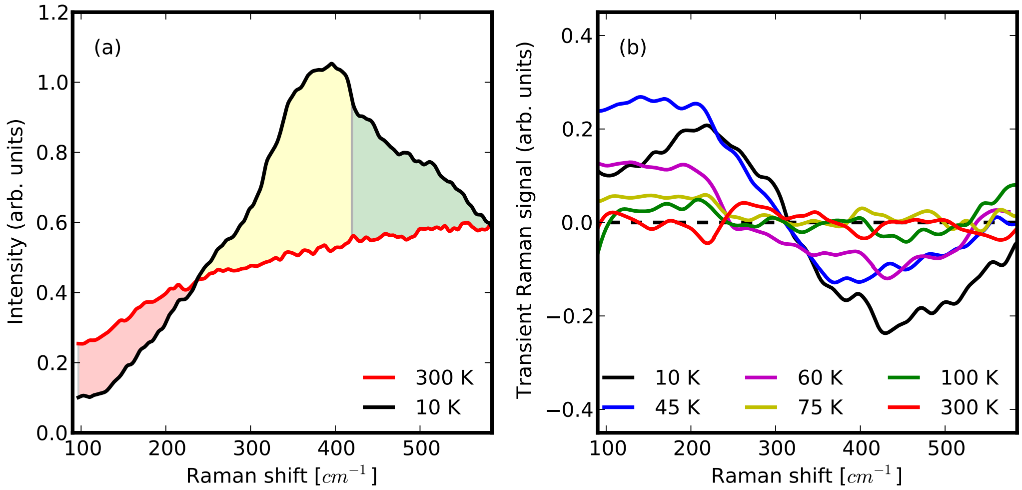

Figure 5.9.: (a) Raman spectra of Bi-2212 at 10 and 300 Kelvin in B_{1g} geometry. It is clear to see the opening of the superconducting gap below 235 cm^{-1} (red shaded area) and the formation of the pair breaking peak at 420 cm^{-1}(yellow and green area). (b) Temperature dependence of the Raman difference spectra at a fixed temporal delay of 3.3 ps in B_{1g} geometry. Above T_c the Raman difference spectra is in average zero.

In the superconducting state the heating is significant compared to T_c, while in the normal state the heating is very small compared to the Fermi temperature of about 10000 K. Therefore it is expected to only measure a non zero Raman difference spectra in the superconducting region.

Figure 5.9 (a) shows the steady state Raman spectra of Biscco-2212 at 10 K and 300 K in B_{1g} geometry. In the superconducting phase a gap is observed below 235 cm^{-1}, and a pair breaking peak arises with a maximum around 420 cm^{-1}. This translates to 2Δ of 52 meV. The red shaded area denotes the gap where spectral weight is lost and redistributed to the yellow and green shaded area. These two parts can be identified as two different contributions to the pair-breaking peak with unique timescales later in this section. In (b) the Raman difference or transient Raman spectra calculated according to equation 4.6 for different temperatures in B_{1g} geometry are shown. It is clear to see, that above 60 K the transient spectrum is zero. This is easy to understand because as discussed earlier in this chapter the heating of the sample is very small compared to the Fermi temperature T_f, so that no change in the shape of the electronic Raman response can be expected. At 60 K and below a strong change in the transient Raman signal is observed. Positive signal denotes an increase of spectral weight and negative signal a decrease of spectral weight. This is because the increase in temperature due to the heating of the probe

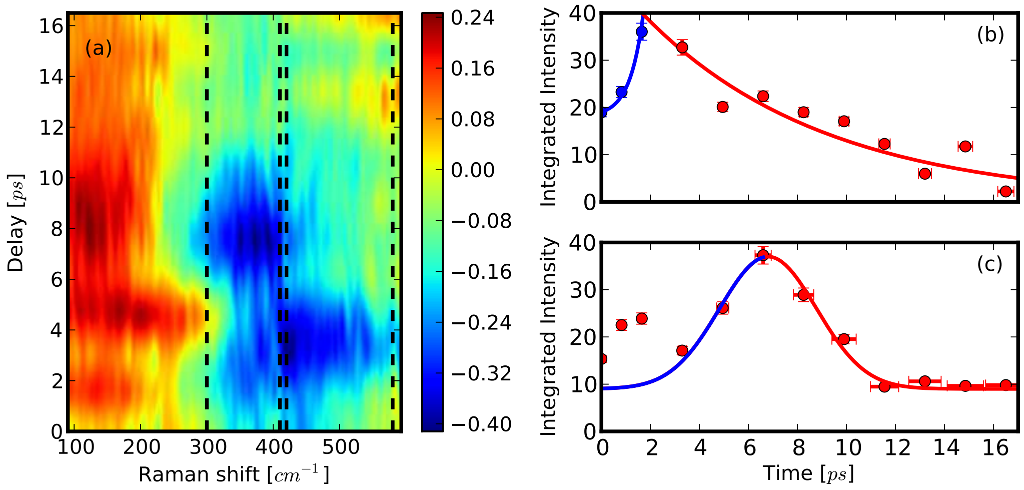

Figure 5.10.: (a) Temporal evolution of the transient Raman signal displayed in a density plot. The plot consists of twelve Raman difference spetra aquired at different temporal delays. The data has been slightly interpolated. The dashed lines mark two independent regions with different responses. (b) Integrated transient Raman intensity over time for the region between 420 cm^{-1} and 580 cm^{-1}. (c) Integrated transient Raman intensity over time for the region between 300 cm^{-1} and 410 cm^{-1}. The solid lines in (b) and (c) are the results of numerical fits.

beam is large enough to break Cooper pairs. This leads to a redistribution of spectral weight from the high energy part to the low energy part of the spectrum. This enables to study the reformation of Cooper pairs and therefore the superconducting order parameter time dependent. All the spectra in 5.9 (b) were taken at a time delay of 3.3 ps.

In Figure 5.10 (a) the temporal evolution of the transient Raman signal is displayed in a density plot. Raman shift is displayed at the x-axis, temporal delay at the y-axis. The red and blue areas correspond to a gain or loss in spectral weight. The plot consists of twelve Raman difference spectra. At first a fast decrease in spectral weight around 420 cm^{-1} can be observed after 2 ps. At 3 ps the suppression of the pair breaking peak is followed by an increase of spectral weight in the low energy region of the spectra. This refers to the light introduced breaking of Cooper pairs, which has to transform into quasiparticle excitation due to charge conservation rule. Furthermore, a second response can be observed starting at 5 ps at 370 cm^{-1}. Here also a decrease of spectral weight of the pair breaking peak and an increase at low energy region happens. However, these two responses are clearly separated in time and energy space and therefore strongly indicate two different coupling mechanisms. To further evaluate these two components, the integrated spectral weight in these two distinct regions has been summed up. The result is shown in 5.10 (b) and (c), where (b) displays the integrated intensity in an energy region of 420 cm^{-1} to 580 cm^{-1}, and (c) from 300 cm^{-1} to 410 cm^{-1}. The higher energy response exhibits a very rapid rise, with a rise time of $\tau = 1.2$ ps and a slow decay of 7.4 ps. The data could be modeled with an exponential approach. The second component has a different behaviour. The rise and decay times are equal at roughly 1.4 ps and this can be represented with a Gaussian fit. It is clear that these two components of the pair-breaking peak have different onset times and different temporal evolutions. The fast high energy response is consistent with a relaxation process through phonon-hole coupling [103]. In contrast the lower energy component can not be explained in terms of phonon-hole scattering and remains of unknown origin. However, data of the coherence peak of the spin susceptibility of neutron scattering shows for energies below 420 cm^{-1} a strong coupling between holes close to T_c [104]. These spin-mediated coupling between holes could yield an increased stiffness against an external perturbation, which results in a delayed decrease of the Cooper pairs after 5 ps. Such a delay mechanism can be supported in a picture where charge rich domains are surrounded by fluctuating charge depleted domains, resulting in the formation of a domain wall. Scanning tunneling microscope experiments indeed observed such static domains [105]. Theoretical calculation performed by *J. Unterhinninghofen and D. Manske*, which used the method of density-matrix calculations, confirmed, that the high energy response is indeed of phononic origin and resembles a phonon-hole coupling [17]. However, the delayed lower energy contribution is not introduced in the applied model.

Figure 5.11 shows the calculated transient Raman data for two different delays in B_{1g} geometry. In the insert the corresponding experimental data are displayed. The experimental data have been corrected for different spot sizes and penetration depths into the material. A good agreement between theoretical and measured data can be found. However, the theoretical decay is slower than the experimental data suggest. This leads to the assumption that multiple phonon modes mix in the decay mechanism, which would yield a faster decay. Furthermore, it is clear that differences can also result from the fact, that the model does not take hole-spin interactions into account and therefore the 5 ps delayed second response is not calculated at all.

In conclusion, it has been shown, that the temporal evolution of the superconducting order parameter Δ can be studied by the novel technique time-resolved Raman spectroscopy. Using a 1.72 eV probe and a 3.44 eV pump laser revealed, that two different timescales and thus two different mechanisms contribute to the suppression of the pair breaking peak. A full decay into the equilibrium state was observed after 17 ps, however, the first contribution started after 2 ps with a fast rise time of $\tau = 1.3$ ps and a lifetime of $\tau = 7.4$ ps. Hole-phonon coupling can explain this be-

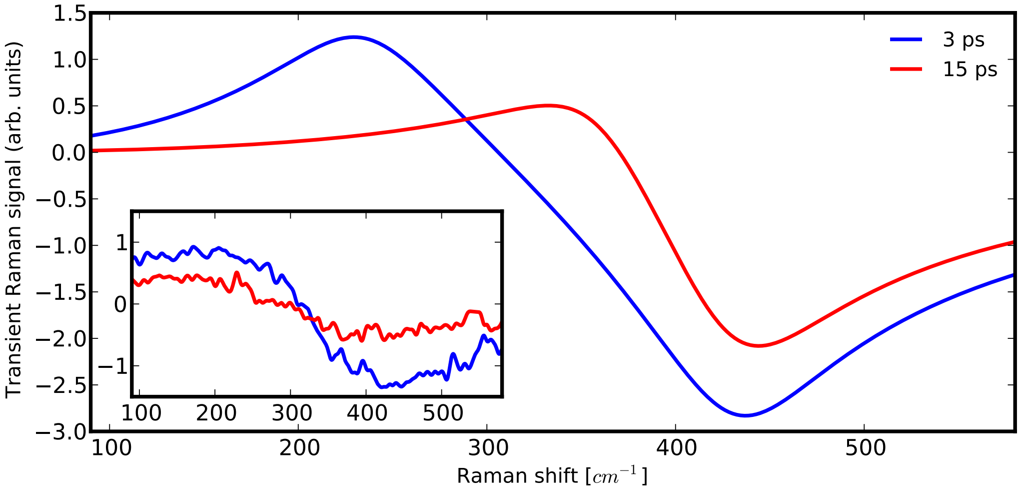

Figure 5.11.: Modeled transient Raman signal at two different delays. The insert shows the corresponding experimental data.

haviour and a good accordance to a theoretical model could be achieved. The second response started delayed after 5 ps and exhibited a symmetrical short rise and decay time of $\tau = 1.4\ ps$. This contribution can be understood if spin-hole interactions and inhomogeneous charge distribution is taken into account.

Paper III

Two-component Dynamics of the Order Parameter of High Temperature $Bi_2Sr_2CaCu_2O_{8-\delta}$ Superconductors Revealed by Time-Resolved Raman Scattering

R. P. Saichu, I. Mahns, A. Goos, S. Binder, P. May, S. G. Singer, B. Schulz, A. Rusydi, J. Unterhinninghofen, D. Manske, P. Guptasarma, M. S. Williamsen, and M. Rübhausen

Physical Review Letter ***102****, 177044 (2009)*

PRL **102,** 177004 (2009) PHYSICAL REVIEW LETTERS week ending 1 MAY 2009

Two-Component Dynamics of the Order Parameter of High Temperature $Bi_2Sr_2CaCu_2O_{8+\delta}$ Superconductors Revealed by Time-Resolved Raman Scattering

R. P. Saichu,[1] I. Mahns,[1] A. Goos,[1] S. Binder,[1] P. May,[1] S. G. Singer,[1] B. Schulz,[1] A. Rusydi,[1,2] J. Unterhinninghofen,[3]
D. Manske,[4] P. Guptasarma,[5] M. S. Williamsen,[5] and M. Rübhausen[1,*]

[1] *Institut für Angewandte Physik, Universität Hamburg, Jungiusstrasse 11, D-20355 Hamburg, Germany,*
Center for Free Electron Laser Science (CFEL), Notkestrasse 85, D-22607 Hamburg, Germany
[2] *NanoCore, Department of Physics, Faculty of Science, National University of Singapore, Singapore 117542, Singapore*
[3] *Institut für Theoretische Physik, Universität Bremen, Postfach 330440, D-28334 Bremen, Germany*
[4] *Max-Planck-Institut für Festkörperforschung, Heisenbergstrasse 1, D-70569 Stuttgart, Germany*
[5] *Department of Physics, University of Wisconsin, Milwaukee, Wisconsin 53211, USA*

(Received 2 December 2008; published 29 April 2009)

We study the dynamics of the superconducting order parameter in the high-T_c cuprate $Bi_2Sr_2CaCu_2O_{8+\delta}$ by employing a novel time-resolved pump-probe Raman experiment. We find two different coupling mechanisms that contribute equally to the pair-breaking peak. One coupling sets in very fast at 2 ps and relaxes slowly, while the other one is delayed and sets in roughly at 5 ps and relaxes fast. A model that couples holes through phonons is able to reproduce one part of the condensate dynamics; thus, we argue that hole-spin interactions are of importance as well.

DOI: 10.1103/PhysRevLett.102.177004 PACS numbers: 74.25.Gz, 74.40.+k, 74.72.Hs, 78.30.−j

The nature of the interaction between holes leading to superconductivity is encoded in the properties of the superconducting order parameter [1,2]. These properties are reflected by the energy, the momentum dependence, and the time scales on which the order parameter reacts to an external perturbation [1–4]. In a material with competing interactions, there is a potential for the development of competing ordering phenomena [2,3]. Undoped high temperature superconductors (high-T_cs) are antiferromagnetic (AFM) insulators that become superconducting upon doping. In the superconducting state, the suppressed AFM order might prevail on short length and time scales and affects thermodynamic properties [1–3]. Therefore, it is crucial to understand the transient physics that is directly connected to a specific phase transition [4]. Such an approach allows the study of competing order parameters, their individual relaxation channels and elucidates the potential interplay between them.

Major progress in the development of pulsed laser, synchrotron, and free electron laser sources has led to innovative time-resolved techniques that can directly address the transient physics of, e.g., a correlated material [5–9]. Several pump-probe techniques that have been applied to understand the superconducting condensate in high-T_cs, fail to probe the superconducting order parameter $\Delta(\mathbf{k})$ directly [5]. In this context an intense debate exists on the question of whether or not one deals with one or more coupling processes for the pairing mechanism [8]. The two mechanisms which attracted the greatest attention invoke the coupling between holes through phonons or spin fluctuations [1–3,10]. However, until today there is no clear understanding to which degree these mechanisms jointly contribute to the superconducting state. Different coupling mechanisms can be expected in different time scales in the response to an external perturbation.

In this Letter, we present a unique time-resolved two-color inelastic light (Raman) scattering experiment, which allows us to probe directly the superconducting order parameter. We report measurements of the dynamics of $\Delta(\mathbf{k})$. The samples are slightly overdoped $Bi_2Sr_2CaCu_2O_{8+\delta}$ (Bi-2212) high-T_cs with a T_c of 82 K and are very well characterized [11–14]. In our pump-probe Raman experiment we employ the UT-3 Raman spectrometer, which is a fully reflective achromatic spectrometer for the frequency range from deep ultraviolet to near infrared [15]. In order to obtain well-defined time resolution we use two pulsed laser beams. The pump beam at 3.44 eV photon energy [full width at half maximum (FWHM) is 0.8 ps] initiates the experiment and drives the system out of its equilibrium state. With the Raman probe beam at 1.72 eV photon energy (FWHM = 0.9 ps) we observe the energy and height of the pair-breaking peak $\Delta(\mathbf{k})$ as a function of delay, i.e., time difference between the pump and the probe beam. The large energy difference between the pump and the probe beam avoids any spurious signal in the Raman probe. We have employed B_{1g} polarization by using crossed polarization between incident and scattered light with respect to the a and b axes in the CuO_2 planes resembling the d-wave symmetry of the superconducting order parameter. The pump beam heats the sample roughly 40–65 K above its equilibrium temperature, whereas the probe beam heats the sample by about 3 K. These values are estimated by comparing the nonequilibrium Raman spectra to the corresponding temperature corrected equilibrium Raman spectra from a continuous wave (cw) source, and numeri-

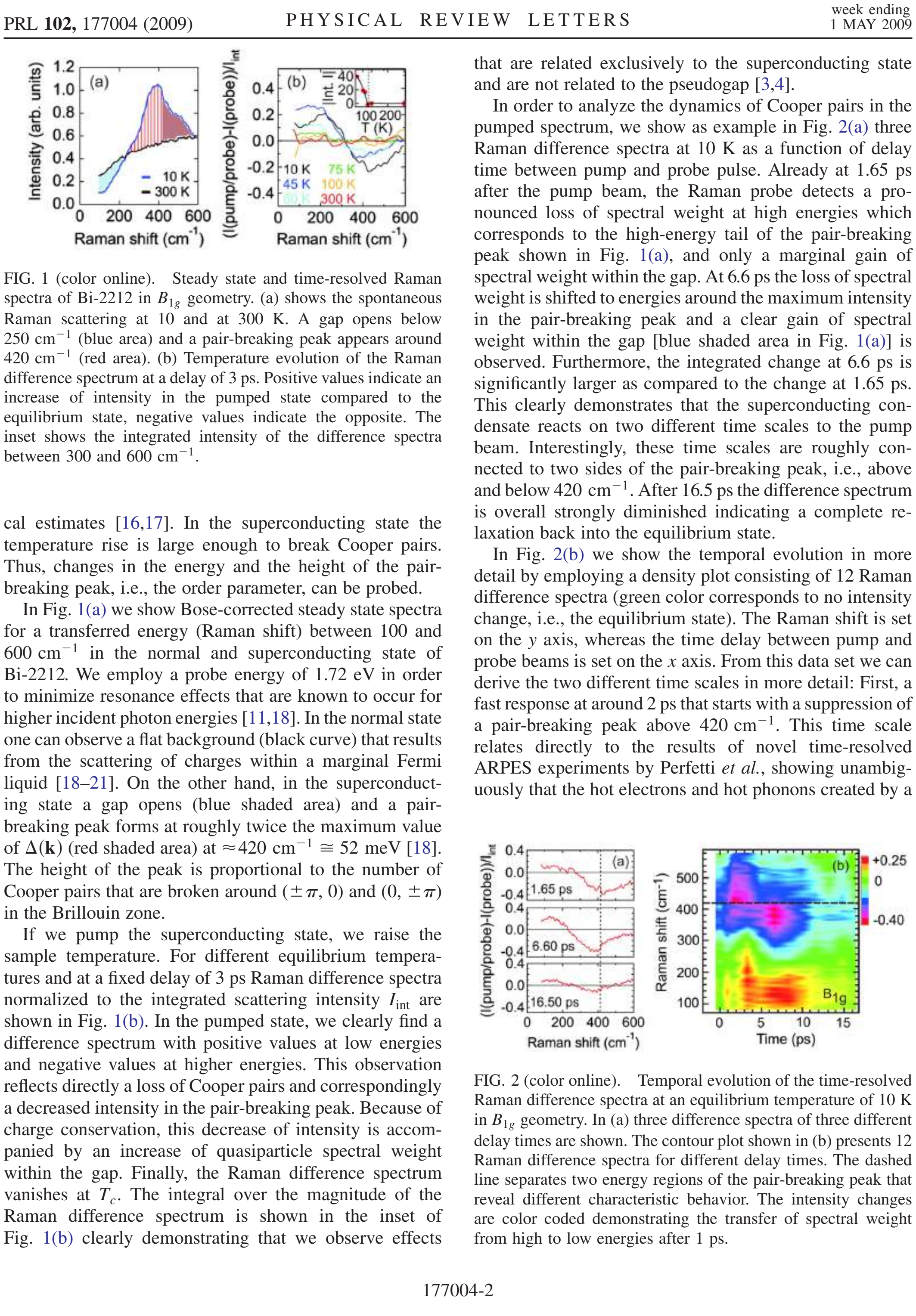

FIG. 1 (color online). Steady state and time-resolved Raman spectra of Bi-2212 in B_{1g} geometry. (a) shows the spontaneous Raman scattering at 10 and at 300 K. A gap opens below 250 cm^{-1} (blue area) and a pair-breaking peak appears around 420 cm^{-1} (red area). (b) Temperature evolution of the Raman difference spectrum at a delay of 3 ps. Positive values indicate an increase of intensity in the pumped state compared to the equilibrium state, negative values indicate the opposite. The inset shows the integrated intensity of the difference spectra between 300 and 600 cm^{-1}.

cal estimates [16,17]. In the superconducting state the temperature rise is large enough to break Cooper pairs. Thus, changes in the energy and the height of the pair-breaking peak, i.e., the order parameter, can be probed.

In Fig. 1(a) we show Bose-corrected steady state spectra for a transferred energy (Raman shift) between 100 and 600 cm^{-1} in the normal and superconducting state of Bi-2212. We employ a probe energy of 1.72 eV in order to minimize resonance effects that are known to occur for higher incident photon energies [11,18]. In the normal state one can observe a flat background (black curve) that results from the scattering of charges within a marginal Fermi liquid [18–21]. On the other hand, in the superconducting state a gap opens (blue shaded area) and a pair-breaking peak forms at roughly twice the maximum value of $\Delta(\mathbf{k})$ (red shaded area) at $\approx$420 cm^{-1} $\cong$ 52 meV [18]. The height of the peak is proportional to the number of Cooper pairs that are broken around $(\pm\pi, 0)$ and $(0, \pm\pi)$ in the Brillouin zone.

If we pump the superconducting state, we raise the sample temperature. For different equilibrium temperatures and at a fixed delay of 3 ps Raman difference spectra normalized to the integrated scattering intensity I_{int} are shown in Fig. 1(b). In the pumped state, we clearly find a difference spectrum with positive values at low energies and negative values at higher energies. This observation reflects directly a loss of Cooper pairs and correspondingly a decreased intensity in the pair-breaking peak. Because of charge conservation, this decrease of intensity is accompanied by an increase of quasiparticle spectral weight within the gap. Finally, the Raman difference spectrum vanishes at T_c. The integral over the magnitude of the Raman difference spectrum is shown in the inset of Fig. 1(b) clearly demonstrating that we observe effects that are related exclusively to the superconducting state and are not related to the pseudogap [3,4].

In order to analyze the dynamics of Cooper pairs in the pumped spectrum, we show as example in Fig. 2(a) three Raman difference spectra at 10 K as a function of delay time between pump and probe pulse. Already at 1.65 ps after the pump beam, the Raman probe detects a pronounced loss of spectral weight at high energies which corresponds to the high-energy tail of the pair-breaking peak shown in Fig. 1(a), and only a marginal gain of spectral weight within the gap. At 6.6 ps the loss of spectral weight is shifted to energies around the maximum intensity in the pair-breaking peak and a clear gain of spectral weight within the gap [blue shaded area in Fig. 1(a)] is observed. Furthermore, the integrated change at 6.6 ps is significantly larger as compared to the change at 1.65 ps. This clearly demonstrates that the superconducting condensate reacts on two different time scales to the pump beam. Interestingly, these time scales are roughly connected to two sides of the pair-breaking peak, i.e., above and below 420 cm^{-1}. After 16.5 ps the difference spectrum is overall strongly diminished indicating a complete relaxation back into the equilibrium state.

In Fig. 2(b) we show the temporal evolution in more detail by employing a density plot consisting of 12 Raman difference spectra (green color corresponds to no intensity change, i.e., the equilibrium state). The Raman shift is set on the y axis, whereas the time delay between pump and probe beams is set on the x axis. From this data set we can derive the two different time scales in more detail: First, a fast response at around 2 ps that starts with a suppression of a pair-breaking peak above 420 cm^{-1}. This time scale relates directly to the results of novel time-resolved ARPES experiments by Perfetti *et al.*, showing unambiguously that the hot electrons and hot phonons created by a

FIG. 2 (color online). Temporal evolution of the time-resolved Raman difference spectra at an equilibrium temperature of 10 K in B_{1g} geometry. In (a) three difference spectra of three different delay times are shown. The contour plot shown in (b) presents 12 Raman difference spectra for different delay times. The dashed line separates two energy regions of the pair-breaking peak that reveal different characteristic behavior. The intensity changes are color coded demonstrating the transfer of spectral weight from high to low energies after 1 ps.

pump pulse thermalize within 50 fs and 2 ps, respectively [22]. From this we can conclude that our observed dynamics after 2 ps is driven by a homogeneously heated sample. After the initial loss of spectral weight in the pair-breaking peak around 2 ps, an increase of low-energy spectral weight is observed roughly 1 ps later, reflecting the transformation of holes from the superconducting condensate into quasiparticles due to charge conservation. Then, a second, delayed response after 5 ps is observed in the pair-breaking peak, this time below 420 cm^{-1}. This spectral-weight suppression in the pair-breaking peak also yields an additional gain in spectral weight within the gap roughly after 1 ps. Thus, summarizing our spectra, we can clearly identify two contributions to the suppression of the pair-breaking peak that have their typical energy and time scales. We observe a fast onset of suppression of the pair-breaking peak above 420 cm^{-1} and a delayed suppression below 420 cm^{-1}. Both regions of the pair-breaking peak are indicated by the differently red shaded areas in Fig. 1(a). As expected from charge conservation, both responses yield their respective gain of spectral weight within the gap indicating a clear redistribution of the superconducting condensate [blue shaded area in Fig. 1(a)].

Having identified two different time scales of the superconducting condensate, what are their corresponding time (decay) constant? To study this, we have integrated the spectral weight along the energy axis above and below 420 cm^{-1} as indicated by the dashed line in Fig. 2(b). The temporal evolution of these spectral-weight changes are displayed in Fig. 3(a) and 3(b), respectively. It is remarkable that the behavior of the fast high-energy response is quite consistent with a relaxation process through in-plane phonons. Our calculation shows that this characteristic time scale of the relaxation process of about 7.4 ps is consistent with previous estimates from other experiments [5,8]. However, the second, delayed response below 420 cm^{-1} is unexpected and has also an untypical behavior, since rise and decay times are roughly equal and of only 1.4 ps [see Fig. 3(b)]. From neutron scattering experiments we know that for energies below 420 cm^{-1} the coherence peak in the spin susceptibility yields to a strong coupling between holes even close to T_c [23]. Thus, it is reasonable to assume that remnant spin-mediated coupling between holes yields an enhanced stiffness of the paired holes against an external perturbation resulting in this delayed reduction of the Cooper pairs after 5 ps. Such a scenario could be supported by a picture in which charge rich domains are surrounded by fluctuating charge poor domains. Indeed, static domains have been observed by static probes such as scanning tunneling microscopy (STM) experiments [24].

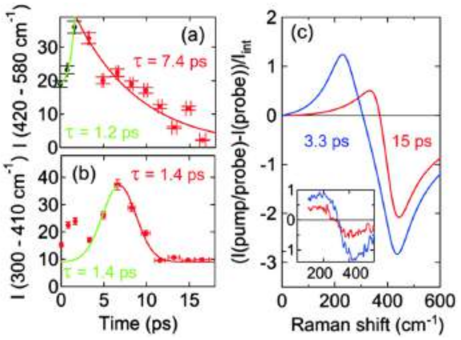

FIG. 3 (color online). Integrated intensity for the two different energy regions and comparison between theoretical and experimental response. (a) Energy region from 420 to 580 cm^{-1}. (b) Energy region from 300 to 410 cm^{-1}. The green characteristic decay time of (a) $\tau = 7.4$ ps and (b) $\tau = 1.4$ ps are determined by an exponential and Gaussian fit, respectively. (c) Calculated time-resolved Raman difference spectra for two different delay times. The inset shows the experimental difference spectra.

Finally, we show in Fig. 3(c) a comparison between a model and our Raman difference spectra in the pumped state. For our calculations, we have employed the method of density-matrix theory [25,26] which has been recently generalized for time-resolved spectroscopy on high-$T_c s$. We have used the Hamiltonian of Ref. [17] that invokes the coupling to the most important phonon modes of the CuO_2 planes, i.e., the breathing and buckling modes. The corresponding electron-phonon matrix elements are treated within LDA. Coupling of holes to spin fluctuations is not considered. Then, in the superconducting state, the non-equilibrium Raman intensity can be calculated from the imaginary part of the response function

$$\chi(\mathbf{q}=0,\omega) \sim \sum_{\mathbf{k}} \gamma_{\mathbf{k}}^2 (u_{\mathbf{k}}^2 \langle \alpha_{\mathbf{k}}^\dagger \alpha_{\mathbf{k}} \rangle + v_{\mathbf{k}}^2 (1 - \langle \beta_{\mathbf{k}}^\dagger \beta_{\mathbf{k}} \rangle) + u_{\mathbf{k}} v_{\mathbf{k}} (\langle \alpha_{\mathbf{k}}^\dagger \beta_{\mathbf{k}}^\dagger \rangle + \langle \beta_{\mathbf{k}} \alpha_{\mathbf{k}} \rangle)). \tag{1}$$

$\mathbf{q}$ and ω denote the transferred momentum and energy, respectively. The summation runs over all (electronic) wave vector $\mathbf{k}$ in the first Brillouin zone. $\gamma_{\mathbf{k}} \propto (k_x^2 - k_y^2)$ is the nonresonant B_{1g} Raman vertex. Because of the employed Bogoliubov transformation the Raman susceptibility $\chi(\mathbf{q}=0,\omega)$ includes the mixing amplitudes $u_{\mathbf{k}}$, $v_{\mathbf{k}}$ and the creation and annihilation operators $\alpha_{\mathbf{k}}$, $\alpha_{\mathbf{k}}^\dagger$, $\beta_{\mathbf{k}}$ and $\beta_{\mathbf{k}}^\dagger$ of the Bogoliubov quasiparticles (linear combination of holes and electrons), respectively [27]. The use of the low photon energies in the probe beam of about 1.7 eV makes this nonresonant vertex more applicable as compared to visible and UV-photon energies where strong resonance effects need to be considered in Bi-2212 [11]. We choose a one-band tight-binding fit to the measured band structure [18,28] and a d-wave order parameter $\Delta_{\mathbf{k}} = \Delta_0(\cos k_x - \cos k_y)/2$, yielding a quasiparticle dispersion $E_{\mathbf{k}} = \sqrt{(\epsilon_{\mathbf{k}}^2 - \mu)^2 + \Delta_{\mathbf{k}}^2}$. Then, we calculate the time-dependent expectation values $\langle\alpha^\dagger_{\mathbf{k}}\alpha_{\mathbf{k}}\rangle(t)$, $\langle\beta^\dagger_{\mathbf{k}}\beta_{\mathbf{k}}\rangle(t)$ and $\langle\beta_{\mathbf{k}}\alpha_{\mathbf{k}}\rangle(t) = \langle\alpha^\dagger_{\mathbf{k}}\beta^\dagger_{\mathbf{k}}\rangle^*(t)$ with the help of coupled Boltzmann equations for the nonequilibrium situation in the pumped state. An additional damping $\delta = 5$ meV is used to account for other scattering processes that we do not take into account. After numerical solution of the equations of motion, the results can be inserted into Eq. (1), and a pump-probe difference Raman spectrum as a function of delay time can be calculated.

Figure 3(c) shows the calculated difference Raman spectra at a fixed delay time of 3.3 and 15 ps. The inset shows the corresponding measured data that have been corrected for the ratio of the pumped to the probed volume [29]. We find a fair agreement considering that we have used no adjustable fitting parameters in the normalized plot of the Raman response. However, the relaxation in the measured Raman spectra is faster as compared to the model calculations indicating a superposition of different phonon modes that contribute to the relaxation process. The electron-phonon coupling strength for the in-plane oxygen breathing and out-of-plane buckling modes [30] yields typical time constants of 4 and 20 ps, respectively, (not shown). From this we derive a roughly 80% contribution of the breathing mode in the phonon mediated relaxation process [17,26]. Furthermore, it is obvious that the second response below 52 meV with a delayed onset after 5 ps and very fast decay time of less then 1.4 ps cannot be described within our model. As mentioned above, this strongly suggests that the hole-spin interaction and the inhomogeneous distribution of holes within the copper-oxygen plane needs to be included in any theory that aims to fully understand the time-resolved Raman response as shown in Fig. 2(b).

In conclusion, we present a unique two-color Raman experiment revealing the ultrafast dynamics of the superconducting order parameter in Bi-2212 by employing a novel time-resolved pump-probe Raman experiment. Our results demonstrate that the pair-breaking peak in the Raman responses reacts on two different time scales. These time scales are equivalent to two different coupling mechanisms. Both couplings show the redistribution of spectral weight from the pair-breaking peak to a quasiparticle response within the gap. The first, fast response sets in at 2 ps and relaxes within 7.4 ps, the second response sets in at 5 ps and relaxes within 1.4 ps, respectively [see Fig. 2(b)]. Based on density-matrix calculations, we are able to model the first response by the coupling of holes to phonons and find the in-plane breathing mode to be dominant. However, for an understanding of the second, delayed Raman response one would need to account explicitly for hole-spin interactions and for the inhomogeneous nature of the charge distribution. Our new technique provides direct information on the condensate dynamics as well as on the coupling mechanisms responsible for the formation of the superconducting state.

We acknowledge stimulating discussions with S. L. Cooper, M. V. Klein, T. P. Devereaux, J. Schneider, M. Drescher, W. Wurth, K. Scharnberg, G. Sawatzky, and A. Cavalleri. Financial support has been granted by the DFG via Ru773/3-1, GK 1286, the BMBF via the project "Time Resolved VUV Raman Scattering" and the NUS YIA.

---

*ruebhausen@physnet.uni-hamburg.de

[1] D. J. Scalapino, Phys. Rep. **250**, 329 (1995).

[2] E. Fradkin, *Field Theories of Condensed Matter Systems* (Addison-Wesley Reading, MA, 1991).

[3] V. J. Emery and S. A. Kivelson, Nature (London) **374**, 434 (1995).

[4] D. Mihailovic and V. V. Kabanov, *Structure and Bonding* (Springer, Berlin, 2005), Vol. 114, p. 331.

[5] R. A. Kaindl *et al.*, Phys. Rev. B **72**, 060510(R) (2005).

[6] G. L. Carr *et al.*, Phys. Rev. Lett. **85**, 3001 (2000).

[7] R. A. Kaindl *et al.*, Science **287**, 470 (2000).

[8] J. Demsar *et al.*, Phys. Rev. Lett. **82**, 4918 (1999).

[9] A. Cavalleri *et al.*, Phys. Rev. B **70**, 161102(R) (2004).

[10] R. Zeyher and M. L. Kulić, Phys. Rev. B **53**, 2850 (1996).

[11] D. Budelmann *et al.*, Phys. Rev. Lett. **95**, 057003 (2005).

[12] M. Rübhausen *et al.*, Phys. Rev. Lett. **82**, 5349 (1999).

[13] M. V. Klein *et al.*, J. Phys. Chem. Solids **67**, 298 (2006).

[14] M. Rübhausen *et al.*, J. Phys. Chem. Solids **67**, 312 (2006).

[15] B. Schulz *et al.*, Rev. Sci. Instrum. **76**, 073107 (2005).

[16] A. Bock, *Makro- und Mikro-Raman-Spektroskopie an* $\mathrm{YBa_2Cu_3O_7}$ *Filmen und Mikrobrücken* (Verlag Shaker, Aachen, 1993).

[17] J. Unterhinninghofen, D. Manske, and A. Knorr, Phys. Rev. B **77**, 180509 (2008).

[18] T. P. Deveraux and R. Hackl, Rev. Mod. Phys. **79**, 175 (2007).

[19] M. V. Klein and S. B. Dierker, Phys. Rev. B **29**, 4976 (1984).

[20] R. Hackl *et al.*, Phys. Rev. B **38**, 7133 (1988).

[21] C. M. Varma *et al.*, Phys. Rev. Lett. **63**, 1996 (1989).

[22] L. Perfetti *et al.*, Phys. Rev. Lett. **99**, 197001 (2007).

[23] L. Capogna *et al.*, Phys. Rev. B **75**, 060502(R) (2007).

[24] J. A. Slezak *et al.*, Proc. Natl. Acad. Sci. U.S.A. **105**, 3203 (2008).

[25] M. Kira and S. W. Koch, Prog. Quantum Electron. **30**, 155 (2006).

[26] M. Richter *et al.*, Phys. Rev. B **75**, 115331 (2007).

[27] One can recover the equilibrium Raman response from Eq. (1) by calculating the equilibrium expectation values; one finds $\langle\alpha^\dagger_{\mathbf{k}}\alpha_{\mathbf{k}}\rangle = \langle\beta^\dagger_{\mathbf{k}}\beta_{\mathbf{k}}\rangle = f(E_{\mathbf{k}})$ with the Fermi function f, $\langle\beta_{\mathbf{k}}\alpha_{\mathbf{k}}\rangle = u_{\mathbf{k}}v_{\mathbf{k}}(1 - 2f(E_{\mathbf{k}}))/(\hbar\omega + i\eta + 2E_{\mathbf{k}})$, which yields the usual Raman response.

[28] A. A. Kordyuk *et al.*, Phys. Rev. B **67**, 064504 (2003).

[29] Both volumes and their penetration depths λ are different due to the variation of the dielectric function between 1.72 eV ($\lambda = 120$ nm) and 3.44 eV ($\lambda = 50$ nm).

[30] J. Song and J. F. Annett, Phys. Rev. B **51**, 3840 (1995).

5.3. VUV-Raman specostropy

In this section an overview of the measurements at the free electron laser Hamburg (FLASH) is given. First calibration data on sand blasted silicon is presented and the general measurement conditions are discussed. Furthermore, the procedure of energy calibration of the VUV-Raman instrument is shown. In the second part the VUV-Raman data taken on doped and undoped spin-ladder compounds are presented and a full theory of the Raman matrix element is presented.

5.3.1. Silicon calibration results

Figure 5.12 shows data taken on sand blasted silicon at the energy ranges of the copper $3s$ ($122.1eV$) edge. It is expected that no resonance effects occurred for this excitation energies (see 2.1) and therefore silicone will only give an elastic response. This is true for the $Cu-3s$ edge and the elastic response is huge enough, that a numerical fit could be performed to determine the exact position on the CCD. With knowledge of the initial FLASH energies the energy axis can be calculated.

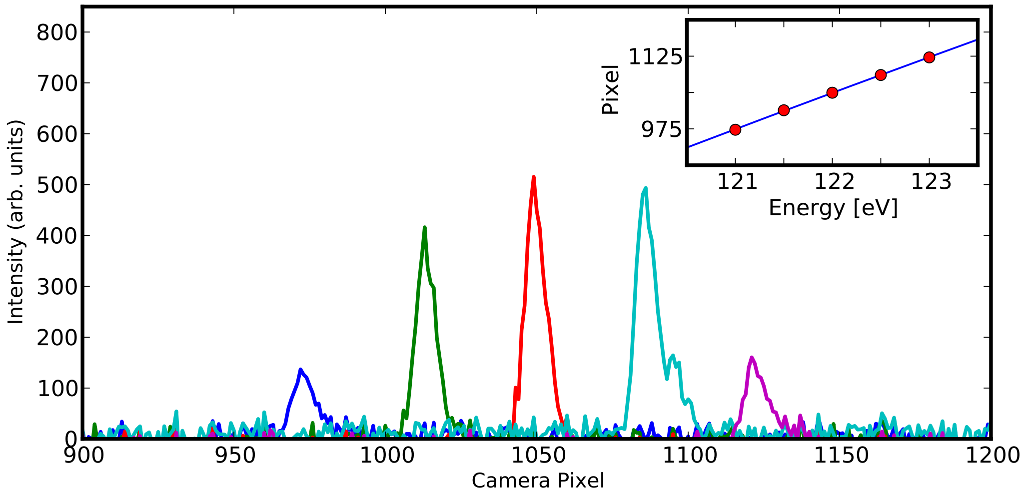

Figure 5.12.: Silicone spectra over camera pixel at different excitation energies at the copper $3s$ edge. 121 eV (blue), 121.5 eV (green), 122 eV (red), 122.5 eV (light blue), 123 eV (violet). In the inserts a linear fit of the peak positions of the elastic response is shown.

For the copper 3p-edge an identical procedure has been performed.

5.3.2. Spin-ladder compound

Spin-ladder compounds have been in the focus of scientific interest in the last decades. The key-structural components are the copper-oxygen bonds in the Cu_2O_3 ladders and the CuO_4 chains. The physics are given by the competition between kinetic energy, electron-electron interactions and superexchange energies. In a Hubbard-Model picture the kinetic energy can be determined by the hopping matrix element t, the electron-electron interactions by the Coulomb on-site repulsion U and the superexchange energy J. Here, a VUV-Raman resonance study at the intrinsically hole doped SLC SCO and the undoped LCCO is presented. The measurements were done at the VUV-Raman instrument at the Free Electron Laser Hamburg (FLASH) at the PG1 beamline. The measurements were performed at the Cu M_1 edge, which allows to investigate $Cu - 3_s \rightarrow 4_p$ band transitions and at the Cu M_3 edge to investigate $Cu - 3_p \rightarrow 3d$ transitions. The energy resolution was 24 meV. The used samples have been characterised beforehand by UV-Raman-spectroscopy finding a strong two-phonon excitation at 138 meV and a three-phonon excitation at 207 meV, which are the second and third order of a one-phonon excitation at 69 meV [65]. Furthermore, the samples have been investigated by soft x-ray scattering and x-ray absorption [58, 106]. The samples are single crystals grown by S. Uchida at the University of Tokyo [107].

To fully understand the observed features, figure 5.13 depicts the density of states of doped and undoped SLC. The copper 3d-band splits into an occupied lower Hubbard Band (LHB) and into an unoccupied upper Hubbard band (UHB). The bare electronic correlation is defined by the Coulumb on-site repulsion energy of the Cu-3d states, which is in the case of cuprates in the order of $U_{dd} \sim 10 - 12\ eV$ [108, 109]. Due to the fact, that in SLCs the O-2p band is closest to the Fermi energy and strong hybridizations occur between the Cu-3d and the O-2p orbitals, U_{dd} is modified, which leads to a normalisation to an effective LHB and UHB respectively [110]. This leads to an effective correlation energy U_{pd}. In the case of doping the doped holes have a O-2p character, which should also influence U_{pd} [58]. Because the effective LHB and UHB reside very close to the Fermi level, tuning incident photon energies to the M_3 edge gains access to these effective electronic correlation energies by studying resonance effects. A possible matrix element accessing spin excitations is discussed later in this chapter. At the Cu-M_1 edge, the Cu-4p states can be accessed, which hybridize with O-3p orbitals. This gains access to oxygen related phonoic excitations.

Figure 5.14 shows the acquired spectra for SCO polarised along the a-axis at the Cu M_3 edge (a), and Cu M_1 edge (b). The black dashed line represents the source

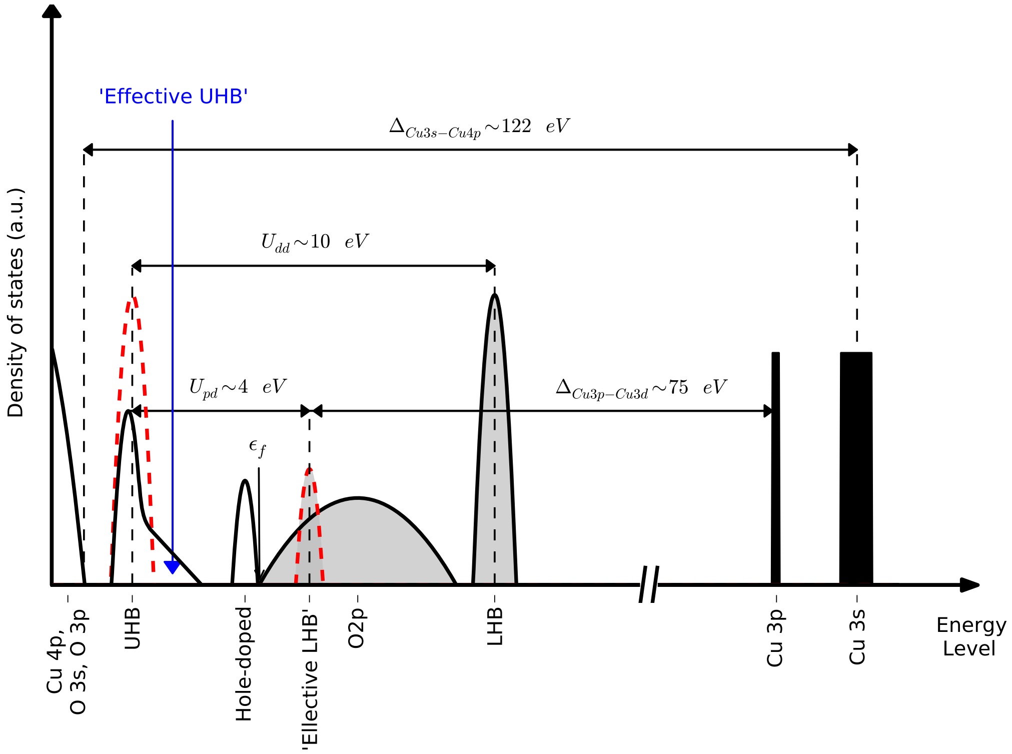

Figure 5.13.: Proposed electronic density of states for spin-ladder compounds. Note that in the doped case the doped holes are slightly above the Fermi level.

intensity, the dashed red line represents the elastic response of sand blasted silicone. A clear change in the inelastic response can be observed in the inelastic response for the Cu-M_3 edge. At the lowest excitation energy the inelastic part is sharp and broadens by increasing to higher excitation energies. At the Cu-M_1 edge an inelastic contribution can be observed at 120 meV which has its resonance at 122.5 eV. This excitation is a strong two-phonon scattering which is in good agreement with UV-Raman results. Also at higher incident photon energies a second mode below 100 meV has been observed which relates to single phonon excitation also in good agreement with UV-Raman results. In contrast to that the excitations at the Cu-M_3 edge result from spin excitations i.e. at 80 eV excitation energy two-magnon excitations can be observed. Figure 5.14 (c) shows these different contributions at the Cu-M_1 and Cu-M_3 edge.

Further investigation of the spin-flip excitations at the M_3 edge are displayed in figure 5.15. Here the VUV-Raman spectra are normalised to the source intensity and displayed over energy loss. In LCCO at the lowest excitation energy of 78 eV (blue curves) which is closest to the XAS edge, a strong excitation at 90 meV can be observed which can be identified as a one-magnon excitation at the spin-gap energy

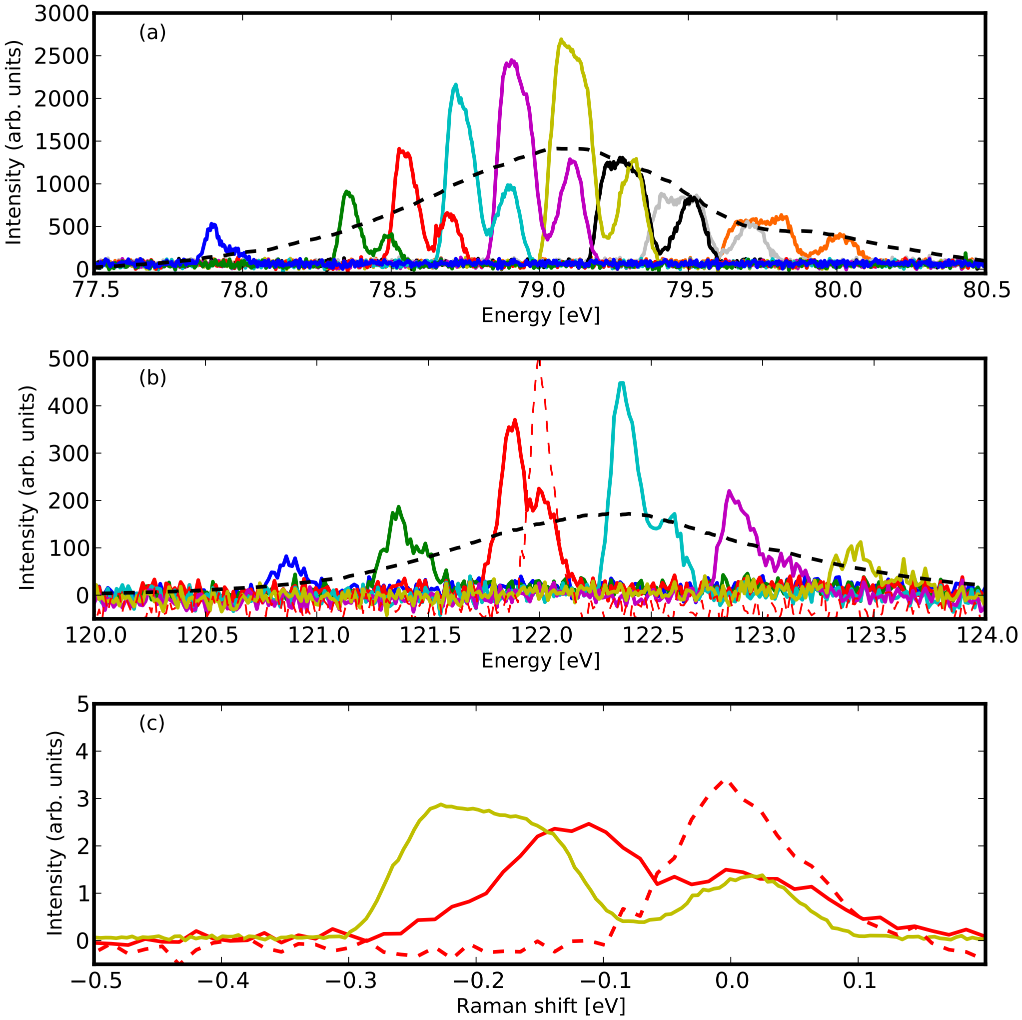

Figure 5.14.: (a) VUV-Raman spectra of SCO along the a-axis at the Cu-3p edge. The initial photon energies were 78 eV (blue), 78.5 eV(green), 78.7 eV (red), 78.9 eV (cyan), 79.1 eV (magenta), 79.3 eV (yellow), 79.5 eV (black), 79.7 eV (gray) and 80 eV (orange). The dashed black line represents the FLASH intensity. (b) VUV-Raman spectra of SCO along the a axis at the Cu-3s edge. The initial photon energies were 121 eV (blue), 121.5 eV (green), 122 eV (red), 122.5 eV (cyan), 123 eV (magenta) and 123 eV (yellow). The dashed red line is the elastic silicone response at 122 eV, the dashed black line represents the Flash intensity. (c) Comparison of the Flash intensity normalised 122 eV spectra (red) to the 79.3 eV spectra (yellow). the dashed line represents the elastic response. The response at the Cu-M_1 edge is two phonon scattering, which can also be observed in UV-Raman. In contrast to that the inelastic respone at the Cu-M_3 edge relates to spin flip excitations.

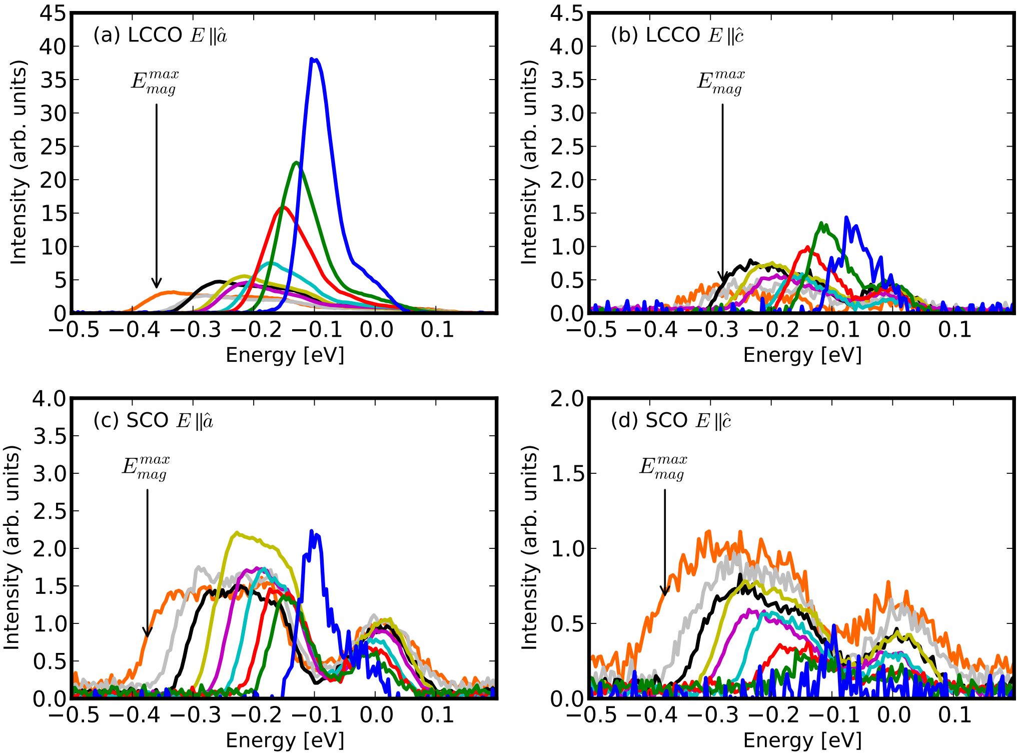

Figure 5.15.: Normalised VUV-Raman spectra of LCCO with a polarisation along the a-axis (b) and c-axis (b) and SCO along the a-axis (c) and c-axis (d). The incident photon energies are 78 eV (blue), 78.5 eV (green), 78.7 eV (red), 78.9 eV (cyan), 79.1 eV (magenta), 79.3 eV (yellow), 79.5 eV (black), 79.7 eV (gray) and 80 eV (orange).

with momentum transfer $q \approx 0$ (see figure 5.15 (a) and (b)) [111, 112]. This excitation exhibits a strong anisotropy, it is 25 times stronger for polarisation along the a-axis in LCCO which means that magnetic bonds are broken along the $\hat{c}$ direction along the legs of the ladder. This allows the propagation of long distances which resembles small q. For polarisation along the c-axis this is not possible. At higher excitation energies also a two-magnon peak can be observed, which resonates at 79.3 eV (yellow curve). The maximal magnon energies of $E_{mag}^{max} \approx 360\ meV$ can be observed at 80 eV excitation energy for polarisation along the a-axis (see figure 5.15 (a)). For polarisation along the c-axis $E_{mag}^{max} = 280 \pm 10\ meV$ can be observed which reveals an anisotropy of $\Delta E_{mag} = 80 \pm 10\ eV$. In contrast to this for SCO reveals no anisotropy at all with $E_{mag}^{max} \approx 375\ meV$, and $\Delta E_{mag} = 5 \pm 10\ eV$. Furthermore, the one-magnon magnetic excitation is strongly suppressed by a factor of 20. Also lower energy contributions to the two-magnon peak arise in SCO at 80 eV excitation energy.

To understand this striking behaviour a model has been developed. Based on the Fleury-Loudon Hamiltonian a two-magnon excitation which involves electron trans-

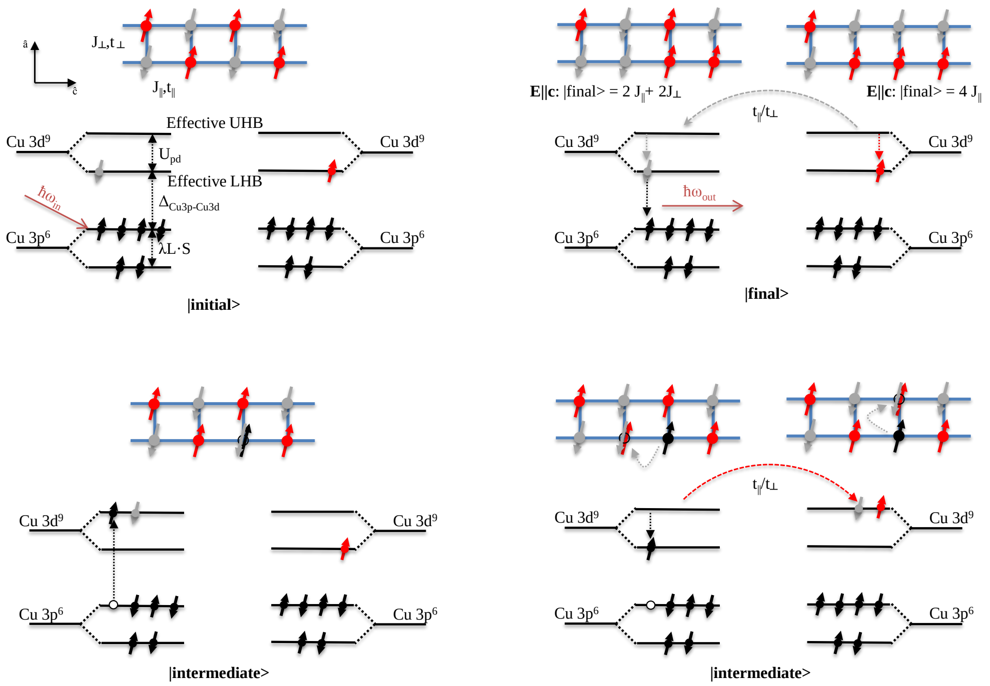

Figure 5.16.: Pictorial model of the two-magnon spin flip excitation process. Top left is the initial state, at the bottom are the intermediate states and top right is the final state.

fer of Cu-2p states is depicted in figure 5.16 [16]. In the top left the initial state is depicted. The copper 3p orbital is split due to spin orbit coupling, and the copper 3d orbitals is spitted into an effective LHB and UHB. The first step is a transition from Cu-3p to the unoccupied UHB which requires the energy of $\Delta_{Cu3p-Cu3d} + U_{pd}$ which leads to a hole in the Cu-3p and a double occupied state in Cu-3d. This intermediate states are depicted in the bottom half of figure 5.13. In a final step (depicted in the top right) a Raman shifted photon is emitted. Each broken spin bond contributes to the Raman shift with an energy of $J/2$. In this model the energy loss is determined by the number of broken spin bonds. This leads to a Raman shift of 2 $J_{||}$ for hopping along the rungs of the ladder or $J_{\perp} + J_{||}$ for hopping along the legs of the ladder. In principle the important cases of two-magnon scattering in SLCs are scattering along the rungs and legs of the ladder, two-magnon scattering from the zone center i.e. $q = 0$ and inter-ladder spin-flip excitations between neighbored ladders, which occur at the energy of 2 $J_{||} + J_{\perp}$. The shift of ΔE_{mag} in LCCO can be explained by anisotropies of $J_{||}$ and $J_{\perp}$, with $J_{||(\perp)} = 2t_{||(\perp)}/U_{pd}$. However, the isotropic ΔE_{mag}^{max} in SCO indicates an anisotropic U_{pd}. Furthermore, the arise of low energy contribution in the SCO spectra results in a screening of U_{pd} when holes are

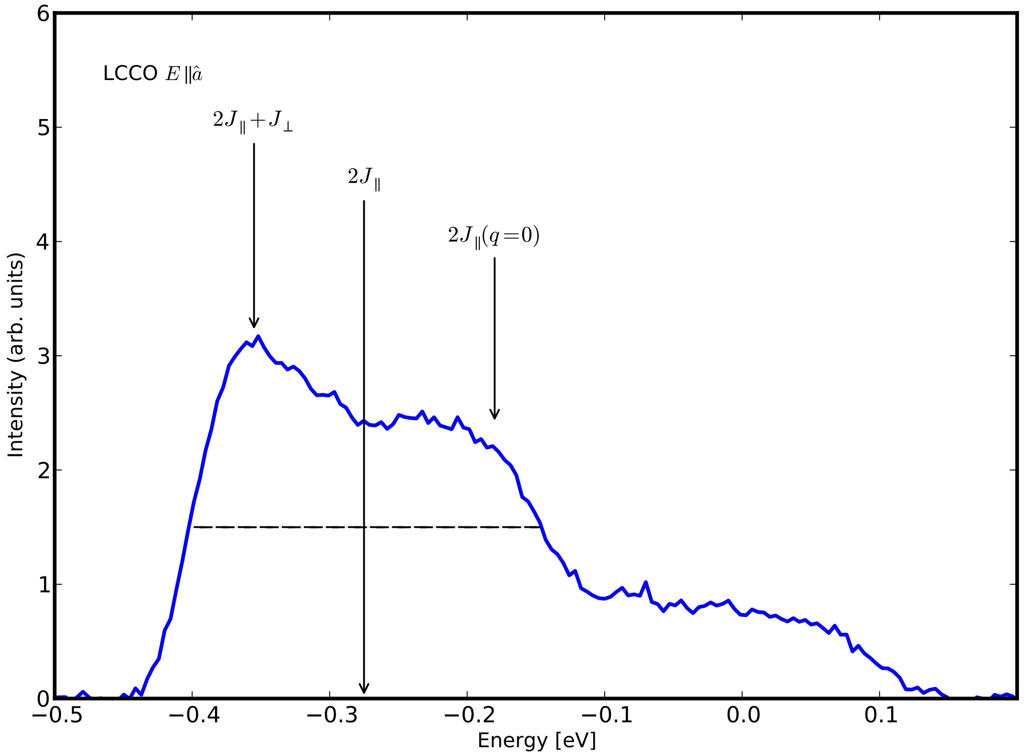

Figure 5.17.: Line shape analysis of the two-magnon excitation spectra of LCCO polarised along the a-axis at 80 eV.

doped into the O-2p orbital. This screening effect is a new observation. A line shape analysis of the two-magnon excitation spectra exemplary shown in figure 5.17 was performed yielding the parameters listed in table 5.1. The obtained values for LCCO are in good agreement with local-density approximation calculations [113]. Neutron scattering data for SCO found a slightly lager anisotropy of $J_{\|}$ and $J_{\perp}$ [114]. The enhancement of $J_{\perp,SCO}$ coincides with a reduction of $U_{pd\perp,SCO}$. So the screening contribution of U_{pd} in SCO develops predominantly along the rungs of the ladder,

	$La_6Ca_8Cu_{24}O_{41}$	$Sr_{41}Cu_{24}O_{41}$
$J_{\|}$	140 ± 10 meV	128 ± 10 meV
$J_{\perp}$	80 ± 10 meV	107 ± 10 meV
$t_{\|}$	529 ± 40 meV	486 ± 40 meV
$t_{\perp}$	400 ± 40 meV	400 ± 40 meV
$U_{\|,pd}$	4.0 ± 0.03 eV	3.7 ± 0.03 eV
$U_{\perp,pd}$	4.0 ± 0.03 eV	3 ± 0.03 eV

Table 5.1.: Superexchange along the legs ($J_{\|}$) and the rungs ($J_{\perp}$), kinetic energies along the legs ($t_{\|}$) and the rungs ($t_{\perp}$), and correlation energies along the legs ($U_{\|,pd}$) and the rungs ($U_{\perp,pd}$) of the undoped spin-ladder $La_6Ca_8Cu_{24}O_{41}$ and the hole-doped spin-ladder $Sr_{14}Cu_{24}O_{41}$.

which can be argued as an indication of a paired hole state.

In conclusion the VUV-Raman technique was successfully applied to investigate the magnetic properties of SLCs revealing Coulomb on-site repulsion energies U_{pd}, superexchange energies J and hopping matrix elements t. A screening of U_{pd} was observed and upon doping a paired hole state can be found along the rungs of the ladder.

Paper IV

Electronic Screening-Enhanced Hole Pairing in Two-Leg Spin Ladders Studied by High-Resolution Resonant Inelastic X-Ray Scattering at Cu M Edges

A. Rusydi, A. Goos, S. Binder, A. Eich, K. Botril, P. Abbamonte, X. Yu, M. B. H. Breese, H. Eisaki, Y. Fujimaki, S. Uchida, N. Guerassimova, R. Treusch, J. Feldhaus, R. Reininger, M. V. Klein, and M. Rübhausen

Physical Review Letter ***113****, 067001 (2014)*

PRL 113, 067001 (2014) PHYSICAL REVIEW LETTERS week ending 8 AUGUST 2014

Electronic Screening-Enhanced Hole Pairing in Two-Leg Spin Ladders Studied by High-Resolution Resonant Inelastic X-Ray Scattering at Cu *M* Edges

A. Rusydi,[1,2,3,*] A. Goos,[1] S. Binder,[1] A. Eich,[1] K. Botril,[1] P. Abbamonte,[4] X. Yu,[3] M. B. H. Breese,[2,3]
H. Eisaki,[5] Y. Fujimaki,[6] S. Uchida,[6] N. Guerassimova,[7] R. Treusch,[7] J. Feldhaus,[7]
R. Reininger,[8] M. V. Klein,[4] and M. Rübhausen[1,2,†]
[1]*Institut für Angewandte Physik, Universität Hamburg, Jungiusstraße 11, D-20355 Hamburg, Germany*
and Center for Free Electron Laser Science (CFEL), Notkestraße 85, D-22607 Hamburg, Germany
[2]*NUSSNI-NanoCore, Department of Physics, National University of Singapore, Singapore 117542, Singapore*
[3]*Singapore Synchrotron Light Source, National University of Singapore, Singapore 117603, Singapore*
[4]*Physics Department and Frederick Seitz Materials Research Laboratory, University of Illinois, Urbana, Illinois 61801, USA*
[5]*Nanoelectronics Research Institute, AIST, 1-1-1 Central 2, Umezono, Tsukuba, Ibaraki 305-8568, Japan*
[6]*Department of Superconductivity, University of Tokyo, Bunkyo-ku, Tokyo 113, Japan*
[7]*Photon Science, DESY, Notkestraße 85, D-22607 Hamburg, Germany*
[8]*Advanced Photon Source, Argonne National Laboratory, Argonne, Illinois 60439, USA*

(Received 7 January 2014; published 4 August 2014)

We study the electronic screening mechanisms of the effective Coulomb on-site repulsion in hole-doped $Sr_{14}Cu_{24}O_{41}$ compared to undoped $La_6Ca_8Cu_{24}O_{41}$ using polarization dependent high-resolution resonant inelastic x-ray scattering at Cu *M* edges. By measuring the energy of the effective Coulomb on-site repulsion and the spin excitations, we estimate superexchange and hopping matrix element energies along rungs and legs, respectively. Interestingly, hole doping locally screens the Coulomb on-site repulsion reducing it by as much as 25%. We suggest that the increased ratio of the electronic kinetic to the electronic correlation energy contributes to the local superexchange mediated pairing between holes.

DOI: 10.1103/PhysRevLett.113.067001 PACS numbers: 74.78.-w, 71.27.+a, 71.45.Gm, 74.25.Jb

As pointed out by Hubbard, electronic screening in condensed matter systems is an example for a correlation effect [1]. Recent examples of the importance of electronic screening processes are the phase transitions in correlated materials such as in C_{60} [2] and in the $BaFe_2As_2$ family [3].

Quasi-one-dimensional spin-ladder compounds (SLCs) such as $(La,Sr)_{14-x}Ca_xCu_{24}O_{41}$ are an ideal example to study electronic screening effects of correlations energies; i.e., correlation energies are lower when electronic screening of Coulomb interactions is present. The SLCs have as a key-structural element copper-oxygen bonds that form Cu_2O_3 ladders and CuO_2 chains [4]. They contain the basic physics given by the competition between the kinetic energy determined by the hopping matrix elements t, the electron-electron interaction (or electronic correlation) energies driven by on-site Coulomb repulsions, and superexchange energies J. Indeed, SLCs show striking properties: superconductivity under high pressure [5], a gapped spin-liquid state [6], charge-density waves [7–11], as well as a paired-hole state [12,13]. This rich physics is a result of competing energy scales that foster a large number of nearly degenerate ground states [13–17].

In this Letter, we study in unprecedented detail the screening of electronic correlation energies, superexchange, and kinetic energies in undoped $La_6Ca_8Cu_{24}O_{41}$ (LCCO) and hole-doped $Sr_{14}Cu_{24}O_{41}$ (SCO). We have developed and used a vacuum-ultraviolet (VUV) off-axis parabolic double-monochromator Raman spectrometer for high-resolution resonance inelastic x-ray scattering (RIXS) at the Free Electron Laser Hamburg (FLASH) of DESY. This allows us to measure and distinguish magnetic and phonon excitations with orbital selectivity at the Cu M_3 edges (Cu-$3p \rightarrow 3d$) and the Cu M_1 edge (Cu-$3s \rightarrow 4p$), and thus to reveal the electronic correlation and superexchange energies, which are then used to determine the hopping matrix elements in LCCO and SCO. The energy resolution was set to ~24 meV. We have used sandblasted Si as the reference to further define elastic, Stokes, and anti-Stokes lines for calibration purposes. All RIXS spectra were corrected to the FLASH intensity. The samples were characterized using resonant soft x-ray scattering, x-ray absorption [9,11,12], and UV-Raman spectroscopy [13]. More details on the RIXS measurements are shown in the Supplemental Material [18].

Figures 1(a) and 1(b) display x-ray absorption spectroscopy (XAS) and FLASH intensities at the Cu M_3 edge and Cu M_1 edge from SCO, respectively. Figure 1(c) shows a schematic diagram of the electronic band structure of LCCO and SCO. The bare electronic correlation can be described by the bare Coulomb on-site repulsion ($U_{dd} \sim 10$–12 eV for cuprates [2,23,24]) defined by the Cu-$3d$ orbitals. This splits Cu-$3d$ states exhibiting the bare lower Hubbard band (LHB) and the bare upper Hubbard band (UHB). However, a downfolding of the Hamiltonian,

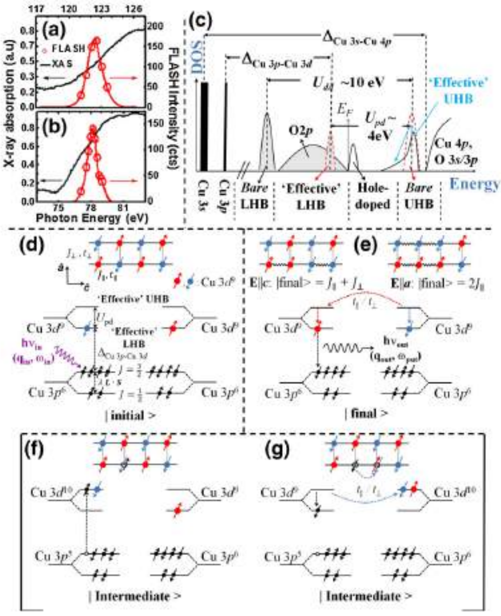

FIG. 1 (color online). X-ray absorption at (a) Cu-$3p$ → Cu-$3d$ and (b) Cu-$3s$ → Cu-$4p$ M-edge transitions and incident photon energies selected for resonance Raman scattering (open bullets) together with the “white-light” intensity distribution of FLASH (red lines). (c) Proposed electronic band structure of the spin-ladder compounds (SLCs) denoting the relevant energy scales for transitions from the Cu-$3p$ and Cu-$3s$ states as well as the correlation energies splitting the states close to the Fermi level. Occupied states are shaded in gray. Dashed lines denote the undoped case, with no accessible electronic states at the Fermi level (E_F). (d) The spin ladder with its different superexchange parallel to the leg (along $\hat{c}$) and parallel to the rung (along $\hat{a}$) of the ladder. (e) The excited final spin state representing the excitation of two magnons. (f) and (g) Intermediate states after absorption of the incident photon outlining the relevant electronic processes between neighboring Cu sites.

i.e., representing electrons from high energy bands by effective electrons from low energy bands, would screen U_{dd} yielding to a reduced *effective* Coulomb on-site repulsion [25]. In this scenario, the effective low energy band needs to be clearly separated and decoupled from high energy degrees of freedom and, very importantly, there is only one dominant effective correlation energy, and without involving O-p orbitals. On the other hand, in SLCs the O-$2p$ bands are closest to the Fermi level [9,12] and thus may strongly affect the effective low energy bands. Strong hybridizations between Cu-$3d$ and O-$2p$ orbitals [15,23] influence U_{dd} and further modify the bare LHB and bare UHB, normalizing them to an effective LHB and effective UHB, respectively. We call this U_{pd}, an effective electronic correlation energy due to strong Cu-$3d$ and O-$2p$ hybridization. This view is further supported by the fact that in doped SCO the holes have more O-$2p$ character [9,12]. Theoretically, but yet to be proven experimentally, doping should, therefore, result in a significant change in U_{pd} and this can, in principle, yield an anisotropic U_{pd} [25]. Our M-edge RIXS measurement aims to reveal U_{pd} and its anisotropy, if any, for undoped LCCO and doped SCO.

By tuning the incoming photon energy to the M_3 edge, effective electronic correlation energies can be studied through the so-called *resonance effect*. Hereby, we are accessing spin excitation via matrix elements outlined in Figs. 1(d)–1(g) as discussed later. Upon doping, the O-$2p$ orbitals host the holes [9,11]. Furthermore, because the Cu-$3d$ orbitals hybridize with the O-$2p$ orbitals close to the Fermi level [see Fig. 1(c)], they determine the properties of the low-energy electronic states [12,26]. In contrast, the Cu-$4p$ orbitals reside well above the Fermi level and hybridize with the O-$3p$ orbitals, thus allowing the coupling of photons to oxygen related phonons at the M_1 edge [see also Fig. 1(c)].

Figure 2(a) highlights the different nature of the excitations for the Cu M_1 and M_3 edge. Indeed, we observe strong phonon excitations for incident photon energies of ~122 eV and spin excitations for incident photon energies of ~80 eV. At ~122 eV strong two-phonon scattering can be seen at 120 meV in agreement with visible Raman scattering [13,27]. Figure 2(b) shows the high-resolution

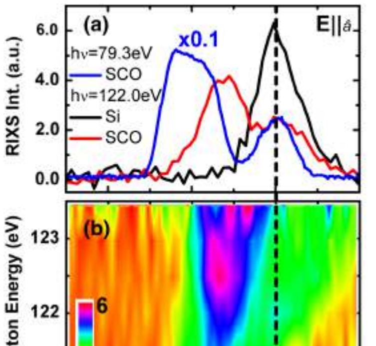

FIG. 2 (color online). (a) Raman spectra (Stokes side is denoted by negative energies) taken at 79.3 and 122.0 eV from the hole-doped $Sr_{14}Cu_{24}O_{41}$ (SCO) with the polarization along the rung ($E\|\hat{a}$) and the elastic line from sandblasted Si for reference. (b) Contour plot of the incident photon energy versus excitation energy (Raman shift) of SCO for $E\|\hat{a}$ showing the resonance behavior of the low-energy phonon excitations. The scale of contour plots is shown.

resonance profile at the Cu-M_1 edge with a resonance energy of 122.5 eV. For increasing incident photon energies, we observe the development of one-phonon scattering from oxygen modes below 100 meV Raman shift also in agreement with visible Raman scattering [13,27]. As reference, for Si, we only observe elastic contributions. At ~80 eV higher-energy inelastic scattering can be seen from double spin-flip-two-magnon excitation.

Our main observation relates to the dependence of the spin-flip excitation spectrum on the incident photon energy, polarization, and with doping as shown in Fig. 3. The resonance dependence of the excitation spectrum of LCCO can be seen in Figs. 3(a) and 3(b) as a contour plot for polarizations along the rung ($E\|\hat{a}$) and the leg ($E\|\hat{c}$), respectively. In Figs. 3(c) and 3(d) spectra at selected energies of 78, 79, and 80 eV are displayed for $E\|\hat{a}$ and $E\|\hat{c}$, respectively. For the lowest energy close to the XAS edge at 78 eV, a strong excitation is evident at around 90 meV Raman shift that corresponds to a one-magnon excitation [28–30] at the spin-gap energy with momentum transfer $(q) \approx 0$. The one-magnon excitation couples to photons by a finite spin-orbit coupling (≈280 meV) of the Cu-3d orbitals [31,32]. Interestingly, the one-magnon excitation exhibits a strong anisotropy. For $E\|\hat{a}$ magnetic bonds are broken along the $\hat{c}$ direction, along the leg of the ladder, allowing the propagation of long distance, i.e., small q, magnetic excitations [see Figs. 1(d) and 1(e)]. For $E\|\hat{a}$, one-magnon excitations are suppressed due to the geometry of ladders. The one-magnon excitation for LCCO is about 6 times stronger as compared to the two-magnon peak. The inset of Fig. 3(a) displays the sharp resonance of the two-magnon peak ~4 eV above the XAS edge. A strong two-magnon excitation spectrum develops in an energy range up to $E_{\rm mag}^{\rm max} \approx 400$ meV with a resonance energy of about 79.3 eV as seen in Fig. 3(a) (see inset) and Fig. 3(c).

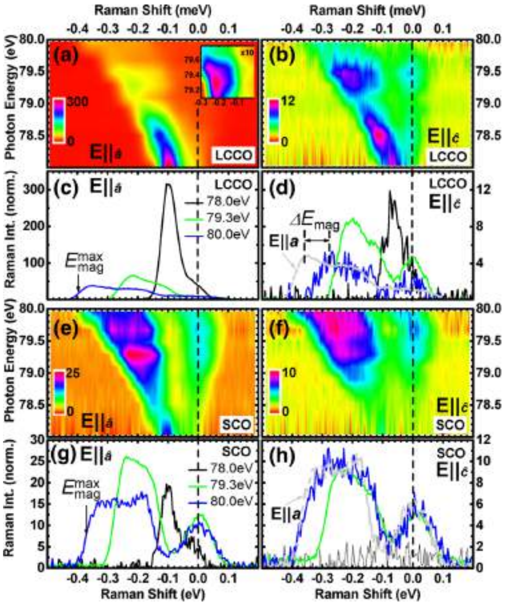

FIG. 3 (color online). Contour plot and resonance profile of resonant inelastic x-ray scattering (RIXS) from undoped $La_6Ca_8Cu_{24}O_{41}$ (LCCO) (a),(c) for $E\|\hat{a}$ (along the rungs) and (b),(d) for $E\|\hat{c}$ (along the leg). The inset of (a) enlarges the region of the two-magnon resonance energy. The maximum two-magnon energy is denoted as $E_{\rm mag}^{\rm max}$ of about 400 meV. The spectrum at 80 eV for ($E\|\hat{c}$) (a gray dotted line) shows the anisotropy of the peak energy denoted as $\Delta E_{\rm mag}^{\rm max}$ of about 80 ± 10 meV. Contour plot and resonance profile of resonant inelastic x-ray scattering (RIXS) from doped $Sr_{14}Cu_{24}O_{41}$ (SCO) (e),(g) for $E\|\hat{a}$ polarization and (f),(h) for $E\|\hat{c}$ polarization. In this case the $E_{\rm mag}^{\rm max}$ and $\Delta E_{\rm mag}^{\rm max}$ are about 375 and 5 ± 10 meV, respectively. For comparison, we replot the E||â spectrum of LCCO and SCO in (d) and (h), respectively.

Based on the Fleury-Loudon Hamiltonian [33] a two-magnon process that considers explicitly a transition of an electron from Cu-3p states is shown in Figs. 1(d) and 1(e). In Fig. 1(d) we display the initial state. The Cu-3p orbitals are split by the spin-orbit coupling, while the Cu-3d orbitals are split by U_{pd}. The initial step relies on the dipole allowed transition due to the ($\mathbf{P}\cdot\mathbf{A}$)-matrix element from the Cu-3p orbital to the unoccupied *effective* UHB. This results in a doubly occupied site and a hole in the Cu-3p state forming a Cu-3d^{10} and a Cu-3p^5 in the intermediate state costing an energy of $\Delta_{\rm Cu3\it{p}\text{-}\rm Cu3\it{d}} + U_{pd}$ being supplied by the incident photon as shown in Figs. 1(f) and 1(g). In the final step we have a transition from effective UHB back into the Cu-3p^5 emitting via the $\mathbf{P}\cdot\mathbf{A}$-matrix element a Raman shifted photon. The energy loss or Raman shift is then given by the effective number of broken spin bonds [cf. Fig. 1(f)]. Within an Ising model each broken bond corresponds to $J/2$. In two-dimensional antiferromagnetic cuprates this would correspond to $3J$, i.e., the typical energy of a two-magnon excitation. In the SLCs the anisotropy of the kinetic energy needs to be considered. This leads for a hopping along the leg to an energy of $(J_\parallel + J_\perp)$ or for hopping along the rungs to $2 \times J_\parallel$.

The effective scattering Hamiltonian can be projected onto spin states [33] and written as

$$\begin{aligned} H_{\rm int}(q,\omega) &= \frac{(t_{\perp/\parallel})^2}{\Delta_{{\rm Cu3}p-{\rm Cu3}d} + U_{pd} - \hbar\omega_{\rm inc}} \\ &\quad \times \sum_{k,q} P(k,q)\vec{S}_{k+q/2}\cdot\vec{S}_{k-q/2} \\ &\underset{\substack{\hbar\omega_{\rm inc}\approx \\ (\Delta_{{\rm Cu3}p-{\rm Cu3}d})}}{\cong} J\sum_{k,q} P(k,q)\vec{S}_{k+q/2}\cdot\vec{S}_{k-q/2}. \end{aligned} \qquad (1)$$

As displayed in Fig. 1(c), $\Delta_{{\rm Cu3}p-{\rm Cu3}d}$ is ~75 eV. Accordingly, U_{pd} affects the resonance energy of the spin excitation relative to the XAS edge. In the momentum transfer $q \rightarrow 0$ limit, we find for incident photon energies close to the energy difference between Cu-3p and Cu-3d states ($\Delta_{\mathrm{Cu}3p-\mathrm{Cu}3d} + U_{pd} \cong 80$ eV), the Fleury-Loudon Hamiltonian [33] representing also two-magnon Raman scattering for visible photon energies. Furthermore, Donkov and Chubukov [34] as well as Verney, Gingras, and Devereaux [35] have calculated the spin susceptibility from the Fleury-Loudon Hamiltonian for $q \neq 0$ limit concluding that symmetry selection rules are still valid for $q \rightarrow 0$. The dispersion of the two-magnon excitation does not represent the single-particle dispersion, but rather the q dependence of the magnon-magnon interactions through the vertex correction that results in an effective q-dependent vertex.

For LCCO, we find surprisingly large anisotropies in intensity and in the energy of the spin-flip excitations denoted by $\Delta E_{\mathrm{mag}} \approx 80 \pm 10$ meV due to the anisotropic superexchange $J_{\parallel(\perp)} \equiv 2t_{\parallel(\perp)}/U_{pd}$ between legs (rungs) (see discussion below). Based on M-edge RIXS, U_{pd} is isotropic [see Figs. 2(a) and 2(b)].

Upon the doping of holes into the O-2p state in SCO [7,24], which is the isostructural doped counterpart of LCCO [4], we find the following striking behavior as shown in Figs. 2(e)–2(h): First, the zone center ($q = 0$) magnetic excitation is strongly suppressed by a factor of 20 in intensity. Second, the maximum energy of the two-magnon excitation is nearly doping independent $E^{\mathrm{max}}_{\mathrm{mag}} \approx 375$ meV. The anisotropy of the superexchange energy is suppressed, yielding nearly isotropic energies along the legs and along the rungs with $\Delta E \approx 5 \pm 10$ meV [see Figs. 2(g) and 2(h)]. More importantly, the resonance seen in the two-magnon channel broadens [compare Figs. 2(a) and 2(e)] and develops a low-energy contribution. Since the resonance energy is given as ($\Delta_{\mathrm{Cu}3p\text{-}\mathrm{Cu}3d} + U_{pd}$) this low-energy contribution signals the enhanced *screening* of U_{pd}, i.e., a reduction of the energy of U_{pd}, when holes are doped into the O-2p orbital.

This reduction of U_{pd} is a new observation. Screening of correlation energies is most relevant for the understanding of correlated materials [3,16,36]. This also implies that the holes doped into the spin ladder enhance locally $J(\sim t^2/U_{pd})$ [2,25]. We would like to point out that calculations of the spin susceptibility from Eq. (1) lead to excitation energies that are within 10% equal to the estimates from a simple Ising model in two-dimensional cuprates [37]. From both parameters the anisotropic t can then be calculated [38,39].

For the following discussion, we derive the relevant parameters, yielding $t_\perp$ ($t_\parallel$) from the measured values of $U_{pd,\perp}$ ($U_{pd,\parallel}$) and the corresponding $J_\perp$ ($J_\parallel$) from the two-magnon excitation spectrum. In the ladders of SLCs each spin is surrounded by three nearest neighbors yielding three broken bonds with an energy of $J/2$ in the $S = 1/2$ case [cf. Fig. 1(e)]. Considering the anisotropy of the hopping integrals $t_\parallel$ and $t_\perp$, the superexchange anisotropy yields as spin flip energy, $E_{\mathrm{spin\,flip}} = 2(J_\parallel/2) + J_\perp/2$ or as maximum two-magnon energy $E^{\mathrm{max}}_{\mathrm{mag}} = 2J_\parallel + J_\perp$. This coincides for the isotropic two-dimensional case with 3J. The results are summarized in Table I. For LCCO, the superexchange energy is anisotropic with $J_\parallel = 140 \pm 10$ and $J_\perp = 80 \pm 10$ meV leading to a maximum two-magnon energy of about 360 ± 10 meV = $E^{\mathrm{max}}_{\mathrm{mag}}$ (see Fig. 3 and also the Supplemental Material [18]). Whereas the effective correlation energy is isotropic with $U_{\parallel,pd} = U_{\perp,pd} \sim 4.00 \pm 0.03$ eV resulting in $t_\parallel = 529 \pm 40$ and $t_\perp = 400 \pm 40$ meV, in good agreement with local-density approximation calculations [40]. In SCO, the magnetic peaks become more isotropic leading to $J_\parallel = 128 \pm 10$ and $J_\perp = 107 \pm 10$ meV. Noting that inelastic neutron scattering [41] and ^{17}O NMR [6] measurements suggested that $J_\perp$ and $J_\parallel$ are about 72–80 and 130–160 meV, respectively, yielding a higher superexchange anisotropy as compared to the values measured by M-edge RIXS. While the $J_\parallel$ is close to the value given by inelastic neutron scattering, the $J_\perp$ is slightly larger, reducing the overall anisotropy. Another surprising result is the anisotropy of U_{pd} in SCO (cf. Table I). This anisotropy is essentially embedded in the downfolding procedure that would lead to an effective U [25], but is shown here experimentally to be relevant. Since U_{pd} and J vary as a function of doping, $t_\parallel$ and $t_\perp$ change to 486 ± 40 and 400 ± 40 meV, respectively, also in good agreement with model calculations [40]. Thus, the enhancement of $J_{\perp,\mathrm{SCO}}$ is equivalent with the reduction of $U_{pd\,\mathrm{SCO}}$ along the $\hat{a}$ direction of about 1 eV. This is indeed confirmed by the changes in U_{pd} [compare Figs. 3(a) and 3(e)]. In undoped LCCO U_{pd} is isotropic, whereas in doped SCO the redistribution of holes in the rungs and legs lead to the anisotropic U_{pd} [12,13]. A screening contribution of U_{pd} develops predominantly along the rungs, where the holes reside in the O-p orbitals and along which they pair accordingly. This effect is negligible along the legs [compare Figs. 3(e) with 3(f)]. Thus, we argue that the anisotropic screening of U_{pd} along the rung triggers the formation of the paired hole state. The observed asymmetry of U_{pd} upon hole doping will have strong consequences for other more isotropic cuprate systems as well.

TABLE I. Superexchange along the legs ($J_\parallel$) and the rungs ($J_\perp$), hopping matrix element energies along the legs ($t_\parallel$) and the rungs ($t_\perp$), and correlation energies along the legs ($U_{\parallel,pd}$) and the rungs ($U_{\perp,pd}$) of the undoped spin-ladder $La_6Ca_8Cu_{24}O_{41}$ and the hole-doped spin-ladder $Sr_{14}Cu_{24}O_{41}$ extracted from resonant inelastic x-ray scattering at Cu M edges.

	$La_6Ca_8Cu_{24}O_{41}$	$Sr_{41}Cu_{24}O_{41}$
$J_\parallel$	140 ± 10 meV	128 ± 10 meV
$J_\perp$	80 ± 10 meV	107 ± 10 meV
$t_\parallel$	529 ± 40 meV	486 ± 40 meV
$t_\perp$	400 ± 40 meV	400 ± 40 meV
$U_{\parallel,pd}$	4.00 ± 0.03 eV	3.70 ± 0.03 eV
$U_{\perp,pd}$	4.00 ± 0.03 eV	3.00 ± 0.03 eV

In conclusion, from the polarization dependent RIXS measurements, we obtain for doped and undoped SLCs the effective Coulomb on-site repulsion energy U_{pd}, superexchange energies J, and estimate anisotropic hopping matrix elements t along the leg and the rung of the ladder. We find that the local pairing of holes is promoted by a local screening of the correlation energy U_{pd}. Upon doping holes into the O-$2p$ states, local screening of U_{pd} leads to a local enhancement of the superexchange and triggers the formation of the paired hole state along the rung. Our result shows the potency of high-resolution RIXS at the Cu M edges to determine competing energy scales in correlated electron systems.

We would like to acknowledge technical support from Holger Weigelt, Benjamin Schulz, Pelangi Saichu, Jason Lim, and Wong How Kwong, and discussions with Dirk Manske, Wilfried Wurth, George Sawatzky, Jochen Schneider, and Lance Cooper. We acknowledge financial support by BMBF under 05K10GUD as well as DFG through Ru 773/4-1 & 4-2, and by Singapore National Research Foundation under its Competitive Research Funding (NRF-CRP 8-2011-06 and NRF2008NRF-CRP002024), MOE Tier 2 (MOE2010-T2-2-121), and FRC and NUS YIA.

*phyandri@nus.edu.sg
†michael.ruebhausen@desy.de

[1] J. Hubbard, Proc. R. Soc. A **276**, 238 (1963).
[2] M. B. J. Meinders, J. van den Brink, J. Lorenzana, and G. A. Sawatzky, Phys. Rev. B **52**, 2484 (1995).
[3] P. Werner, M. Casula, T. Miyake, F. Aryasetiawan, A. J. Millis, and S. Biermann, Nat. Phys. **8**, 331 (2012).
[4] E. M. McCarron III, M. Subramanian, J. Calabrese, and R. Harlow, Mater. Res. Bull. **23**, 1355 (1988).
[5] K. Kojima, N. Motoyama, H. Eisaki, and S. Uchida, J. Electron Spectrosc. Relat. Phenom. **117–118**, 237 (2001).
[6] T. Imai, K. R. Thurber, K. M. Shen, A. W. Hunt, and F. C. Chou, Phys. Rev. Lett. **81**, 220 (1998).
[7] G. Blumberg, P. Littlewood, A. Gozar, B. S. Dennis, N. Motoyama, H. Eisaki, and S. Uchida, Science **297**, 584 (2002).
[8] B. Gorshunov, P. Haas, T. Rõõm, M. Dressel, T. Vuletić, B. Korin-Hamzić, S. Tomić, J. Akimitsu, and T. Nagata, Phys. Rev. B **66**, 060508 (2002).
[9] P. Abbamonte, G. Blumberg, A. Rusydi, A. Gozar, P. G. Evans, T. Siegrist, L. Venema, H. Eisaki, E. D. Isaacs, and G. A. Sawatzky, Nature (London) **431**, 1078 (2004).
[10] A. Rusydi, P. Abbamonte, H. Eisaki, Y. Fujimaki, G. Blumberg, S. Uchida, and G. A. Sawatzky, Phys. Rev. Lett. **97**, 016403 (2006).
[11] A. Rusydi, P. Abbamonte, H. Eisaki, Y. Fujimaki, S. Smadici, N. Motoyama, S. Uchida, Y.-J. Kim, M. Rübhausen, and G. A. Sawatzky, Phys. Rev. Lett. **100**, 036403 (2008).
[12] A. Rusydi, M. Berciu, P. Abbamonte, S. Smadici, H. Eisaki, Y. Fujimaki, S. Uchida, M. Rübhausen, and G. A. Sawatzky, Phys. Rev. B **75**, 104510 (2007).
[13] A. Rusydi, W. Ku, B. Schulz, R. Rauer, I. Mahns, D. Qi, X. Gao, A. T. S. Wee, P. Abbamonte, H. Eisaki, Y. Fujimaki, S. Uchida, and M. Rübhausen, Phys. Rev. Lett. **105**, 026402 (2010).
[14] E. Dagotto, J. Riera, and D. Scalapino, Phys. Rev. B **45**, 5744 (1992).
[15] M. B. J. Meinders, H. Eskes, and G. A. Sawatzky, Phys. Rev. B **48**, 3916 (1993).
[16] A. Rusydi, R. Rauer, G. Neuber, M. Bastjan, I. Mahns, S. Müller, P. Saichu, B. Schulz, S. G. Singer, A. I. Lichtenstein, D. Qi, X. Gao, X. Yu, A. T. S. Wee, G. Stryganyuk, K. Dörr, G. A. Sawatzky, S. L. Cooper, and M. Rübhausen, Phys. Rev. B **78**, 125110 (2008).
[17] P. Phillips, Rev. Mod. Phys. **82**, 1719 (2010).
[18] See Supplemental Material at http://link.aps.org/supplemental/10.1103/PhysRevLett.113.067001, which includes Refs. [19–22], for high-energy resonant inelastic x-ray scattering.
[19] P. Kuiper, J.-H. Guo, C. Såthe, L.-C. Duda, J. Nordgren, J. J. M. Pothuizen, F. M. F. de Groot, and G. A. Sawatzky, Phys. Rev. Lett. **80**, 5204 (1998).
[20] X. Yu, O. Wilhelmi, H. O. Moser, S. V. Vidyaraj, X. Gao, A. T. Wee, T. Nyunt, H. Qian, and H. Zheng, J. Electron Spectrosc. Relat. Phenom. **144–147**, 1031 (2005).
[21] B. Schulz, J. Bäckström, D. Budelmann, R. Maeser, M. Rübhausen, M. V. Klein, E. Schoeffel, A. Mihill, and S. Yoon, Rev. Sci. Instrum. **76**, 073107 (2005).
[22] N. Motoyama, T. Osafune, T. Kakeshita, H. Eisaki, and S. Uchida, Phys. Rev. B **55**, R3386 (1997).
[23] J. Zaanen, G. A. Sawatzky, and J. W. Allen, Phys. Rev. Lett. **55**, 418 (1985).
[24] K. Wohlfeld, A. M. Oleś, and G. A. Sawatzky, Phys. Rev. B **81**, 214522 (2010).
[25] M. Imada and T. Miyake, J. Phys. Soc. Jpn. **79**, 112001 (2010).
[26] N. Nücker, M. Merz, C. A. Kuntscher, S. Gerhold, S. Schuppler, R. Neudert, M. S. Golden, J. Fink, D. Schild, S. Stadler, V. Chakarian, J. Freeland, Y. U. Idzerda, K. Conder, M. Uehara, T. Nagata, J. Goto, J. Akimitsu, N. Motoyama, H. Eisaki, S. Uchida, U. Ammerahl, and A. Revcolevschi, Phys. Rev. B **62**, 14 384 (2000).
[27] A. Gozar, G. Blumberg, B. S. Dennis, B. S. Shastry, N. Motoyama, H. Eisaki, and S. Uchida, Phys. Rev. Lett. **87**, 197202 (2001).
[28] M. G. Cottam and D. J. Lockwood, Phys. Rev. B **31**, 641 (1985).
[29] M. L. Tacon, G. Ghiringhelli, J. Chaloupka, M. M. Sala, V. Hinkov, M. W. Haverkort, M. Minola, M. Bakr, K. J. Zhou, S. Blanco-Canosa, C. Monney, Y. T. Song, G. L. Sun, C. T. Lin, G. M. D. Luca, M. Salluzzo, G. Khaliullin, T. Schmitt, L. Braicovich, and B. Keimer, Nat. Phys. **7**, 725 (2011).
[30] J. Schlappa, T. Schmitt, F. Vernay, V. N. Strocov, V. Ilakovac, B. Thielemann, H. M. Rønnow, S. Vanishri, A. Piazzalunga, X. Wang, L. Braicovich, G. Ghiringhelli, C. Marin, J. Mesot, B. Delley, and L. Patthey, Phys. Rev. Lett. **103**, 047401 (2009).
[31] G. Ghiringhelli, L. H. Tjeng, A. Tanaka, O. Tjernberg, T. Mizokawa, J. L. de Boer, and N. B. Brookes, Phys. Rev. B **66**, 075101 (2002).

[32] M. W. Haverkort, Phys. Rev. Lett. **105**, 167404 (2010).
[33] P. A. Fleury and R. Loudon, Phys. Rev. **166**, 514 (1968).
[34] A. Donkov and A. V. Chubukov, Phys. Rev. B **75**, 024417 (2007).
[35] F. H. Vernay, M. J. P. Gingras, and T. P. Devereaux, Phys. Rev. B **75**, 020403 (2007).
[36] P. Werner and A. J. Millis, Phys. Rev. Lett. **104**, 146401 (2010).
[37] C. M. Canali and S. M. Girvin, Phys. Rev. B **45**, 7127 (1992).
[38] B. S. Shastry and B. I. Shraiman, Int. J. Mod. Phys. B **05**, 365 (1991).
[39] M. Rübhausen, C. T. Rieck, N. Dieckmann, K.-O. Subke, A. Bock, and U. Merkt, Phys. Rev. B **56**, 14 797 (1997).
[40] T. F. A. Müller, V. Anisimov, T. M. Rice, I. Dasgupta, and T. Saha-Dasgupta, Phys. Rev. B **57**, R12 655 (1998).
[41] R. S. Eccleston, M. Uehara, J. Akimitsu, H. Eisaki, N. Motoyama, and S.-i. Uchida, Phys. Rev. Lett. **81**, 1702 (1998).

6. Conclusion and Outlook

In this thesis the scientific value of Raman spectroscopy for the investigations of the properties of samples in the focus of our scientific interest has been proven. Several different material systems, ranging from bio inorganic model complexes over manganites to high temperature superconductors have been investigated and discussed. Furthermore, three different kinds of Raman spectroscopy have been used in the investigations.

Two classical Raman experiments on bio inorganic samples have been presented. First of all the the bis-μ-oxo vibrational modes in model complexes were investigated and it could be verified by isotope shift, that a peroxo core formed and therefore the structure of the model complexes mimic the structure and function of the natural tyrosinase. Furthermore, the complex is stable at -78 °C for a duration that gives access to optical analysis which allows to investigate the complex in its liquid form for the first time. This is a crucial achievement to recreate the natural process.

Furthermore, a resonance Raman study has been performed on two types of guadinin-quinoline copper complexes to investigate their entatic behaviour. These complexes inherit a metal to ligand charge transfer or a ligand to metal charge transfer depending on the used ligands. The charge transfer functions through different oxidation states of the copper center. By performing resonance Raman spectroscopy in an energy range from 1.72 eV to 4.78 eV resonances were found at 3.4 eV and 4.45 eV for most of the peaks in both Cu^I and Cu^{II} oxidated cores. By comparing these results to theoretical calculations two modes at 788 cm^{-1} and 815 cm^{-1} can be related to vibrations connected to the structure of both oxidation states within the charge transfer process. Therefore, it is possible to directly probe the charge transfer process through observing these modes with Raman spectroscopy.

While traditional Raman studies are a very useful tool in the understanding of structural changes during phase transitions little to no information can be gained about the dynamics of this phase transitions. This changed by the introduction of time-resolved Raman spectroscopy, which made it possible to investigate the exact dynamics of phase changes at picosecond timescales.

Time resolved Raman studies have been performed to investigate the dynamics in high temperature superconductors and manganites. In the case of manganites the melting and recombination of the charged ordered phase in $La_{1-x}Ca_xMnO_3$ was investigated for the dopings x =0.5, 0.55 and 0.76. By observation of the time-depend intensities of the Jahn-Teller mode the temporal evolution of the melting and recombination process of the charge ordered phase could be determined to be at a timescale of around 500 ps in the case of the commensurate dopings. A rise time of the melting of the charge ordered state of 56 ps was found and after 300 ps a sharp decay of 25 ps could be observed. Also a strong interplay between the electronic background and the width of the mode could be observed. Out of phase oscillation of the width of the mode i.e. the energy stored in the lattice and the electron background with a periodicity of 113 ps for the width and 93 ps for the electronic background. This is due to the creation of free charges i.e. polarons by the initial excitation. A delayed response from the lattice leads to a hopping of the free charges to the energetically favorable state. At incommensurate dopings this behaviour is strongly suppressed or not found at all.

The time-resolved Raman study at the high temperature superconductor Bi-2212 investigated the melting and recombination of the superconducting state by observing the temporal evoultion of the superconducting gap. A redistribution of spectral weight was found which indicated a breaking of Cooper pairs. Two different timescales of the reformation of the superconducting gap have been discovered. The first one has a rise of about 2 ps and decays within 7.4 ps. This process can be understood by the coupling of holes to phonons and theoretical calculations show a good agreement to the observed data. Furthermore, a second feature in the recombination of the superconducting state was observed, which sets in at 5 ps and is only lasting for 1.4 ps. This second contribution is related to spin hole interactions.

Also presented in this thesis is a VUV-Raman study at the strongly correlated quasi two dimensional spin-ladder compound $La_6Ca_8Cu_24O_{41}$(LCCO) and the hole doped $Sr_{14-x}Ca_xCu_{24}O_{41}$ (SCO). These are the first experimental results of the newly established VUV-Raman spectrometer at the Free Electron Laser Hamburg by performing polarisation and resonance studies at the copper M-edges. By investigating the effective Coulomb on-side repulsion and spin-excitations the superexchange parameter J and the kinetic energies t could be estimated. Also a screening of the on-site repulsion energy in the intrinsically hole doped case could be observed which leads to an increased superexchange and the formation of paired-hole states.

Furthermore, the newly implemented VUV-Raman setup at FLASH has been discussed in this thesis, an overview of the technical details has been given. A detailed alignment procedure of the spectrometer parts has been developed and presented.

All results in this thesis show the value of Raman spectroscopy in structural investigation as well as the investigation of dynamic processes. In the case of bio inorganic copper complexes the next step should be to investigate charge transfer processes time-dependent with time-resolved Raman spectroscopy in order to learn more about the dynamics of these processes that are very important in nature. In addition other time resolved measurements like XANES could give additional insight. On the technical sight our time resolved Raman setup is now able to measure longer delays by using a chopper and also to independently tune pump and probe energies by using two independent pulsed lasers. Furthermore, it is also a goal to measure these liquid bio inorganic complexes at the VUV-Raman spectrometer at FLASH with the installation of a JET. Also time resolved measurements at the VUV-Raman instrument at FLASH could give an increased insight in the dynamics of all evaluated systems in this thesis. In general the possibilities of time resolved and VUV-Raman combined with the classical structural analysis capability makes Raman spectroscopy an ideal tool to investigate structural, magnetic and electronic dynamics in solids and fluids.

Acknowledgement

This work has been influenced and supported by others. I like to thank

- Prof. Dr. Rübhausen for the opportunity to work in his optics group and providing excellent support and facilities. Also for the possibility to teach some lectures which was a wonderful experience.
- Prof. Dr. Robert H. Blick for the evaluation of this thesis.
- Prof. Dr. Andivo Rusydi for being referee of the oral defence and the fruitful scientific discussions, and his support during the FLASH measurement times.
- Prof. Dr. Sonja Herres-Pawlis and Prof. Dr. Gerald Henkel for providing the bioinorganic Samples.
- Dr. Stephan Binder for helping a lot to complete this work, scientific discussions about biophysics and the fun time in the laboratory, office, and at the scoccer table. Thanks for being a friend.
- Dr. Benjamin Schultz and Dr. Ilka Mahns for introducing me to the UT-3 Raman spectrometer, helping with my work and for always having good ideas regarding alignment, data analysis or time management.
- Pelangi Saichu for the great collaborative work during the time resolved Raman measurements and the FLASH allignment time.
- Dr. Natalia Guerassimova for her support at the FLASH facility and for intoducing me to beamline science.
- Holger Weigelt for his help and support at the VUV-Raman spectrometer and nice chatting during downtime.
- Alina Wetzel and Benjamin Lebsanft for being great colleagues. It was a pleasure to work with you.
- Horst Biederman and the team of the electronic workshop as well as Rolf-Peter Beneke and the team of the mechanical workshop for their fantastic support.
- Petra Roth for her help with administrative issues.

- all current and former members of the Optics group at the institute of applied physics in Hamburg. It was always a nice and pleasant atmosphere.
- all my friends in Hamburg for supporting me all those years.
- my family, which supported me from day one and never lost faith in me.
- Last but not least i would like to thank my girlfriend Andrea Hagedorn who supported me in so many ways. You are a wonderful person.

I would also like to express my gratitude towards the University and city of Hamburg for providing financial support.

List of Publications

- **Electronic Screening-Enhanced Hole Pairing in Two-Leg Spin Ladders Studied by High-Resolution Resonant Inelastic X-Ray Scattering at Cu *M* Edges**, A. Rusydi, A. Goos, S. Binder, A. Eich, K. Botril, P. Abbamonte, X. Yu, M. B. H. Breese, H. Eisaki, Y. Fujimaki, S. Uchida, N. Guerassimova, R. Treusch, J. Feldhaus, R. Reininger, M. V. Klein and M. Rübhausen *Phys. Rev. Lett.* **113**, 067001, (2014)

- **Catching an Entatic State - A Pair of Copper Complexes**, A. Hoffmann, S. Binder, A. Jesser, R. Haase, U. Flörke, M. Gnida, M. S. Stagni, W. Meyer-Klaucke, B. Lebsanft, L. E. Grünig, S. Schneider, M. Hashemi, A. Goos, A. Wetzel, M. Rübhausen, and S. Herres-Pawlis *Angewandte Chemie* **126**, 305–310, (2014)

- **Catalytic Phenol Hydroxylation with Dioxygen: Extension of the Tyrosinase Mechanism beyond the Protein Matrix**, A. Hoffmann, C. Citek, S. Binder, A. Goos, M. Rübhausen, O. Troeppner, I. Ivanović-Burmazović, E. C. Wasinger, T. Daniel P. Stack, and S. Herres-Pawlis *Angewandte Chemie* **125**, 5508–5512 (2013)

- **Observation of room-temperature high-energy resonant excitonic effects in graphene**, I. Santoso, P. K. Gogoi, H. B. Su, H. Huang, Y. Lu, D. Qi, W. Chen, M.A. Majidi, Y.P. Feng, A.T.S. Wee, K.P. Loh, T. Venkatesan, R.P. Saichu, A. Goos, A. Kotlov, M. Rübhausen, A. Rusydi *Phys. Rev. B* **84**, 081403 (2011)

- **UV-light-induced conversion and aggregation of prion proteins**, L. Redecke, S. Binder, M. Elmallah, R. Broadbent, C. Tilkorn, B. Schulz, P. May, A. Goos, A. Eich, M. Rübhausen, C. Betzel *Free Radical Biology and Medicine* **46** 1353-1361 (2009)

- **Two-component Dynamics of the Order Parameter of High Temperature $\mathbf{Bi_2Sr_2CaCu_2O_{8-\delta}}$ Superconductors Revealed by Time-Resolved Raman Scattering**, R. P. Saichu, I. Mahns, A. Goos, S. Binder, P. May, S.

G. Singer, B. Schulz, A. Rusydi, J. Unterhinninghofen, D. Manske, P. Guptasarma, M. S. Williamsen, and M. Rübhausen *Physical Review Letter* **102**, 177044 (2009)

Bibliography

[1] C. V. Raman, “A new radiation,” *Indian J. Phys.*, vol. 2, pp. 387–398, 1928.

[2] G. Landsberg and L. Mandelstam, “Eine neue Erscheinung bei der Lichtzerstreuung in Krystallen,” *Naturwissenschaften*, vol. 16, pp. 557–558, 1928. 10.1007/BF01506807.

[3] A. Smekal, “Zur Quantentheorie der Dispersion,” *Naturwissenschaften*, vol. 11, pp. 873–875, 1923.

[4] S. Bolik, M. Rübhausen, S. Binder, B. Schulz, M. Perbandt, N. Genov, V. Erdmann, S. Klussmann, and C. Betzel, “First experimental evidence for the preferential stabilization of the natural d- over the nonnatural l-configuration in nucleic acids,” *RNA*, vol. 13, pp. 1877–1880, Nov. 2007.

[5] J. Jackson, *Classical Electrodynamics Third Edition.* Wiley, Aug. 1998.

[6] F. Schwabl, *Quantenmechnik.* Springer, 1998.

[7] M. R. Gaberdil, “Quantenmechanik ii.” Skript, 2008.

[8] R. Mattuck, *A Guide to Feynman Diagrams in the Many-Body Problem.* Dover Publications, June 1992.

[9] W. Nolting, *Grundkurs theoretische Physik, Band 7: Vielteilchenphysik.* Springer Berlin Heidelberg; Auflage: 7., aktualisierte Aufl., 2009.

[10] Michael Alexander Rübhausen, *Electronic Correlations in Cuprate Superconductors.* PhD thesis, 1999.

[11] F. Schwabl, *Quantenmechnik für Fortgeschrittene.* Springer, 2005.

[12] J. Bardeen, L. N. Cooper, and J. R. Schrieffer, “Theory of superconductivity,” *Phys. Rev.*, vol. 108, pp. 1175–1204, Dec. 1957.

[13] M. Rübhausen, C. T. Rieck, N. Dieckmann, K.-O. Subke, A. Bock, and U. Merkt, “Inelastic light scattering at high-energy excitations in doped cuprate superconductors,” *Phys. Rev. B*, vol. 56, pp. 14797–14808, Dec 1997.

[14] A. Bock, S. Ostertun, R. Das Sharma, M. Rübhausen, K.-O. Subke, and C. T. Rieck, "Anomalous self-energy effects of the B_{1g} phonon in $\mathrm{y}_{1-x}(\mathrm{Pr},\mathrm{Ca})_x\mathrm{ba}_2\mathrm{cu}_3\mathrm{o}_7$ films," *Phys. Rev. B*, vol. 60, pp. 3532–3537, Aug 1999.

[15] U. Fano, "Effects of configuration interaction on intensities and phase shifts," *Phys. Rev.*, vol. 124, pp. 1866–1878, Dec. 1961.

[16] P. A. Fleury and R. Loudon, "Scattering of light by one- and two-magnon excitations," *Phys. Rev.*, vol. 166, pp. 514–530, Feb. 1968.

[17] J. Unterhinninghofen, D. Manske, and A. Knorr, "Theory of ultrafast nonequilibrium dynamics in d-wave superconductors," *Phys. Rev. B*, vol. 77, pp. 180509–, May 2008.

[18] W. H. Parker, "Modified heating theory of nonequilibrium superconductors," *Phys. Rev. B*, vol. 12, pp. 3667–3672, Nov. 1975.

[19] C. S. Owen and D. J. Scalapino, "Superconducting state under the influence of external dynamic pair breaking," *Phys. Rev. Lett.*, vol. 28, pp. 1559–1561, June 1972.

[20] E. J. Nicol and J. P. Carbotte, "Comparison of s- and d-wave gap symmetry in nonequilibrium superconductivity," *Phys. Rev. B*, vol. 67, pp. 214506–, June 2003.

[21] R. H. Holm, P. Kennepohl, and E. I. Solomon, "Structural and functional aspects of metal sites in biology," *Chemical Reviews*, vol. 96, no. 7, pp. 2239–2314, 1996. PMID: 11848828.

[22] J. P. Klinman, "Mechanisms whereby mononuclear copper proteins functionalize organic substrates," *Chemical Reviews*, vol. 96, no. 7, pp. 2541–2562, 1996. PMID: 11848836.

[23] E. I. Solomon, U. M. Sundaram, and T. E. Machonkin, "Multicopper oxidases and oxygenases," *Chemical Reviews*, vol. 96, no. 7, pp. 2563–2606, 1996. PMID: 11848837.

[24] S. Binder, *From UV-irradiation to FLASH - Establishing methods for the investigation of properties and function of biological and bioinorganic samples.* PhD thesis, Universität Hamburg, 2009.

[25] S. Herres-Pawlis, S. Binder, A. Eich, R. Haase, B. Schulz, G. Wellenreuther, G. Henkel, M. Rübhausen, and W. Meyer-Klaucke, "Stabilisation of a highly reactive bis(μ-oxo)dicopper(iii) species at room temperature by electronic and steric constraint of an unconventional nitrogen donor ligand," *Chemistry - A European Journal*, vol. 15, no. 35, pp. 8678–8682, 2009.

[26] A. Hoffmann, C. Citek, S. Binder, A. Goos, M. Rübhausen, O. Troeppner, I. Ivanovič-Burmazovič, E. C. Wasinger, T. D. P. Stack, and S. Herres-Pawlis, "Katalytische phenolhydroxylierung mit sauerstoff: Substratvielfalt jenseits der proteinmatrix von tyrosinase," *Angewandte Chemie*, vol. 125, no. 20, pp. 5508–5512, 2013.

[27] B. L. Vallee and R. J. Williams, "Metalloenzymes: the entatic nature of their active sites," *Proceedings of the National Academy of Sciences*, vol. 59, no. 2, pp. 498–505, 1968.

[28] C. Kittel, *Einführung in die Festkörperphysik.* Oldenbourg Verlag München Wien, 2002.

[29] A. J. Millis, "Lattice effects in magnetoresistive manganese perovskites," *Nature*, vol. 392, pp. 147–150, Mar. 1998.

[30] Jin, S. and O'Bryan, H. M. and Tiefel, T. H. and McCormack, M. and Rhodes, W. W., "Large magnetoresistance in polycrystalline La–Y–Ca–Mn–O," *Appl. Phys. Lett.*, vol. 66, pp. 382–384, Jan. 1995.

[31] J. Van Santen and G. Jonker, "Electrical conductivity of ferromagnetic compounds of manganese with perovskite structure," *Physica*, vol. 16, pp. 599–600, 1950.

[32] J. H. Van Vleck, "Theory of the variations in paramagnetic anisotropy among different salts of the iron group," *Phys. Rev.*, vol. 41, pp. 208–215, July 1932.

[33] Ilka Mahns, *Static and Dynamic Properties of Manganites and Cuprates.* PhD thesis, 2009.

[34] M. Abbate, F. M. F. de Groot, J. C. Fuggle, A. Fujimori, O. Strebel, F. Lopez, M. Domke, G. Kaindl, G. A. Sawatzky, M. Takano, Y. Takeda, H. Eisaki, and S. Uchida, "Controlled-valence properties of $La_{1-x}Sr_xFeO_3$ and $La_{1-x}Sr_xMnO_3$ studied by soft-x-ray absorption spectroscopy," *Phys. Rev. B*, vol. 46, pp. 4511–4519, Aug. 1992.

[35] R. G. Burns, *Mineralogical Applications of Crystal Field Theory.* Cambridge University Press, 1993.

[36] Coey, J. M. D. and Viret, M. and von Molnár, S., "Mixed-valence manganites," *Advances in Physics*, vol. 48, pp. 167–293, Mar. 1999.

[37] A. J. Millis, "Condensed-matter physics: Stripes of a different stripe," *Nature*, vol. 392, pp. 438–439, Apr. 1998.

[38] Chen, C. H. and Cheong, S-W., "Commensurate to Incommensurate Charge Ordering and Its Real-Space Images in $La_{0.5}Ca_{0.5}MnO_3$," *Phys. Rev. Lett.*, vol. 76, pp. 4042–4045, May 1996.

[39] Y. Tokura, "Critical features of colossal magnetoresistive manganites," *Reports on Progress in Physics*, vol. 69, no. 3, pp. 797–, 2006.

[40] C. Zener, "Interaction between the d-Shells in the Transition Metals. II. Ferromagnetic Compounds of Manganese with Perovskite Structure," *Phys. Rev.*, vol. 82, pp. 403–405, May 1951.

[41] S. Nahler, *Optical Studies of Ordering Phenomena in Manganese Oxides.* PhD thesis, 2005.

[42] H.A. Kramers, "L'interaction Entre les Atomes Magnétogénes dans un Cristal Paramagnétique," *Physica*, vol. 1, pp. 182–192, 1934.

[43] J. Hubbard, "Electron correlations in narrow energy bands," *Proceedings of the Royal Society of London A: Mathematical, Physical and Engineering Sciences*, vol. 276, no. 1365, pp. 238–257, 1963.

[44] J. Hubbard, "Electron Correlations in Narrow Energy Bands. II. The Degenerate Band Case," *Royal Society of London Proceedings Series A*, vol. 277, pp. 237–259, 1964.

[45] J. Hubbard, "Electron Correlations in Narrow Energy Bands. III. An Improved Solution," *Royal Society of London Proceedings Series A*, vol. 281, pp. 401–419, 1964.

[46] Bednorz, J. G. and Müller, K. A., "Possible high T_c superconductivity in the Ba-La-Cu-O system," *Zeitschrift für Physik B Condensed Matter*, vol. 64, pp. 189–193, June 1986.

[47] H. Onnes, "The resistance of pure mercury at helium temperatures," *Commun. Phys. Lab. Univ. Leiden*, vol. 12, pp. 120–, 1911.

[48] Meissner, W. and Ochsenfeld, R., "Ein neuer Effekt bei Eintritt der Supraleitfähigkeit," *Naturwissenschaften*, vol. 21, pp. 787–788, Nov. 1933.

[49] L. V. Shubnikov, V. I. Khotkevich, Y. D. Shapelev, and Y. N. Ryabinin, "Magnetic properties of superconducting metals and alloys," *Zh. Eksp. Teor. Fiz.*, vol. 7, p. 221, 1937.

[50] M.B., Maple, "High-temperature superconductivity," *Journal of Magnetism and Magnetic Materials*, vol. 177-181, Part 1, pp. 18–30, Jan. 1998.

[51] D. L. Cox and M. B. Maple, “Electronic pairing in exotic superconductors,” *Phys. Today*, vol. 48, pp. 32–40, Feb. 1995.

[52] Hardy, W. N. and Bonn, D. A. and Morgan, D. C. and Liang, Ruixing and Zhang, Kuan, “Precision measurements of the temperature dependence of λ in $YBa_2Cu_3O_{6.95}$: Strong evidence for nodes in the gap function,” *Phys. Rev. Lett.*, vol. 70, pp. 3999–4002, June 1993.

[53] B. Stadlober, G. Krug, R. Nemetschek, R. Hackl, J. L. Cobb, and J. T. Markert, “Is $Nd_{2-x}Ce_xCuO_4$ a High-Temperature Superconductor?,” *Phys. Rev. Lett.*, vol. 74, pp. 4911–4914, June 1995.

[54] D. Manske, I. Eremin, and K. H. Bennemann, “Theory for electron- and hole-doped cuprate superconductors: d -wave symmetry order parameter,” *EPL (Europhysics Letters)*, vol. 53, no. 3, pp. 371–, 2001.

[55] T. Tohyama and S. Maekawa, “Angle-resolved photoemission in high T_c cuprates from theoretical viewpoints,” *Superconductor Science and Technology*, vol. 13, no. 4, pp. R17–, 2000.

[56] D. J. Scalapino, J. Loh, E., and J. E. Hirsch, “d-wave pairing near a spin-density-wave instability,” *Phys. Rev. B*, vol. 34, pp. 8190–8192, Dec. 1986.

[57] D.J., Scalapino, “Antiferromagnetic fluctuations and $d_{x^2-y^2}$-pairing in the cuprates,” *Physica C: Superconductivity*, vol. 235-240, Part 1, pp. 107–112, Dec. 1994.

[58] P. Abbamonte, G. Blumberg, A. Rusydi, A. Gozar, P. G. Evans, T. Siegrist, L. Venema, H. Eisaki, E. D. Isaacs, and G. A. Sawatzky, “Crystallization of charge holes in the spin ladder of $Sr_{14}Cu_{24}O_{41}$,” *Nature*, vol. 431, pp. 1078–1081, Oct. 2004.

[59] E. Wigner, “On the interaction of electrons in metals,” *Phys. Rev.*, vol. 46, pp. 1002–1011, Dec. 1934.

[60] N. D. Drummond, Z. Radnai, J. R. Trail, M. D. Towler, and R. J. Needs, “Diffusion quantum monte carlo study of three-dimensional wigner crystals,” *Phys. Rev. B*, vol. 69, pp. 085116–, Feb. 2004.

[61] B. Tanatar and D. M. Ceperley, “Ground state of the two-dimensional electron gas,” *Phys. Rev. B*, vol. 39, pp. 5005–5016, Mar. 1989.

[62] D. Budelmann, B. Schulz, M. Rübhausen, M. V. Klein, M. S. Williamsen, and P. Guptasarma, “Gaplike Excitations in the Superconducting State of $Bi_2Sr_2CaCu_2O_8$ Studied by Resonant Raman Scattering,” *Phys. Rev. Lett.*, vol. 95, pp. 057003–, July 2005.

[63] D. Budelmann, *Electronic and Magnetic Properties of Pure and Structured Cuprate Superconductors, A Raman Scattering and Ellipsometry Study.* PhD thesis, Institute of Applied Physics, University Hamburg, Germany, (Cuvillier Verlag Göttingen, 2004).

[64] K. Kojima, N. Motoyama, H. Eisaki, and S. Uchida, "The electronic properties of cuprate ladder materials," *Journal of Electron Spectroscopy and Related Phenomena*, vol. 117–118, pp. 237–250, June 2001.

[65] Rusydi, A. and Ku, W. and Schulz, B. and Rauer, R. and Mahns, I. and Qi, D. and Gao, X. and Wee, A. T. S. and Abbamonte, P. and Eisaki, H. and Fujimaki, Y. and Uchida, S. and Rübhausen, M., "Experimental observation of the crystallization of a paired holon state," *Phys. Rev. Lett.*, vol. 105, pp. 026402–, July 2010.

[66] Rusydi, A. and Abbamonte, P. and Eisaki, H. and Fujimaki, Y. and Smadici, S. and Motoyama, N. and Uchida, S. and Kim, Y.-J. and Rübhausen, M. and Sawatzky, G. A., "Strain Amplification of the $4k_F$ Chain Instability in $Sr_{14}Cu_{24}O_{41}$," *Phys. Rev. Lett.*, vol. 100, pp. 036403–, Jan. 2008.

[67] M. Uehara, N. Motoyama, M. Matsuda, H. Eisaki, and J. Akimitsu, "Superconductivity and magnetism in ladder and chain compounds," in *Frontiers in Magnetic Materials* (A. Narlikar, ed.), pp. 573–609–, Springer Berlin Heidelberg, 2005.

[68] A. Goos, "Zeitaufgeloeste Ramanspektroskopie an $\mathrm{La}_{1-x}\mathrm{Ca}_x\mathrm{MnO}_3$," Master's thesis, Institute of Applied Physics, University of Hamburg, Germany, 2008.

[69] R. P. Saichu, "Zeitaufgelöste Raman-Spektroskopie an $\mathrm{Bi_2Sr_2CaCu_2O_8}$," Master's thesis, Institute of Applied Physics, University Hamburg, 2008.

[70] Spectra Physics, *Millenia Pro s-Series, Diode Pumped, CW Visible Laser System Manual*, Part Number 0000-320 A, Rev. B. (2006).

[71] A. Weiner, *Ultrafast Optics.* Wiley, 2008.

[72] Spectra-Physics, *Tsunami, Mode-locked Ti:sapphire Laser Manual*, Part Number 0000-232A, Rev. D. (2002).

[73] Spectra Physics, *GWU-FHG, Flexible Harmonic Generator Manual*, Part Number 0000-279A, Rev. A. (2005).

[74] B. Schulz, J. Bäckström, D. Budelmann, R. Maeser, M. Rübhausen, M. V. Klein, E. Schoeffel, A. Mihill, and S. Yoon, "Fully reflective deep ultraviolet to near infrared spectrometer and entrance optics for resonance Raman spectroscopy," *Rev. Sci. Instr.*, vol. 76, p. 073107, 2005.

[75] B. Schulz, "Optische Untersuchungen chiraler Anregungen bei Kuprathochtemperatursupraleitern," Master's thesis, Institute of Applied Physics, University Hamburg, (2001).

[76] I. Mahns, "Optische Specktroskopie und inelastische Lichtstreuung an multiferroischem $TbMnO_3$," Master's thesis, Institute of Applied Physics, University Hamburg, (2005).

[77] J. Rossbach, "A VUV free electron laser at the TESLA test facility at DESY," *Nuclear Instruments and Methods in Physics Research Section A: Accelerators, Spectrometers, Detectors and Associated Equipment*, vol. 375, pp. 269 – 273, 1996. Proceedings of the 17th International Free Electron Laser Conference.

[78] H. Weise, "The tesla test facility (ttf) linac-a status report," in *Particle Accelerator Conference, 1995., Proceedings of the 1995*, vol. 1, pp. 677–679 vol.1, 1995.

[79] R. Bonifacio, C. Pellegrini, and L. Narducci, "Collective instabilities and high-gain regime in a free electron laser," *Optics Communications*, vol. 50, no. 6, pp. 373 – 378, 1984.

[80] J. Andruszkow, B. Aune, V. Ayvazyan, N. Baboi, R. Bakker, V. Balakin, D. Barni, A. Bazhan, M. Bernard, A. Bosotti, J. C. Bourdon, W. Brefeld, R. Brinkmann, S. Buhler, J.-P. Carneiro, M. Castellano, P. Castro, L. Catani, S. Chel, Y. Cho, S. Choroba, E. R. Colby, W. Decking, P. Den Hartog, M. Desmons, M. Dohlus, D. Edwards, H. T. Edwards, B. Faatz, J. Feldhaus, M. Ferrario, M. J. Fitch, K. Flöttmann, M. Fouaidy, A. Gamp, T. Garvey, C. Gerth, M. Geitz, E. Gluskin, V. Gretchko, U. Hahn, W. H. Hartung, D. Hubert, M. Hüning, R. Ischebek, M. Jablonka, J. M. Joly, M. Juillard, T. Junquera, P. Jurkiewicz, A. Kabel, J. Kahl, H. Kaiser, T. Kamps, V. V. Katelev, J. L. Kirchgessner, M. Körfer, L. Kravchuk, G. Kreps, J. Krzywinski, T. Lokajczyk, R. Lange, B. Leblond, M. Leenen, J. Lesrel, M. Liepe, A. Liero, T. Limberg, R. Lorenz, L. H. Hua, L. F. Hai, C. Magne, M. Maslov, G. Materlik, A. Matheisen, J. Menzel, P. Michelato, W.-D. Möller, A. Mosnier, U.-C. Müller, O. Napoly, A. Novokhatski, M. Omeich, H. S. Padamsee, C. Pagani, F. Peters, B. Petersen, P. Pierini, J. Pflüger, P. Piot, B. Phung Ngoc, L. Plucinski, D. Proch, K. Rehlich, S. Reiche, D. Reschke, I. Reyzl, J. Rosenzweig, J. Rossbach, S. Roth, E. L. Saldin, W. Sandner, Z. Sanok, H. Schlarb, G. Schmidt, P. Schmüser, J. R. Schneider, E. A. Schneidmiller, H.-J. Schreiber, S. Schreiber, P. Schütt, J. Sekutowicz, L. Serafini, D. Sertore, S. Setzer, S. Simrock, B. Sonntag, B. Sparr, F. Stephan, V. A. Sytchev, S. Tazzari, F. Tazzioli, M. Tigner, M. Timm, M. Tonutti, E. Trakhtenberg, R. Treusch, D. Trines, V. Verzilov, T. Vielitz, V. Vogel, G. v. Walter, R. Wanzenberg, T. Weiland,

H. Weise, J. Weisend, M. Wendt, M. Werner, M. M. White, I. Will, S. Wolff, M. V. Yurkov, K. Zapfe, P. Zhogolev, and F. Zhou, "First observation of self-amplified spontaneous emission in a free-electron laser at 109 nm wavelength," *Phys. Rev. Lett.*, vol. 85, pp. 3825–3829, Oct. 2000.

[81] *SASE FEL at the TESLA Facility, Phase 2*, June 2002.

[82] M. Wellhöfer, M. Martins, W. Wurth, A. A. Sorokin, and M. Richter, "Performance of the monochromator beamline at flash," *Journal of Optics A: Pure and Applied Optics*, vol. 9, no. 7, pp. 749–, 2007.

[83] M. Martins, M. Wellhofer, J. T. Hoeft, W. Wurth, J. Feldhaus, and R. Follath, "Monochromator beamline for flash," *Review of Scientific Instruments*, vol. 77, no. 11, p. 115108, 2006.

[84] R. Reininger, "Parameters for the refocusing optics," tech. rep., Scientific Answers & Solutions, LLC, 2006.

[85] "Description of the VUV-Raman spectrometer," September 2006.

[86] C. Palmer, *Diffraction Grating Handbook*. Newport Corporation, 6th ed., 2005.

[87] X. Ottenwaelder, D. J. Rudd, M. C. Corbett, K. O. Hodgson, B. Hedman, and T. D. P. Stack, "Reversible o-o bond cleavage in copper-dioxygen isomers: impact of anion basicity," *Journal of the American Chemical Society*, vol. 128, pp. 9268–9269, July 2006.

[88] A. Jesser, M. Rohrmüller, W. G. Schmidt, and S. Herres-Pawlis, "Geometrical and optical benchmarking of copper guanidine-quinoline complexes: Insights from td-dft and many-body perturbation theory," *Journal of Computational Chemistry*, vol. 35, no. 1, pp. 1–17, 2014.

[89] S. Naler, M. Rübhausen, S. Yoon, S. L. Cooper, K. H. Kim, and S. W. Cheong, "Lattice dynamics and charge ordering in $La_{1-x}Ca_xMnO_3$ $(0.45 < x < 0.76)$," *Phys. Rev. B*, vol. 65, p. 092401, Jan 2002.

[90] R. Krüger, B. Schulz, S. Naler, R. Rauer, D. Budelmann, J. Bäckström, K. H. Kim, S.-W. Cheong, V. Perebeinos, and M. Rübhausen, "Orbital ordering in $\mathrm{LaMnO_3}$ investigated by resonance Raman spectroscopy," *Phys. Rev. Lett.*, vol. 92, p. 097203, 2004.

[91] A. Kowalczyk, J. Baszynski, A. Szajek, A. Slebarski, and T. Tolinski, "Electronic structure of doped $LaMnO_3$ perovskite studied by x-ray photoemission spectroscopy," *Journal of Physics: Condensed Matter*, vol. 13, no. 23, p. 5519, 2001.

[92] L. D. Landau, “Über die Bewegung der Elektronen in Kristalgitter,” *Phys. Z. Sowjetunion*, pp. 644–645, 1933.

[93] Y.-F. Yang and K. Held, “Localization of strongly correlated electrons as jahn-teller polarons in manganites,” *Phys. Rev. B*, vol. 76, p. 212401, Dec 2007.

[94] G.-m. Zhao, D. J. Kang, W. Prellier, M. Rajeswari, H. Keller, T. Venkatesan, and R. L. Greene, “Strong oxygen-isotope effect on the intrinsic resistivity in the ferromagnetic state of manganites,” *Phys. Rev. B*, vol. 63, p. 060402, Dec 2000.

[95] V. Cataudella, G. De Filippis, and G. Iadonisi, “Coexistence of large and small polarons in manganites,” *Phys. Rev. B*, vol. 63, p. 052406, Jan 2001.

[96] A. J. Lotka, *Elements of Physical Biology.* Williams and Wilkins Company, 1925.

[97] C. Jost, G. Devulder, J. A. Vucetich, R. O. Peterson, and R. Arditi, “The wolves of isle royale display scale-invariant satiation and ratio-dependent predation on moose,” *Journal of Animal Ecology*, vol. 74, no. 5, pp. 809–816, 2005.

[98] C. H. Feinstein, ed., *Socialism, Capitalism and Economic Growth Essays Presented to Maurice Dobb.* Cambridge University Press, 1975.

[99] M. Desai and P. Ormerod, “Richard Goodwin: a Short Appreciation,” *The Economic Journal*, vol. 108, no. 450, pp. 1431–1435, 1998.

[100] D. Scalapino, “The case for $d_{x^2-y^2}$ pairing in the cuprate superconductors,” *Physics Reports*, vol. 250, pp. 329–365, Jan. 1995.

[101] C. J. Stevens, D. Smith, C. Chen, J. F. Ryan, B. Podobnik, D. Mihailovic, G. A. Wagner, and J. E. Evetts, “Evidence for Two-Component High-Temperature Superconductivity in the Femtosecond Optical Response of $YBa_2Cu_3O_{7-\delta}$,” *Phys. Rev. Lett.*, vol. 78, pp. 2212–2215, Mar 1997.

[102] A. Bock, *Makro- und Mikro-Raman Spektroskopie an $YBa_2Cu_3O_7$ Filmen und Mikrobrücken.* PhD thesis, Institute of Applied Physics, University Hamburg, Germany, (Shaker Verlag, 1993).

[103] R. A. Kaindl, M. A. Carnahan, D. S. Chemla, S. Oh, and J. N. Eckstein, “Dynamics of Cooper pair formation in $Bi_2Sr_2CaCu_2O_{8+\delta}$,” *Phys. Rev. B*, vol. 72, p. 060510, Aug 2005.

[104] L. Capogna, B. Fauqué, Y. Sidis, C. Ulrich, P. Bourges, S. Pailhès, A. Ivanov, J. L. Tallon, B. Liang, C. T. Lin, A. I. Rykov, and B. Keimer, “Odd and even magnetic resonant modes in highly overdoped $\mathrm{Bi_2Sr_2CaCu_2O_{8+\delta}}$,” *Phys. Rev. B*, vol. 75, p. 060502, Feb. 2007.

[105] J. A. Slezak, J. Lee, M. Wang, K. McElroy, K. Fujita, B. M. Andersen, P. J. Hirschfeld, H. Eisaki, S. Uchida, and J. C. Davis, "From the Cover: Imaging the impact on cuprate superconductivity of varying the interatomic distances within individual crystal unit cells," *PNAS*, vol. 105, pp. 3203–3208, Feb. 2008.

[106] A. Rusydi, M. Berciu, P. Abbamonte, S. Smadici, H. Eisaki, Y. Fujimaki, S. Uchida, M. Rübhausen, and G. A. Sawatzky, "Relationship between hole density and charge-ordering wave vector in $\mathrm{Sr}_{14-x}\mathrm{Ca}_x\mathrm{Cu}_{24}\mathrm{O}_{41}$," *Phys. Rev. B*, vol. 75, p. 104510, Mar 2007.

[107] N. Motoyama, T. Osafune, T. Kakeshita, H. Eisaki, and S. Uchida, "Effect of ca substitution and pressure on the transport and magnetic properties of $\mathrm{sr}_{14}\mathrm{cu}_{24}\mathrm{o}_{41}$ with doped two-leg cu-o ladders," *Phys. Rev. B*, vol. 55, pp. R3386–R3389, Feb 1997.

[108] M. B. J. Meinders, J. van den Brink, J. Lorenzana, and G. A. Sawatzky, "Atomic screening and intersite coulomb repulsion in strongly correlated systems," *Phys. Rev. B*, vol. 52, pp. 2484–2495, Jul 1995.

[109] J. Zaanen, G. A. Sawatzky, and J. W. Allen, "Band gaps and electronic structure of transition-metal compounds," *Phys. Rev. Lett.*, vol. 55, pp. 418–421, Jul 1985.

[110] M. B. J. Meinders, H. Eskes, and G. A. Sawatzky, "Spectral-weight transfer: Breakdown of low-energy-scale sum rules in correlated systems," *Phys. Rev. B*, vol. 48, pp. 3916–3926, Aug 1993.

[111] M. G. Cottam and D. J. Lockwood, "One-magnon raman scattering in a $S=5/2$ antiferromagnet," *Phys. Rev. B*, vol. 31, pp. 641–643, Jan 1985.

[112] M. L. Tacon, G. Ghiringhelli, J. Chaloupka, M. M. Sala, V. Hinkov, M. W. Haverkort, M. Minola, M. Bakr, K. J. Zhou, S. Blanco-Canosa, C. Monney, Y. T. Song, G. L. Sun, C. T. Lin, G. M. D. Luca, M. Salluzzo, G. Khaliullin, T. Schmitt, L. Braicovich, and B. Keimer, "Intense paramagnon excitations in a large family of high-temperature superconductors," *Nature Physics*, vol. 7, no. 9, pp. 725–730, 2011.

[113] T. F. A. Müller, V. Anisimov, T. M. Rice, I. Dasgupta, and T. Saha-Dasgupta, "Electronic structure of ladder cuprates," *Phys. Rev. B*, vol. 57, pp. R12655–R12658, May 1998.

[114] R. S. Eccleston, M. Uehara, J. Akimitsu, H. Eisaki, N. Motoyama, and S.-i. Uchida, "Spin Dynamics of the Spin-Ladder Dimer-Chain Material $Sr_{14}Cu_{24}O_{41}$," *Phys. Rev. Lett.*, vol. 81, pp. 1702–1705, Aug 1998.

A. Derivation of a “classical” propagator

In this section a brief overview of the methods and tools that are used to derive propagators (Green’s functions) is given.

A.1. Fourier transformation

Every periodic function $f(t)$ can be written as a superposition of sin and cos functions. In complex notation this yields

$$f(t) = \sum_{n=-\infty}^{\infty} c_n \exp\left(in\frac{2\pi}{T}t\right) \tag{A.1}$$

withe T as the period of the function $f(t)$ and the coefficient c_n:

$$c_n = \frac{1}{T}\int\limits_{-T/2}^{T/2} f(t)\exp\left(-i\frac{2\pi}{T}nt\right)dt \tag{A.2}$$

For $T \mapsto \infty$ and with $\frac{2\pi}{T} = \Delta\omega$ and $\frac{2\pi n}{T} = \omega$ one finds:

$$\begin{aligned}
f(t) &= \sum_{n=-\infty}^{\infty} c_n \exp\left(in\frac{2\pi}{T}t\right) && \text{(A.3)}\\
&= \frac{T}{2\pi}\sum_{n=-\infty}^{\infty} \frac{2\pi}{T}c_n\left(\frac{2\pi n}{T}\right)\exp\left(i\frac{2\pi}{T}nt\right) && \text{(A.4)}\\
&= \frac{T}{2\pi}\sum_{n=-\infty}^{\infty} \Delta\omega c_n(\omega)\exp\left(i\omega t\right) && \text{(A.5)}\\
&\overset{T\mapsto\infty}{=} \frac{T}{2\pi}\int\limits_{-\infty}^{\infty} d\omega\; c(\omega)\exp\left(i\omega t\right) && \text{(A.6)}\\
&\overset{T\mapsto\infty}{=} \int\limits_{-\infty}^{\infty} d\omega\; \frac{1}{2\pi}\tilde{f}(\omega)\exp(i\omega t). && \text{(A.7)}
\end{aligned}$$

$\tilde{f}(\omega)$ is called the Fourier transformed function to $f(t)$. After further evaluation of equation A.7 one finds

$$\tilde{f}(\omega) = T \cdot c(\omega) = \lim_{T \mapsto \infty} \int\limits_{-T/2}^{T/2} dt\ f(t) \exp\left(-in\frac{2\pi}{T}t\right) = \int\limits_{-\infty}^{\infty} dt\ f(t) \exp(-i\omega t), \quad \text{(A.8)}$$

and the back transformation

$$f(t) = \int\limits_{-\infty}^{\infty} d\omega\ \frac{1}{2\pi}\tilde{f}(\omega) \exp(i\omega t). \quad \text{(A.9)}$$

Equation A.8 and A.9 are not unitary. To make these equations unitary the factor $\frac{1}{2\pi}$ of equation A.9 is often splinted between the Fourier transformed function

$$\tilde{f}(\omega) = \frac{1}{\sqrt{2\pi}} \int\limits_{-\infty}^{\infty} dt\ f(t) \exp(-i\omega t), \quad \text{(A.10)}$$

and the inverse Fourier transformed function

$$\tilde{\tilde{f}}(t) = f(t) = \frac{1}{\sqrt{2\pi}} \int\limits_{-\infty}^{\infty} d\omega\ \tilde{f}(\omega) \exp(i\omega t). \quad \text{(A.11)}$$

Both notations are equal.

A.2. Greens functions

Greens functions are powerful tools to solve inhomogeneous differential equations of the kind

$$D_t f(t) = h(t), \quad \text{(A.12)}$$

with D_t as any linear differential operator. In physics this is a common problem, for example the harmonic oscillator with an external force.

To solve this kind differential equations it is necessary to calculate the solutions of the homogeneous equation and to find one solution of the inhomogeneous equation. This yields to the global solution $f(t) = f_{hom}(t) + f_{inhom}$. f_{hom} is the solution to the homogeneous equation $D_t f(t) = 0$. To find a special solution to the inhomogeneous equation $D_t f(t) = h(t)$ it is useful to first evaluate a δ-function as inhomogeneity.

$$D_t G(t, t') = \delta(t - t') \quad \text{(A.13)}$$

t' is an arbitrarily coordinate and $G(t,t')$ is a function that solves this equation. If equation A.13 is multiplied with $h(t')$ and both sides are integrated over t' it is easy to find:

$$D_t G(t,t')h(t') = \delta(t-t')h(t') \tag{A.14}$$

$$\int_{-\infty}^{\infty} dt'\ D_t G(t,t')h(t') = \int_{-\infty}^{\infty} dt'\ \delta(t-t')h(t') \tag{A.15}$$

The evaluation of the right side of equation A.15 is trivial and yields $h(t)$. If the integration and the differentiation are permuted on the left side of equation A.15 one obtains

$$D_t \int_{-\infty}^{\infty} dt'\ G(t,t')h(t') = h(t). \tag{A.16}$$

Now a solution can directly be read of the inhomogeneous differential equation A.12.

$$f_{inhom} = \int_{-\infty}^{\infty} dt'\ G(t,t')h(t') \tag{A.17}$$

f_{inhom} is the convolution of the function $G(t,t')$ an the inhomogeneity $h(t')$. G(t,t') is known as the **Greens function** of the related linear differential equation.

Example: How to find the Greens function

Let a linear differential equation be considered of the kind:

$$\left(a_0 + a_1 \frac{d}{dt}\right) f(t) = c \tag{A.18}$$

Here, c is an arbitrary constant. This is a first order linear differential equation, but the procedure is analog for higher orders. To solve such an equation it is useful to first evaluate an equation of the kind:

$$\left(a_0 + a_1 \frac{d}{dt}\right) G(t,t') = \delta(t-t') \tag{A.19}$$

This equation can be evaluated in an elegant manner by using the Fourier Transformation. According to equation A.9 $G(t,t')$ can be written as

$$G(t,t') = \int_{-\infty}^{\infty} d\omega \frac{1}{2\pi} \tilde{G}(\omega) \exp(i\omega(t-t')). \tag{A.20}$$

The δ-function can also be written as the inverse Fourier-transform. The Fourier transformed of the δ-function is easy to obtain by solving the integral:

$$\tilde{\delta}(\omega) = \int\limits_{-\infty}^{\infty} dt' \delta(t-t') \exp(-i\omega(t-t')) = 1 \tag{A.21}$$

Thus we find:

$$\left(a_0 + a_1 \frac{d}{dt}\right) \int\limits_{-\infty}^{\infty} d\omega \frac{1}{2\pi} \tilde{G}(\omega) \exp(i\omega(t-t')) = \int\limits_{-\infty}^{\infty} d\omega \frac{1}{2\pi} 1 \ \exp(i\omega(t-t')) \tag{A.22}$$

By permuting the differentiation and the integration we get

$$\int\limits_{-\infty}^{\infty} d\omega \ \frac{1}{2\pi}(a_0 + i\omega a_1)\tilde{G}(\omega) \exp(i\omega(t-t')) = \int\limits_{-\infty}^{\infty} d\omega \ \frac{1}{2\pi} \exp(i\omega(t-t')) \tag{A.23}$$

By comparing the integrates it is easy to see that

$$\tilde{G}(\omega) = \frac{1}{a_0 + i\omega a_1}. \tag{A.24}$$

Now the Greens-Function can back transform:

$$G(t,t') = \int\limits_{-\infty}^{\infty} d\omega \ \frac{1}{2\pi} \tilde{G}(\omega) \exp(i\omega(t-t')) \tag{A.25}$$

$$= \frac{1}{a_1} \int\limits_{-\infty}^{\infty} d\omega \ \frac{1}{2\pi i} \frac{\exp(i\omega(t-t'))}{\omega - \frac{a_0}{a_1} i}. \tag{A.26}$$

To evaluate the integral in equation A.26 the expression for the unit step function $\Theta(t)$ was used.

$$\int\limits_{-\infty}^{\infty} d\omega \ \frac{1}{2\pi i} \frac{\exp(i\omega t)}{\omega - ix} = \Theta(t) \exp(-xt) \tag{A.27}$$

This yields the Greens function of equation A.19:

$$G(t,t') = \frac{1}{a_1} \Theta(t-t') \exp\left(-\frac{a_0}{a_1}(t-t')\right) \tag{A.28}$$

This is also the homogeneous solution of A.19 multiplied with a unit step function. The unit step function denotes, that the system reacts after an external perturbation is applied. The inhomugenius solution f_{inhom} is easy obtainable by evaluation of

A.17. This yields to:

$$\begin{aligned} f_{inhom} &= \int\limits_{-\infty}^{\infty} dt' \frac{1}{a_1} \Theta(t-t') \exp\left(-\frac{a_0}{a_1}(t-t')\right) \cdot c && \text{(A.29)} \\ &= \int\limits_{-\infty}^{t} dt' \frac{c}{a_1} \exp\left(-\frac{a_0}{a_1}(t-t')\right) && \text{(A.30)} \\ &= \left[\frac{c}{a_1}\frac{a_1}{a_0} \exp\left(-\frac{a_0}{a_1}(t-t')\right)\right]_{-\infty}^{t} && \text{(A.31)} \\ &= \frac{c}{a_0} && \text{(A.32)} \end{aligned}$$

As result we get (with t'=0):

$$f(t) = f_{hom} + f_{inhom} = \frac{1}{a_1} \exp\left(-\frac{a_0}{a_1}t\right) + \frac{c}{a_0} \tag{A.33}$$

B. The *Tsunami ps 10W Pump*

The following table shows the achieved power and pulse width with the 15 ps option of the “Tsunami” Ti:sapphire laser. Also the achieved output power in the frequency doubled (2ω) and frequency tripled (3ω) beam is shown. The power of the pump laser was set to 8 Watt.

λ [nm]	$P_{Tsunami}$ [W]	P_{ω} [mW]	$P_{2\omega}$ [mW]	$P_{3\omega}$ [mW]	τ_{ac} [ps]
718,13	1,97	73	44,0	1,00	13,6
723,18	2,00	430	54,3	4,26	14,0
727,97	2,08	688	57,2	6,11	15,0
733,01	2,15	970	60,1	11,80	15,6
738,04	2,19	1130	65,0	14,40	14,8
742,32	2,20	1200	64,4	14,00	15,0
748,35	2,33	1120	74,1	12,30	15,8
753,13	2,32	1260	70,8	11,80	14,0
763,16	2,38	1390	63,0	15,00	15,0
773,18	2,34	1400	57,0	9,50	16,0
783,19	2,30	1310	67,1	5,80	17,0
792,68	2,20	995	57,3	4,15	17,0

Table B.1.: Power characteristic of the used laser system for time resolved Raman scattering. The pump power was 8 Watt and the “15 ps option” was used.

C. Technical drawings of the VUV Raman experiment at FLASH

In this chapter the most important technical drawings and three dimensional CAD-pictures of the VUV Raman setup at FLASH are shown. The drawings have been generated by BESTEC GmbH if not denoted otherwise.

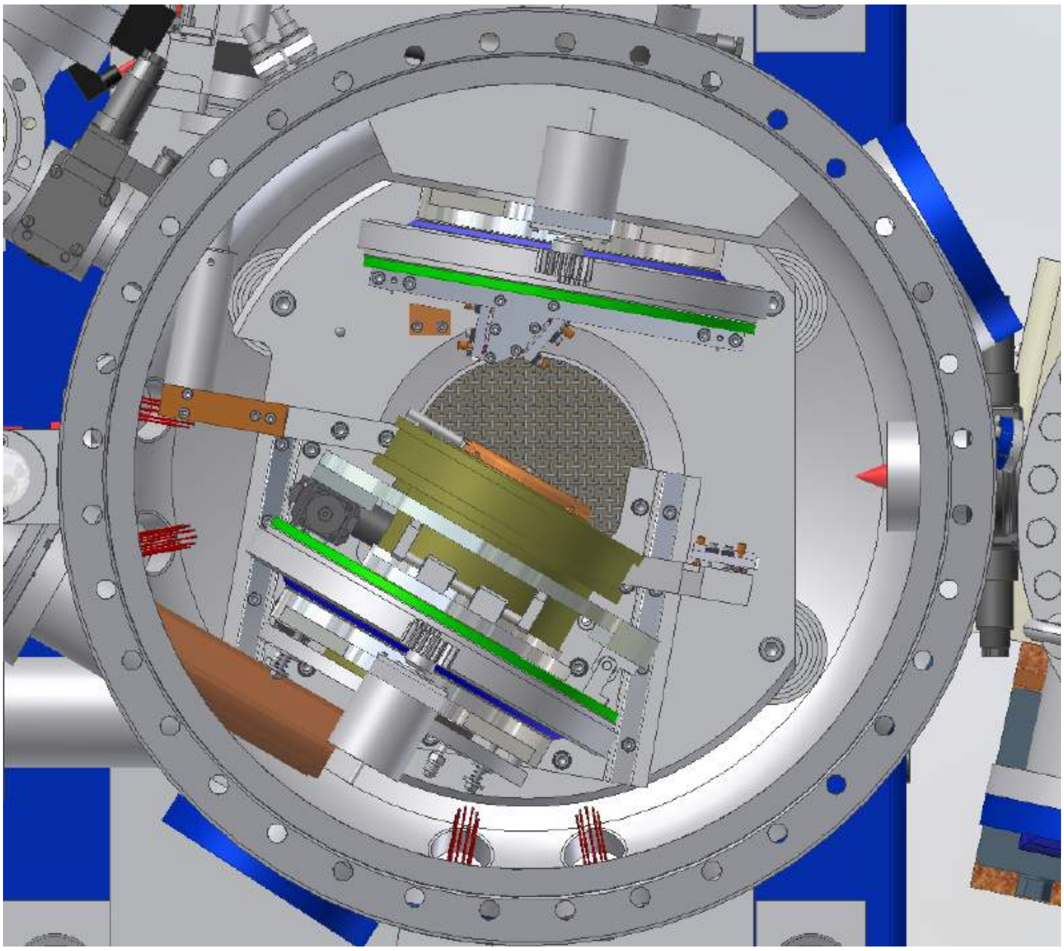

Figure C.1.: Top view CAD drawing of the sample chamber. The FEL beam enters at the right side (denoted by the red cone). The sampleholder is located in a goniometer (dark yellow) in the center of the chamber. The opening to the spectrometer is at the top.

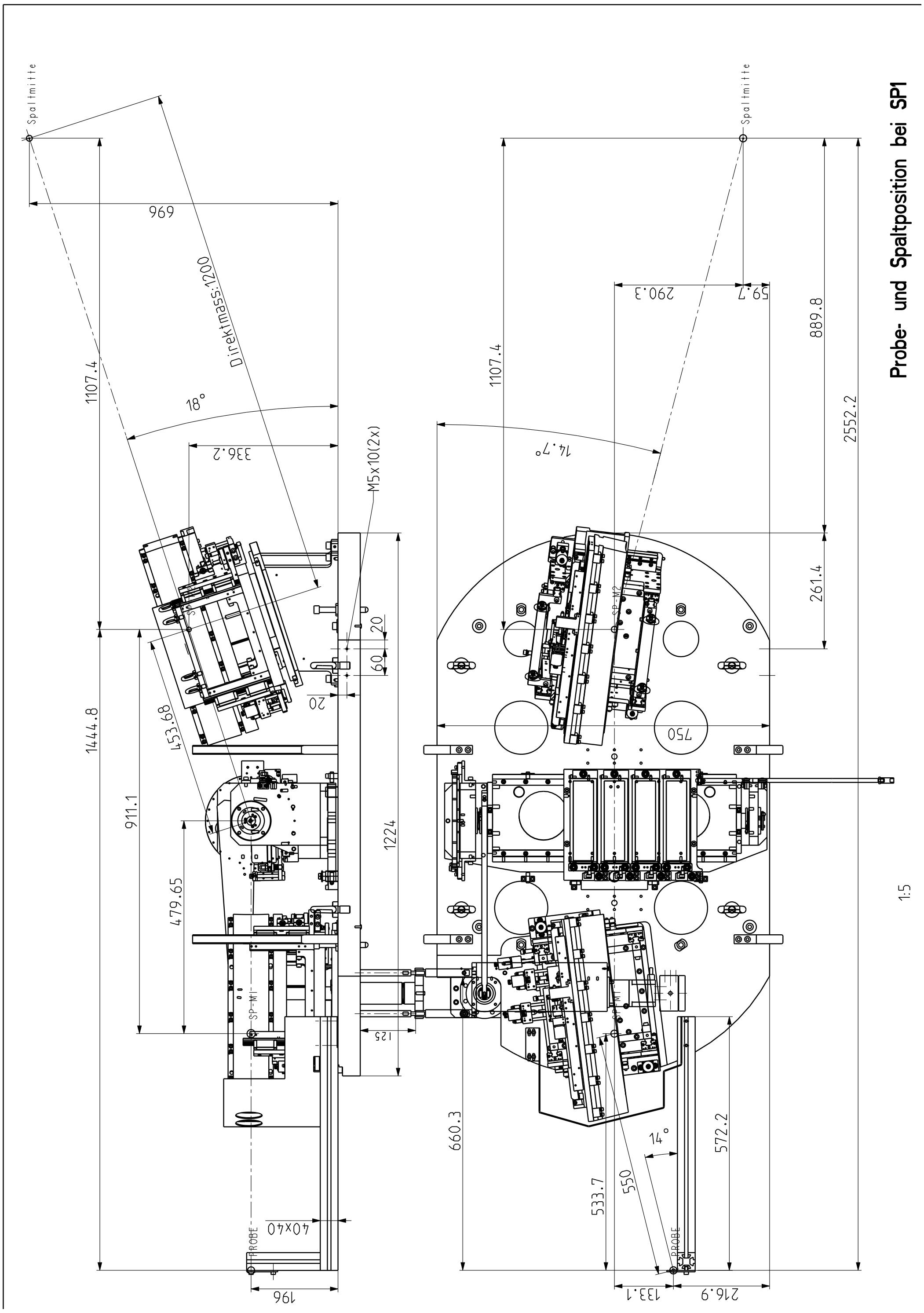

Figure C.2.: Technical drawing of the first monochromator stage (left: side view, right: top view).

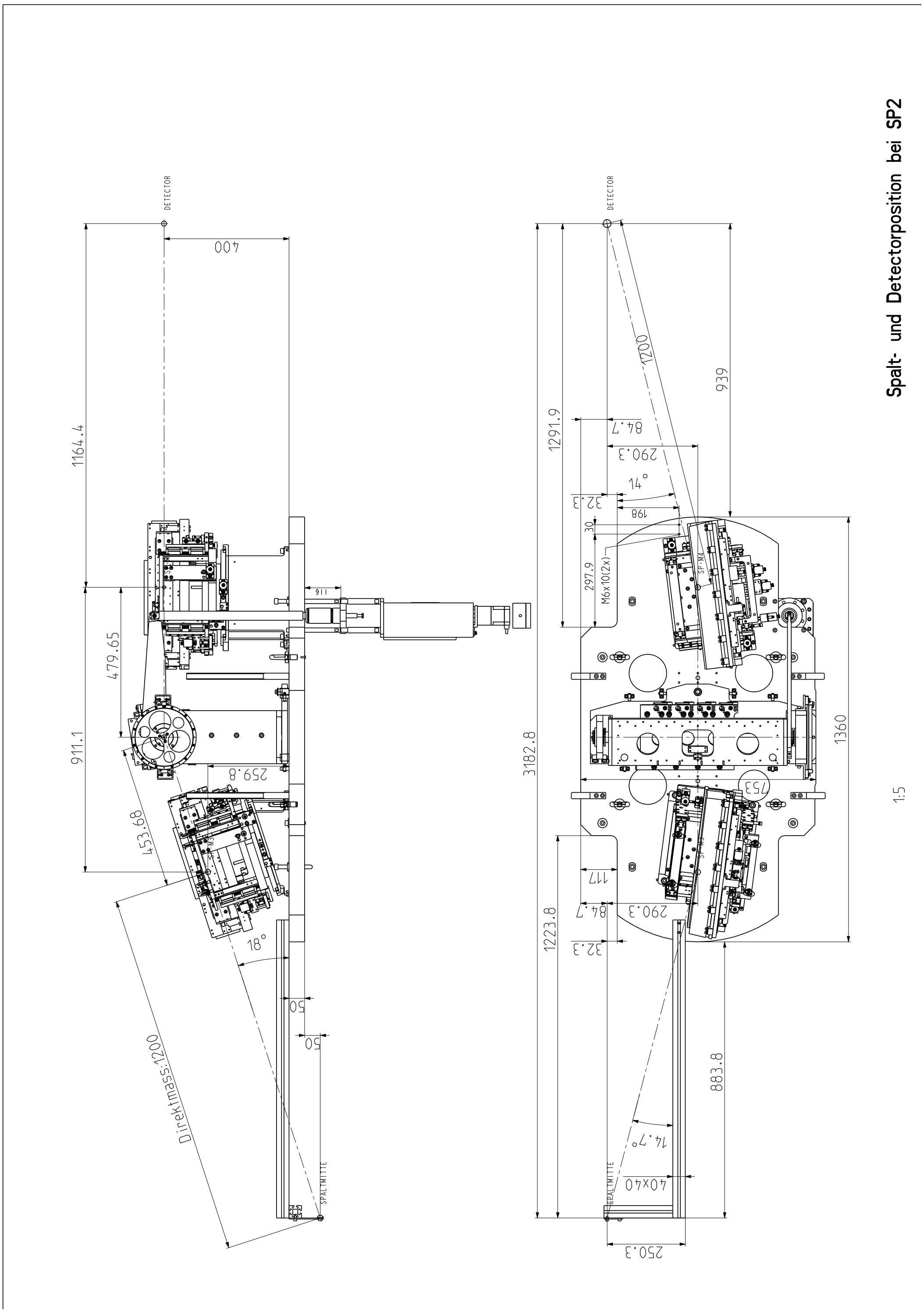

Figure C.3.: Technical drawing of the second monochromator stage (left: side view, right: top view).

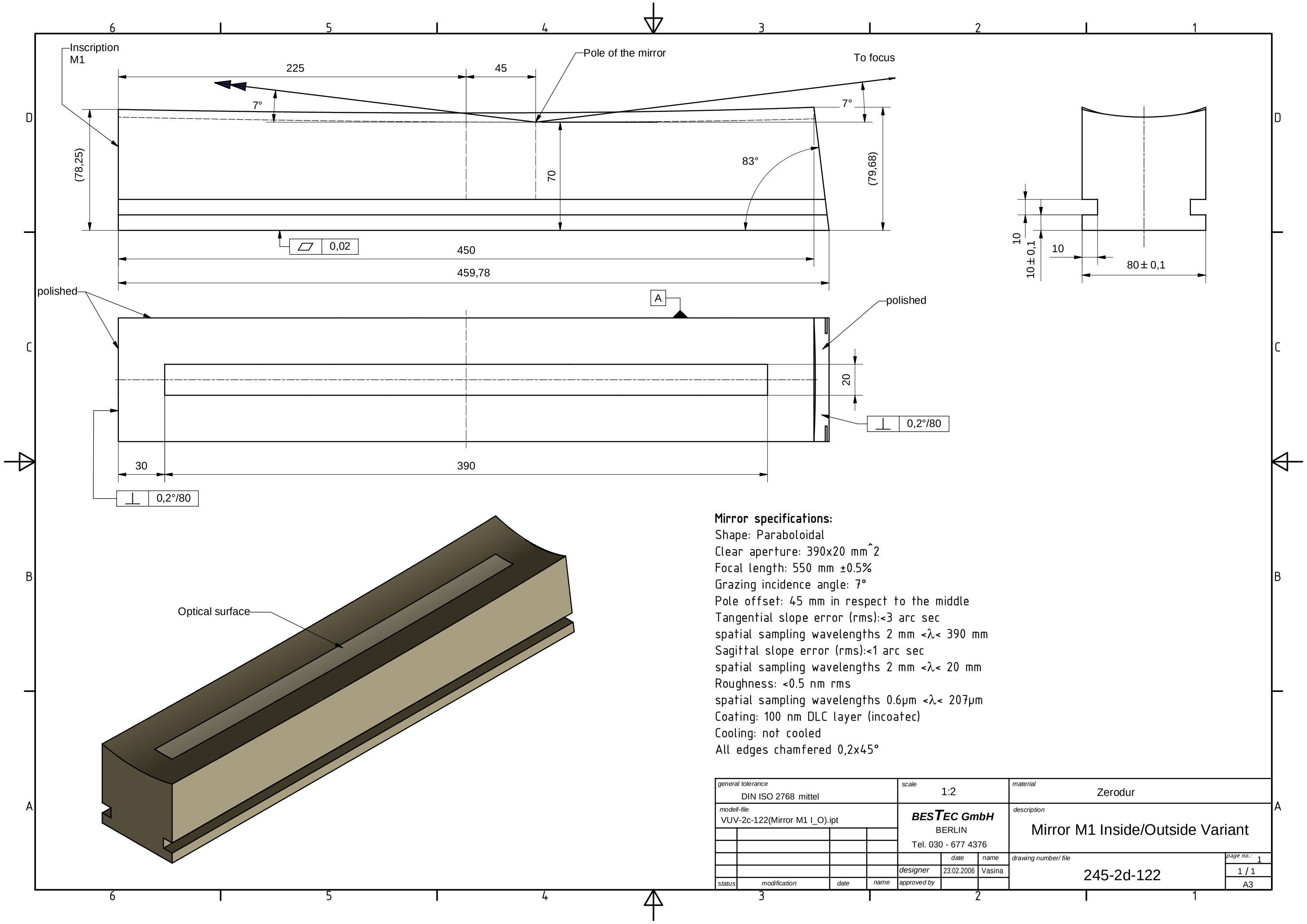

Mirror specifications:
Shape: Paraboloidal
Clear aperture: 390x20 mm^2
Focal length: 550 mm ±0.5%
Grazing incidence angle: 7°
Pole offset: 45 mm in respect to the middle
Tangential slope error (rms):<3 arc sec
spatial sampling wavelengths 2 mm <λ< 390 mm
Sagittal slope error (rms):<1 arc sec
spatial sampling wavelengths 2 mm <λ< 20 mm
Roughness: <0.5 nm rms
spatial sampling wavelengths 0.6μm <λ< 207μm
Coating: 100 nm DLC layer (incoatec)
Cooling: not cooled
All edges chamfered 0,2x45°

Figure C.4.: Technical drawing of the M1 mirror.

D. Alignment pictures of the VUV Raman spectrometer

In this chapter some exemplary pictures of the alignment are given.

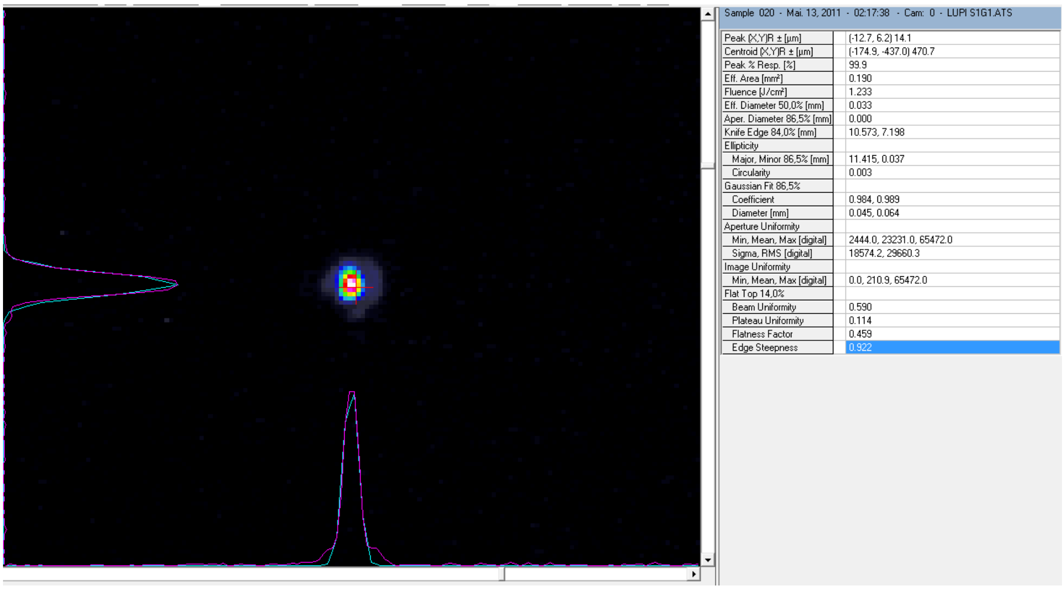

Sample 020 - Mai. 13, 2011 - 02:17:38 - Cam: 0 - LUPI S1G1.ATS

Peak (X,Y)R ± [µm]	(-12.7, 6.2) 14.1
Centroid (X,Y)R ± [µm]	(-174.9, -437.0) 470.7
Peak % Resp. [%]	99.9
Eff. Area [mm^2]	0.190
Fluence [J/cm^2]	1.233
Eff. Diameter 50,0% [mm]	0.033
Aper. Diameter 86,5% [mm]	0.000
Knife Edge 84,0% [mm]	10.573, 7.198
Ellipticity	
Major, Minor 86,5% [mm]	11.415, 0.037
Circularity	0.003
Gaussian Fit 86,5%	
Coefficient	0.984, 0.989
Diameter [mm]	0.045, 0.064
Aperture Uniformity	
Min, Mean, Max [digital]	2444.0, 23231.0, 65472.0
Sigma, RMS [digital]	18574.2, 29660.3
Image Uniformity	
Min, Mean, Max [digital]	0.0, 210.9, 65472.0
Flat Top 14,0%	
Beam Uniformity	0.590
Plateau Uniformity	0.114
Flatness Factor	0.459
Edge Steepness	0.922

Figure D.1.: Spot formation of the LUPI beam over the S1G1 grating at the focal point of the M2 mirror. Screenshot taken from the Beamview analyser software version 4.2.2. The spot size (effective diameter 50%) is 33 μm.

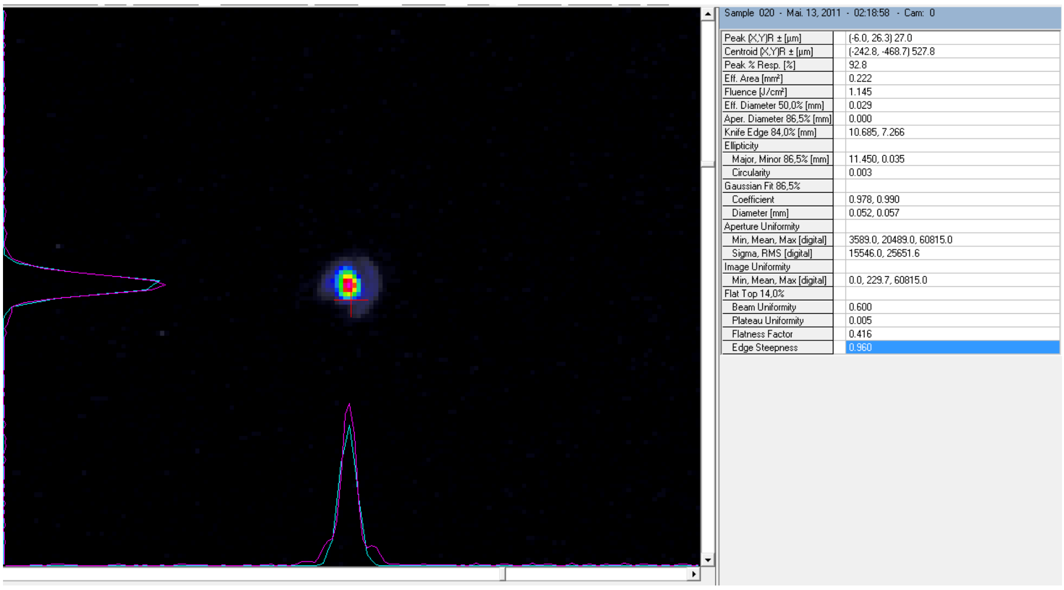

Sample 020 - Mai. 13, 2011 - 02:18:58 - Cam: 0

Peak (X,Y)R ± [µm]	(-6.0, 26.3) 27.0
Centroid (X,Y)R ± [µm]	(-242.8, -468.7) 527.8
Peak % Resp. [%]	92.8
Eff. Area [mm²]	0.222
Fluence [J/cm²]	1.145
Eff. Diameter 50,0% [mm]	0.029
Aper. Diameter 86,5% [mm]	0.000
Knife Edge 84,0% [mm]	10.685, 7.266
Ellipticity	
Major, Minor 86,5% [mm]	11.450, 0.035
Circularity	0.003
Gaussian Fit 86,5%	
Coefficient	0.978, 0.990
Diameter [mm]	0.052, 0.057
Aperture Uniformity	
Min, Mean, Max [digital]	3589.0, 20489.0, 60815.0
Sigma, RMS [digital]	15546.0, 25651.6
Image Uniformity	
Min, Mean, Max [digital]	0.0, 229.7, 60815.0
Flat Top 14,0%	
Beam Uniformity	0.600
Plateau Uniformity	0.005
Flatness Factor	0.416
Edge Steepness	0.960

Figure D.2.: Spot formation of the LUPI beam over the S1G2 grating at the focal point of the M2 mirror. Screenshot taken from the Beamview analyser software version 4.2.2. The spot size (effective diameter 50%) is 29 μm.

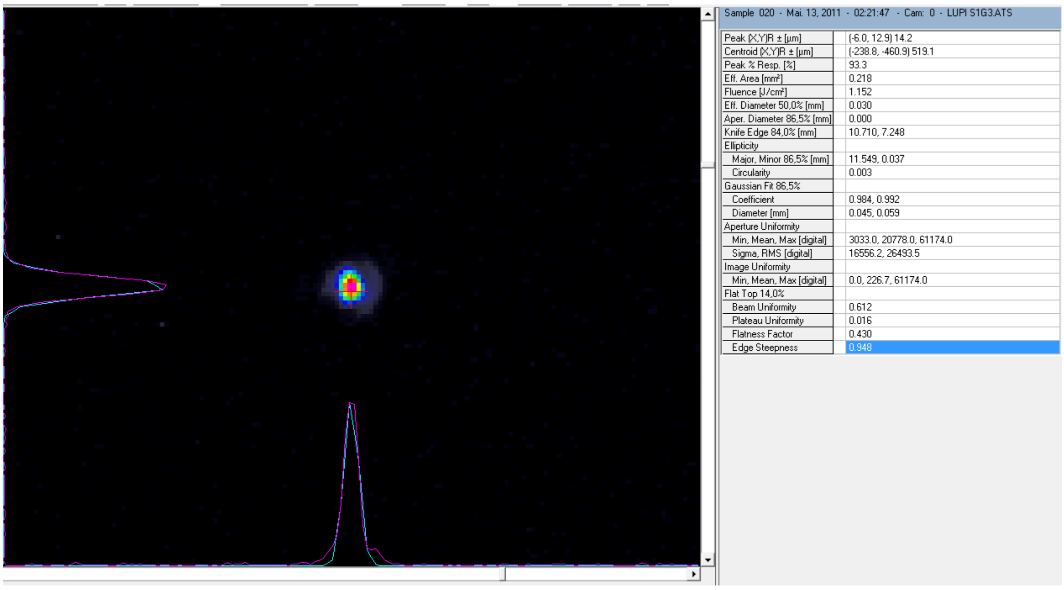

Sample 020 - Mai. 13, 2011 - 02:21:47 - Cam: 0 - LUPI S1G3.ATS

Peak (X,Y)R ± [µm]	(-6.0, 12.9) 14.2
Centroid (X,Y)R ± [µm]	(-238.8, -460.9) 519.1
Peak % Resp. [%]	93.3
Eff. Area [mm²]	0.218
Fluence [J/cm²]	1.152
Eff. Diameter 50,0% [mm]	0.030
Aper. Diameter 86,5% [mm]	0.000
Knife Edge 84,0% [mm]	10.710, 7.248
Ellipticity	
Major, Minor 86,5% [mm]	11.549, 0.037
Circularity	0.003
Gaussian Fit 86,5%	
Coefficient	0.984, 0.992
Diameter [mm]	0.045, 0.059
Aperture Uniformity	
Min, Mean, Max [digital]	3033.0, 20778.0, 61174.0
Sigma, RMS [digital]	16556.2, 26493.5
Image Uniformity	
Min, Mean, Max [digital]	0.0, 226.7, 61174.0
Flat Top 14,0%	
Beam Uniformity	0.612
Plateau Uniformity	0.016
Flatness Factor	0.430
Edge Steepness	0.948

Figure D.3.: Spot formation of the LUPI beam over the S1G3 grating at the focal point of the M2 mirror. Screenshot taken from the Beamview analyser software version 4.2.2. The spot size (effective diameter 50%) is 30 μm.

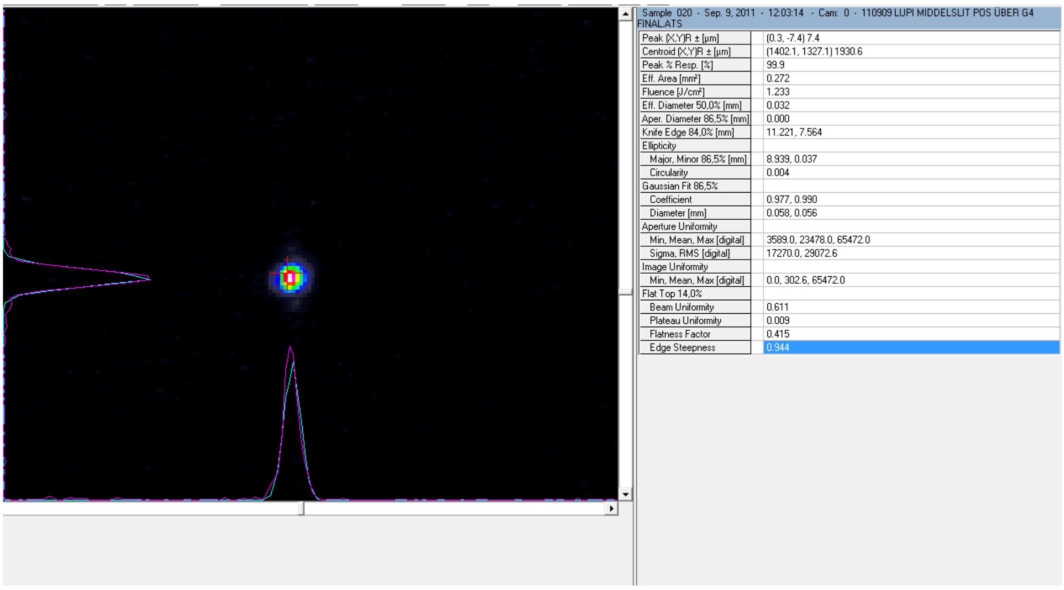

Sample 020 - Sep. 9, 2011 - 12:03:14 - Cam: 0 - 110909 LUPI MIDDELSLIT POS ÜBER G4 FINAL.ATS

Peak (X,Y)R ± [µm]	(0.3, -7.4) 7.4
Centroid (X,Y)R ± [µm]	(1402.1, 1327.1) 1930.6
Peak % Resp. [%]	99.9
Eff. Area [mm²]	0.272
Fluence [J/cm²]	1.233
Eff. Diameter 50,0% [mm]	0.032
Aper. Diameter 86,5% [mm]	0.000
Knife Edge 84,0% [mm]	11.221, 7.564
Ellipticity	
Major, Minor 86,5% [mm]	8.939, 0.037
Circularity	0.004
Gaussian Fit 86,5%	
Coefficient	0.977, 0.990
Diameter [mm]	0.058, 0.056
Aperture Uniformity	
Min, Mean, Max [digital]	3589.0, 23478.0, 65472.0
Sigma, RMS [digital]	17270.0, 29072.6
Image Uniformity	
Min, Mean, Max [digital]	0.0, 302.6, 65472.0
Flat Top 14,0%	
Beam Uniformity	0.611
Plateau Uniformity	0.009
Flatness Factor	0.415
Edge Steepness	0.944

Figure D.4.: Spot formation of the LUPI beam over the S2G4 grating at the focal point of the M3 mirror. Screenshot taken from the Beamview analyser software version 4.2.2. The spot size (effective diameter 50%) is 32 μm.

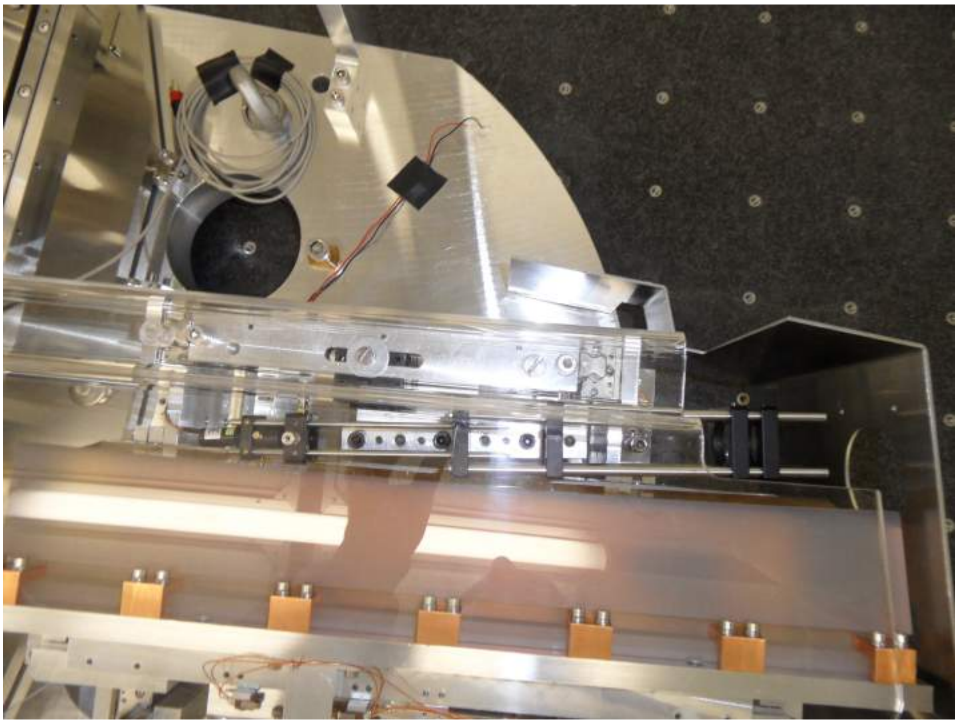

Figure D.5.: Picture of the focus marking lasers at the M1 mirror.

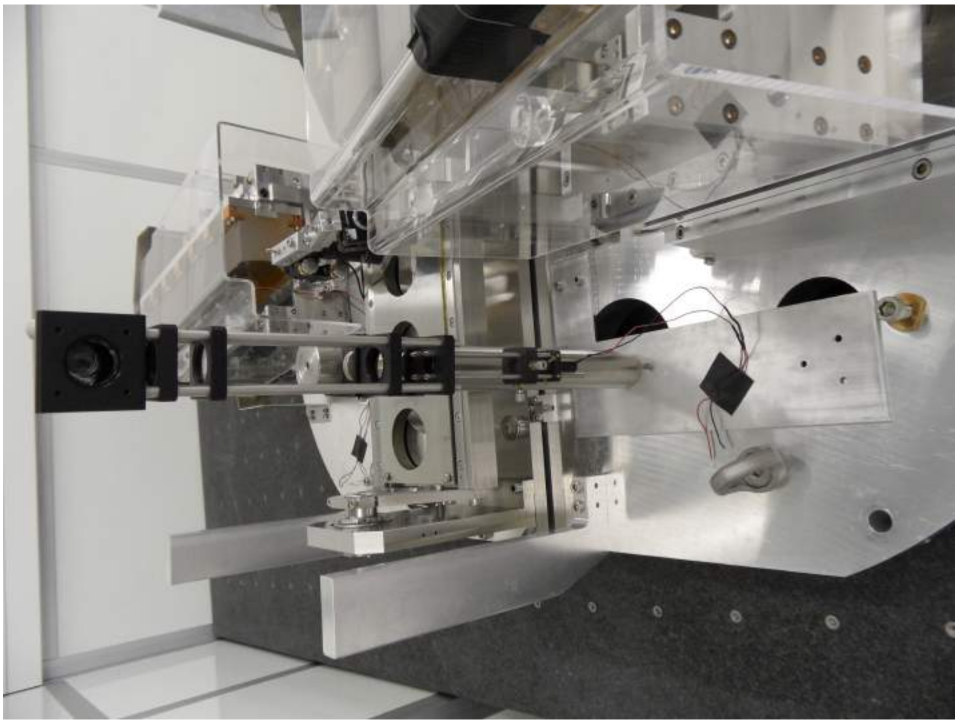

Figure D.6.: Picture of the focus marking lasers at the M2 mirror.

Figure D.7.: Picture of the marking lasers at the first monochromator stage.

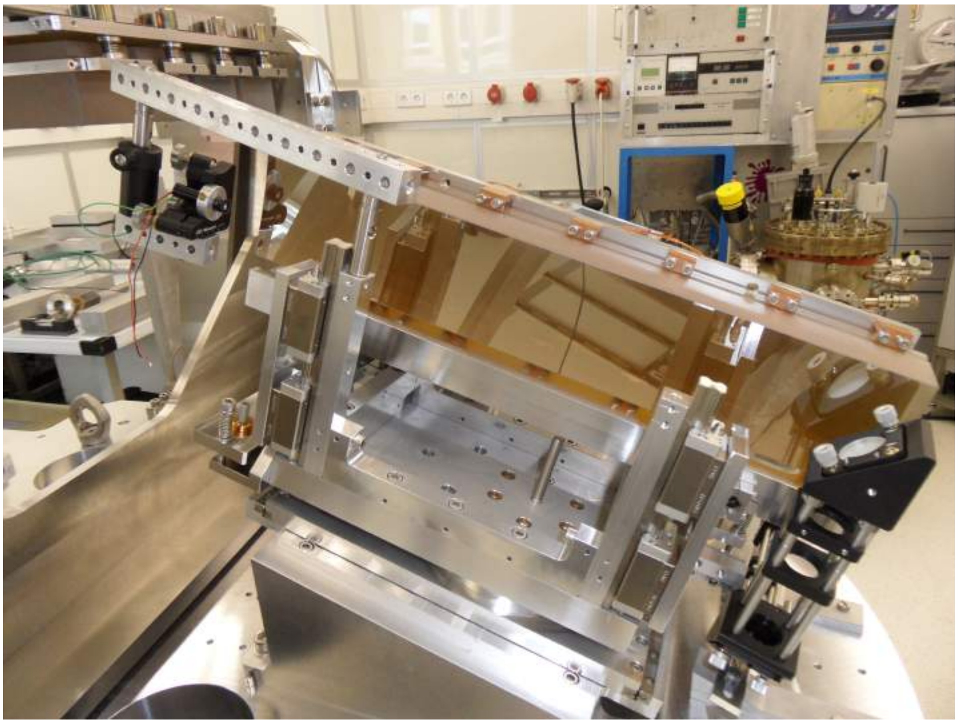

Figure D.8.: Picture of the marking lasers at the M3 mirror.